Characterizing the Impacts of Seismic Exploration Lines on the Hydrology and Vadose Zone for a Watershed in West-Central Alberta

by

Daniels Kononovs

A thesis submitted in partial fulfilment of the requirements for the degree of

Master of Science

Department of Earth and Atmospheric Sciences
University of Alberta

Abstract

Seismic lines are long linear cut lines through forests created for hydrocarbon exploration and comprise over 50 % of all linear disturbances in the Canadian Boreal Forest. They are known to impact local eco-hydrological conditions and show minimal regeneration back to pre-disturbance conditions. This thesis aims at assessing the effects of seismic exploration lines on the eco-hydrology and vadose zone of a 700 km^2 forested watershed located near Fox Creek in west-central Alberta. This region has been one of the most active areas for hydrocarbon production in Canada for the past 50 years, having a mean density of 3.3 km/km^2 of seismic lines. Here, the impacts of seismic exploration lines on soil-water content (SWC), the hydrological cycle using a 1-D model known as the Simultaneous Heat and Water (SHAW) model, and the physio-chemical properties of the vadose zone are examined using paired sites in disturbed and undisturbed areas.

SWC measurements indicated that seismic lines do not always have a higher moisture content. During the fall season, SWC measured at 15 cm depth were significantly higher on the seismic line due to the faster dormancy and reduced water usage of grasses and understory species that are dominant on seismic lines, in contrast to the trees and shrubs that are dominant in the adjacent undisturbed area. In the spring, SWC was significantly higher on the adjacent undisturbed area, due to delayed snowmelt on the seismic line. SWC measured during the summer and winter seasons was more variable among study sites and shallow soil layers (15 cm and 30 cm), which experience more seasonal SWC variations than deeper (60 cm) soil layers.

Using the SHAW model, an annual water budget was estimated for a 60 cm soil profile. The simulations revealed that undisturbed areas have a higher annual evapotranspiration (ET), by up to 117 mm/year, as compared to undisturbed areas. Consequently, the higher ET rates on

undisturbed areas lead to a larger depletion (up to 126.0 mm) of soil water storage. Simulated percolation at the bottom of the profile ranged from 0 to 47.8 mm/year, and was preferentially observed in the undisturbed areas, whereas seismic lines contributed to enhanced runoff.

Soil-water sampled using suction lysimeters was mainly of the $CaHCO_3$ type which is like the shallow (within 30 – 40 m) groundwater in the region. Measured $\delta^{18}O$ and $\delta^{2}H$ isotopic signatures of soil-water samples (n=154) indicate water of meteoric origin that has undergone minimal evaporation as they align with the local meteoric water line (LMWL). Soil bulk density (BD) values were all < 1.7 g/cm^3, thus within the range of typical mineral soils (1.0 to 1.8 g/cm^3). BD values for the upper 15 cm were higher by 8 to 65 % on the seismic lines compared to the undisturbed areas, showing that the soils were not significantly compacted by machinery. The soils were acidic with a mean pH of 4.9 (n = 30) and soil samples from seismic lines had a lower cation-exchange capacity (CEC) and higher concentrations of base ions (e.g., Ca^{2+}, Mg^{2+}) in the soil solution compared to undisturbed areas. The reduced CEC on seismic lines indicates a lower buffering capacity of the soil, increasing its vulnerability to acidification and potential contamination by metals compared to undisturbed areas.

Acknowledgements

The completion of this thesis was made possible through the invaluable assistance of numerous individuals and groups. Firstly, I'd like to express my gratitude to my supervisors Daniel Alessi, Dani Degenhardt, and Christine Rivard, who provided me with the opportunity to conduct this research and showed confidence in my research abilities to complete this thesis. Without their unwavering support and feedback, this thesis would not have been achievable. Additionally, I am very grateful to the Geological Survey of Canada of Natural Resources Canada and the Daniel Alessi Research Group for providing the financial resources that made this project possible.

I would also like to extent my appreciation to Kaitlyn Trepanier, Katherine Snihur, Daniela Gutierrez Rueda, Baptiste Coutret, Cody Lazowski, Kelly Rozanitis, Caren Jones, and all other individuals who contributed to the field and laboratory work conducted for this thesis. I am also indebted to the town and residents of Fox Creek for their warm hospitality and helpfulness during my field visits.

Last but not least, I am grateful for my family, friends, and my dog Luna who supported me throughout this project. Their continuous love, support, and humour cannot go unmentioned.

Table of Contents

List of Tables

List of Figures

List of Appendices

Chapter 1 Introduction

1.1 Background

The term "critical zone" describes the heterogeneous near-surface earth environment extending from the top of the vegetation canopy to the underlying groundwater (Brantley *et al.,* 2007; Richardson, 2017). This region hosts complex physical, chemical, and biological processes involving the simultaneous interactions of the atmosphere, hydro-geosphere, pedosphere, and living biota, all of which regulate crucial resources for life (Richardson, 2017). The continual impacts of anthropogenic activities and climate change on the natural environment have led to an increasing importance on studying the critical zone to ensure its sustainability and to better understand its response to human activities. However, analysis of the various processes operating within the critical zone is difficult as it requires an inter-disciplinary approach that considers complex spatio-temporal variations (Brantley *et al.,* 2007).

Canada's vast boreal ecosystem (approximately 552 million ha.) has been subjected to anthropogenic activities leading to an increasingly fragmented landscape (Pasher *et al.,* 2013), making the critical zone in this region particularly vulnerable. Within the boreal ecosystem is the Boreal Plains (BP) Ecozone (Figure 1.1), Canada's fourth largest ecozone (Environment Canada, 2013) spanning across the provinces of Manitoba, Saskatchewan, and Alberta with minor excursions in British Columbia and Northwest Territories. The dominant land uses in the BPE comprise 59% forestry and 19% agriculture, 11% conservation, and lesser amounts for industrial uses (NRCan, 2020). The BP, particularly its western extent in Alberta, has undergone rapid and significant industrial development, presenting challenges in preserving its ecological features (Pasher *et al.,* 2013).

A major anthropogenic disturbance in western BP is the presence of linear seismic exploration lines produced by the hydrocarbon extraction industry, which comprise nearly half of all linear disturbances in the Canadian Boreal Forest (Pasher *et al*., 2013). Timoney

and Lee (2001) estimated a total length of 1.5 to 1.8 million km of lines in Alberta alone. Early seismic lines in Western Canada, referred to as "legacy lines", are linear disturbances, roughly 5 – 10 m wide, and intersect many other linear features over the landscape (Davidson *et al*., 2020). Legacy seismic lines were constructed until the early 1990s using bulldozers to clear vegetation and flatten topography to produce a landscape suitable for the seismic surveys (Lee and Boutin, 2006; Braverman and Quinton, 2016). The construction of these legacy lines often resulted in significant soil and vegetation disturbance (Dabros et al. 2018) and in certain cases it involved scraping the topsoil and mixing it with the underlying mineral soil layers (MacFarlane, 2013). Following the 1990s, legacy lines were replaced by low-impact seismic (LIS) lines in Alberta, British Columbia, Northwest Territories, and Yukon to reduce their ecological footprint (Dabros *et al.* 2018). LIS are narrower (1.5–5 m wide), have meandering paths through forests, and cause less soil disturbance as they are constructed using low ground pressure bull dozers (MacFarlane 2013). However, LIS are typically placed in a high-density grid, with spacing often as close as tens of meters apart (Lee and Boutin 2006; Dabros *et al.* 2018). Overall, improved management practices and the implementation of LIS, has greatly reduced the damage to soil and ground layer vegetation (Dabros *et al.* 2018). Nevertheless, many seismic lines, remain visible on the landscape, even decades after their creation, especially in wetland ecosystems (van Rensen *et al.* 2015).

The Fox Creek region of west-central Alberta (Figure 1.1) was selected for this MSc thesis study as it has undergone extensive petroleum exploration and production dating back to the late 1950s (Fox Creek Historical Association, 1992). Petroleum production was further spurred in the region due to advances in horizontal drilling techniques and hydraulic fracturing which allowed unconventional reservoirs to be tapped (Rivard *et al*., 2014; Alessi *et al*., 2017). Thus, studying the impacts from petroleum activities in this area, particularly from seismic exploration lines on the critical zone appeared important and was selected as the focus of this MSc research. The objective of this project was to study and compare the

hydrological cycle and vadose zone over the course of a year in undisturbed forests and areas disturbed by seismic exploration lines using *in situ* measurements and sampling, laboratory analyses and numerical modeling. This study is part of a larger Geological Survey of Canada (GSC) multi-institutional project investigating the cumulative environmental effects of resource extraction in a 700 km^2 watershed located in the Fox Creek region.

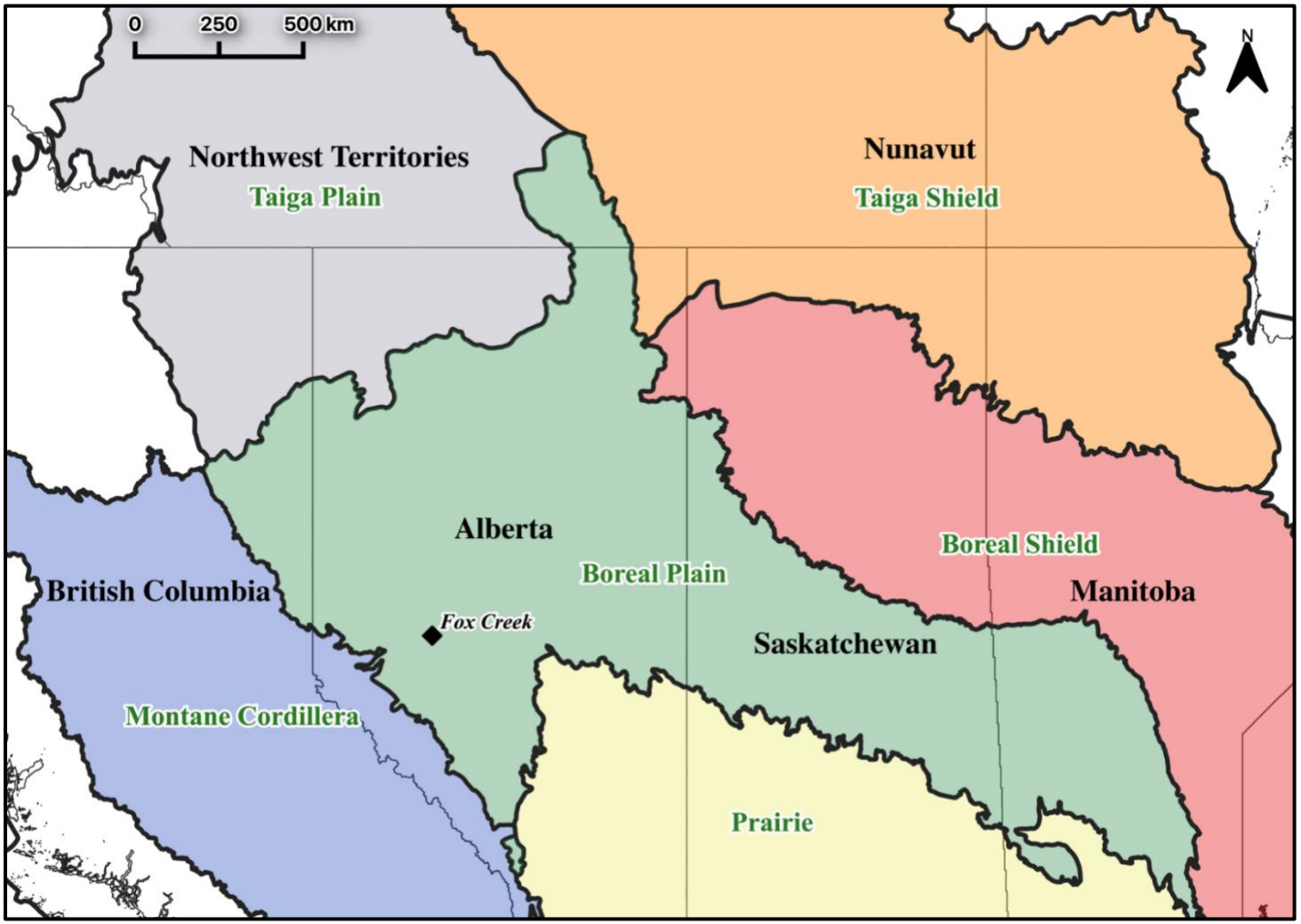

Figure 1.1: Map of Western Canada showing the major ecozones and the watershed.

1.2 General Context of the Fox Creek Region

1.2.1 Physiography and General Context

The study area is a 700 km^2 watershed located near the town of Fox Creek, west-central Alberta (54.4009 ° N, 116.8045 ° W) (Figure 1.2). Land surface elevation varies by approximately 425 m, from 1180 m in the southwestern margin of the study area to 755 m in the northern part. Physiographical features in this region were largely shaped by the underlying bedrock (Atkinson and Hartman, 2017) yielding high-relief benchland terrain as the dominant land expression in this region which is most prominent in the southwestern part of the study area near the Rocky Mountain Foothills (Atkinson and Hartman, 2017). Drainage in this ecoregion follows the slope of a northeastward trend via the Athabasca, Saskatchewan, and Peace River basins (Environment Canada, 2013).

The land surface in the watershed is dominantly forested and contains significant infrastructure from hydrocarbon production, including gravel roads, gas plants, well pads, pipeline corridors, and fluid storage facilities. The intensive petroleum activities in this region have led to over 775 oil and gas wells being completed within the Duvernay Formation (Guarin-Martinez, 2022) and a high density of seismic exploration lines (3.3 km/km^2) (Figure 1.2). The western part of our study area includes the Little Smoky range (Figure 1.2), which is considered among the most disturbed woodland caribou ranges in Canada (Russell *et al*., 2016; Alberta Wilderness Association, n.a.), notably due to the high density of seismic lines in Alberta (Government of Alberta, 2017).

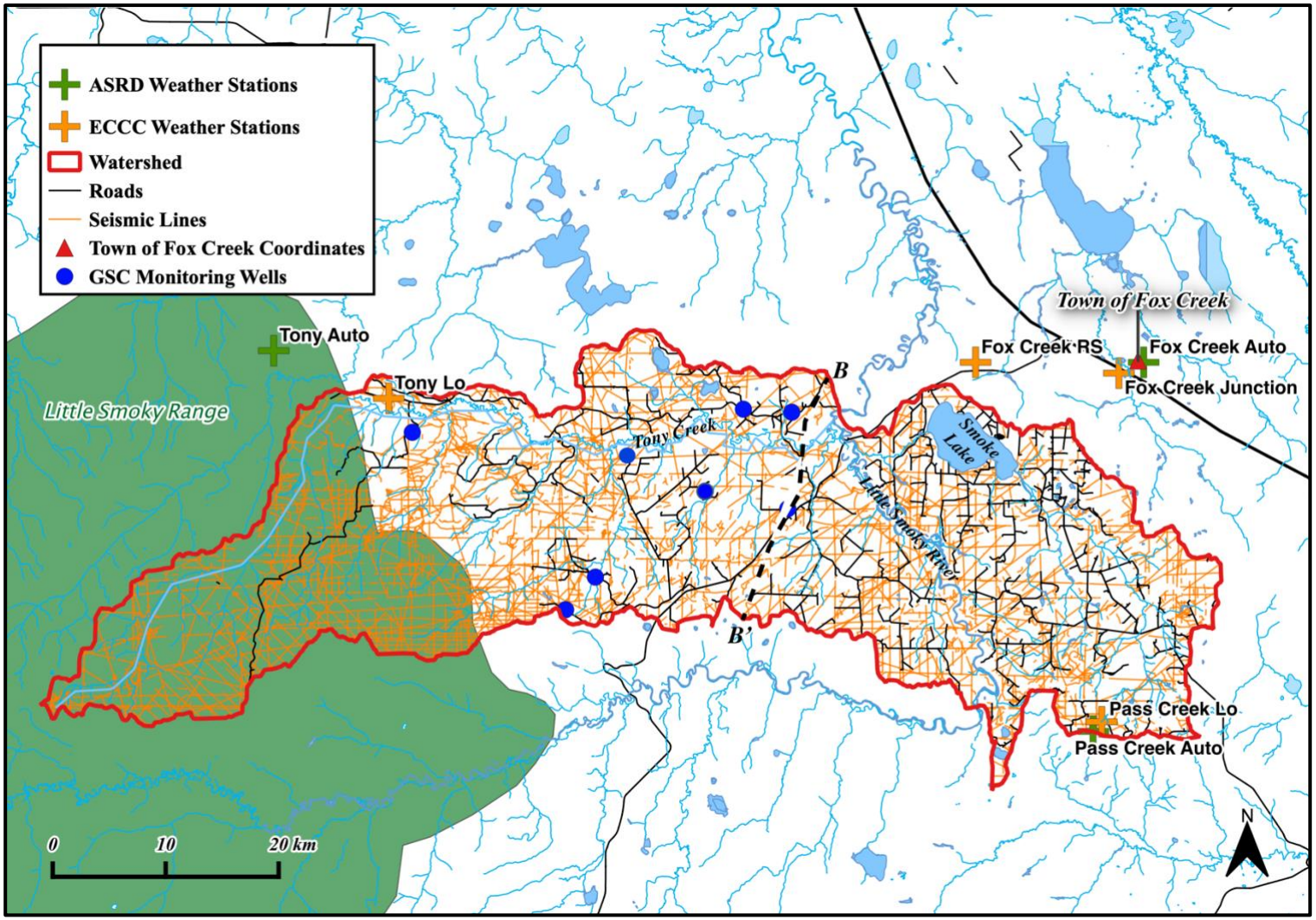

Figure 1.2: Map of the watershed study area near the town of Fox Creek. Cross section B-B' is used in Figure 1.3 after Corlett *et al.* (2019) and Guarin-Martinez (2022).

1.2.2 Geological Background

West-central Alberta is underlain by Upper Cretaceous – Paleogene bedrock emplaced by fluvial systems originating from the Laramide Orogeny (Atkinson and Hartman, 2017). In sedimentary succession, bedrock strata in the area of study near Fox Creek include non-marine deposits from the Wapiti, Battle, Scollard, and Paskapoo formations, which subcrop in a northernly direction (Figure 1.3) (Atkinson and Hartman, 2017; Smerdon *et al.,* 2019). These formations contain an assemblage of mudstones, siltstones, and sandstones with the Battle Formation being an exception as it is primarily mudstone dominated and contains altered volcanic ash (Hathway and Plint, 2011).

The Cretaceous Wapiti Formation consists mainly of alluvial deposits with minor lacustrine sediments and interbedded coal seams (Dawson *et al*., 1994). The Late Cretaceous Battle Formation contains lacustrine/marsh deposits ranging from 18-m thick to completely eroded away (Hathway and Plint, 2011). The Cretaceous to Paleogene Scollard Formation comprises fluvial and deltaic deposited sediments with major interbedded coal seams (Gibson, 1977). Lastly, the Paleogene Paskapoo Formation consists of fluvial deposits that become sandier in texture towards its southern extent, where it can reach up to 800 m in thickness (Grasby *et al*., 2008). The bedrock strata are overlain by thin (generally < 20 m in the study area) unconsolidated Paleogene-Quaternary surficial sediments which are mainly comprised of glacial and fluvial deposits that are more permeable near the southern extent of the Paskapoo Formation (Atkinson and Hartman 2017; Hughes *et al*. 2017). The permeability of the surficial sediments in the study region is likely lower than those near the southern extent of the Paskapoo Formation since the composition of these sediments is largely derived from the underlying formation. Guarin-Martinez (2022), in a hydrogeological study of the study area carried out earlier as part of the GSC project, had estimated that vertical aquifer recharge was indeed low, ranging from of 0 to 70 mm/year, in agreement with the estimate of Smerdon *et al.* (2019).

The Paskapoo Formation comprises a large regional aquifer that is heavily exploited with over 150,000 users in Alberta (Lyster and Andriashek, 2012). The Paskapoo Formation has been divided into three hydrostratigraphic units, which in ascending order are the Haynes Aquifer, Lacombe aquitard, and the Sunchild Aquifer based on sandstone occurrence (Lyster and Andriashek, 2012). These hydrostratigraphic units have a large range in hydraulic conductivity values (10^{-10} to 10^{-3} m/s), which reflect the very heterogeneous nature of the aquifer (Grasby *et al.,* 2008; Atkinson and Hartman, 2017). Additionally, locally occurring high hydraulic conductivity sand lenses connect the Haynes and Sunchild aquifers (Lyster and Andriashek, 2012).

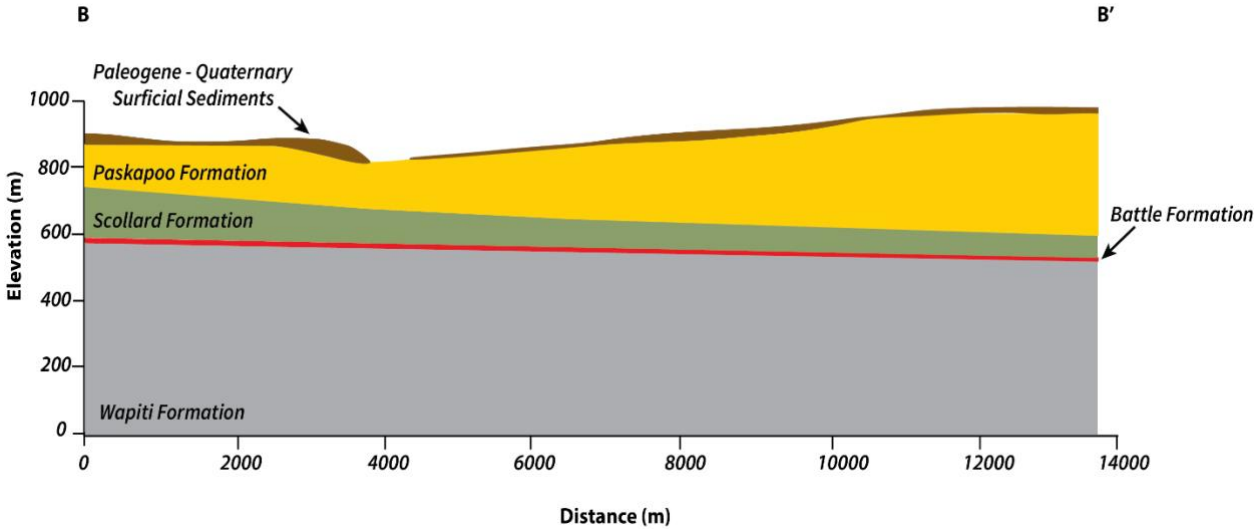

Figure 1.3: Cross-section B to B' showing the geology within the watershed modified after Corlett *et al*. (2019) and Guarin-Martinez (2022).

1.2.3 Climate and Hydrology

Historical climate data for this project were collected from six weather stations with time-series data that vary in temporal coverage and proximity to the Fox Creek study area (Figure 1.2). Of these, three are still active and are maintained by Alberta Sustainable Resource Development (ASRD); the other three inactive weather stations were maintained by Environment Canada Climate Change (ECCC) and terminated measurements in 2011-2012. Table 1.1 summarizes the climate variables recorded by the ECCC and ASRD weather stations.

Table 1.1: Climate variables available from ASRD and ECCC weather stations near or inside the study area (ECCC, 2011; ACIS, 2022).

Weather Stations	Temperature	Relative Humidity	Wind Speed	Reference Evapotranspiration (ET)	Liquid (Rain) Precipitation	Solid (snow) Precipitation
ECCC	✓	x	x	x	✓	✓
ASRD	✓	✓	✓	✓	✓	x

The ASRD weather stations have a complete data record for humidity and temperature but not precipitation, which is measured with a tipping bucket-type rain gauge that accurately measures only liquid precipitation (rain), primarily during the months of June to August, and is not recommended for snow measurements. Although no longer active, the ECCC weather stations have longer climate records than the ASRD stations. Except for the Fox Creek Junction weather station, the other ECCC stations (Pass Creek Lo and Tony Lo) have a significant amount of missing daily temperature and precipitation data (Table 1.2). Data from the newer ASRD weather stations represent a near-continuous coverage, but over a shorter time-period.

Due to the inconsistency in data availability across the six weather stations near the study area, the Ground Water Hydrograph Analysis Toolbox (GWHAT, Gosselin, 2022) was used to obtain a comprehensive dataset using the most complete data series, and data from the other five weather stations to fill in the gaps. GWHAT uses a Python Gap Filling Weather Data algorithm (PyGWD), which relies on multiple linear regression (MLR) based on proximity and similarities to nearby weather stations to fill-in and estimate missing weather data (Gosselin, 2016). The gap-filled climate data produced by GWHAT for all weather stations is summarized in Table 1.3 along with the long-term climate normal histograms in Figure 1.4 for the most complete original records (Fox Creek Junction and Fox Creek Auto, both located to the west of the study area). Of note, statistics for Pass Creek Lo and Tony Lo

stations are presented in Table 1.3, although they each have a high percentage of missing data, particularly for the winter months.

Table 1.2: Parameters for the six available weather stations near or inside the study area. ASRD data obtained via ACIS (2022). ECCC data obtained via ECCC (2011).

Station	Distance to Watershed (km)	Data Availability (Number of years)	Elevation (m)	Source	% Missing Data
Town of Fox Creek	5	2011-Present (12)	850	ASRD	0
Fox Creek Junction	4	1991-2012 (21)	829	ECCC	7
Pass Creek Auto	within	2016-Present (7)	1081	ASRD	0
Pass Creek Lo	within	1954-2011 (57)	1135	ECCC	65
Tony Auto	4	2016-Present (7)	1007	ASRD	0
Tony Lo	within	1957-2011 (54)	1036	ECCC	64

Table 1.3: Calculated weather mean values from GWHAT for each weather station time period specified in Table 1.

Station	Daily T-min (°C)	Daily T-avg (°C)	Daily T-max (°C)	Rain (mm/year)	Snow* (mm/year)	Total Precipitation (mm/year)	ETP (mm/year)	PET:P
Fox Creek Auto	-2.3	3.4	9.2	408.6	NA	413.2	549	1.3
Fox Creek Junction	-4	2.6	9.3	412.2	107.6	519.8	535	1.3
Pass Creek Auto	-2.3	2.5	8	496.5	NA	519.8	513.8	1
Pass Creek Lo	*2.4*	*6.6*	*10.7*	*429*	*NA*	*434.6*	*543.5*	*1.3*
Tony Auto	-2.3	2.9	8.5	488.8	NA	513.1	523.4	1.1
Tony Lo	*2.7*	*8*	*13.2*	*392.7*	*NA*	*398.3*	*589.3*	*1.5*

Notes: ETP: potential evapotranspiration values are calculated via the Thornthwaite method in GWHAT (Thornthwaite, 1948). Snow* (mm/year) denotes these measurements are unreliable yearly estimates. Data for Pass Creek Lo and Tony Lo are formatted differently because of the amount of missing data.

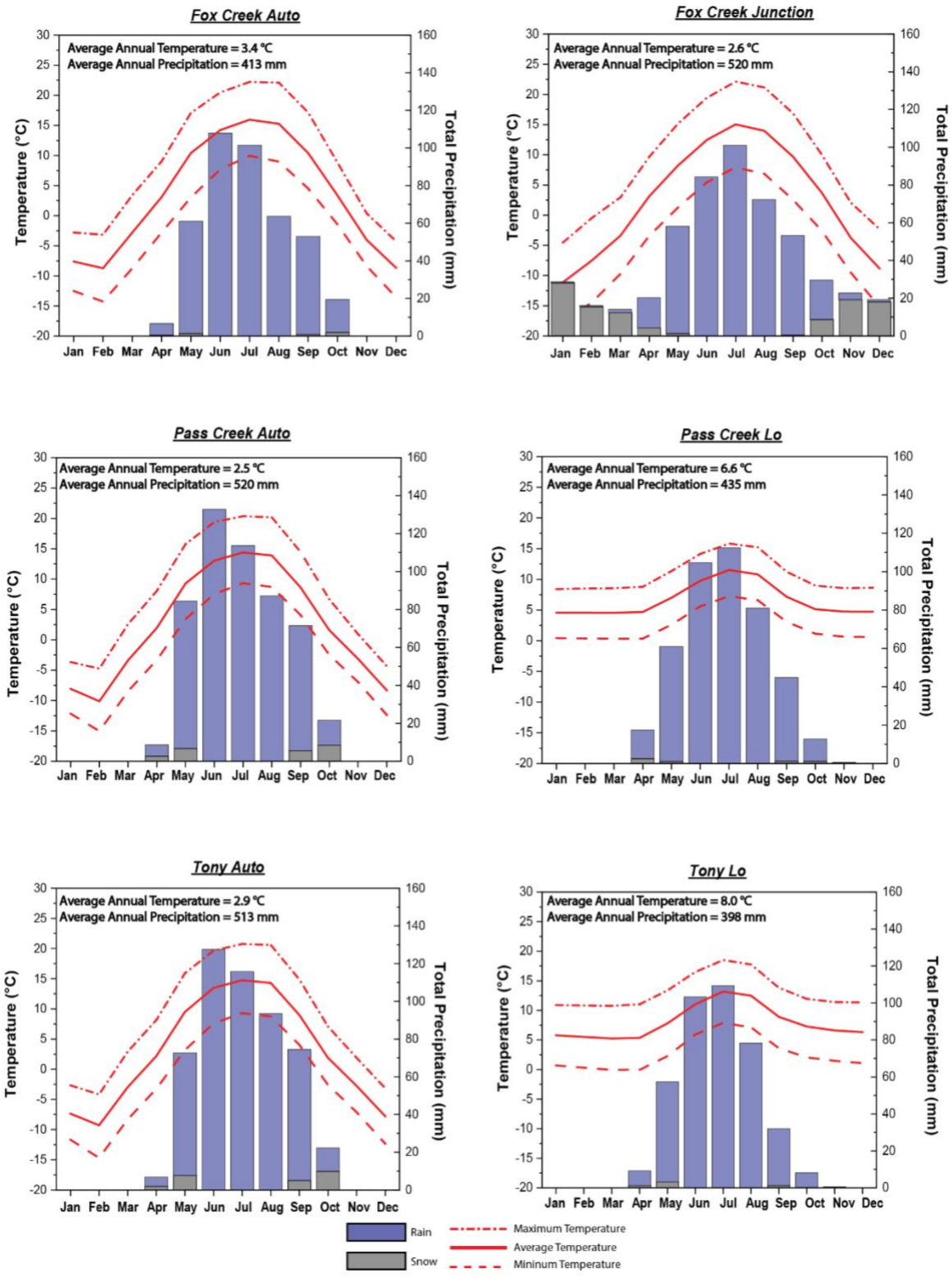

Figure 1.4: Climate normal histograms for select weather stations near the area of study and their data availability. Data normalized via GWHAT software (Gosselin, 2022).

The Fox Creek Junction weather station has the most complete weather record for the region (and in particular for the winter period) and was therefore used to classify the climate of the region based on the Koppen-Geiger Climate Classification system. The Fox Creek region can be characterized as Dfc, a cold climate, without a dry season, and cold summers with year-round precipitation (Peel *et al*., 2007). Using the dryness index (PET:P) (Table 1.3), it can be surmised that the climate within the region is characterized by an overall long-term moisture deficit ($P \leq ET$) as confirmed by Smerdon *et al*., (2019).

Other studies have found similar mean weather values for the area of study. Devito *et al.* (2012) used more than 30 years of data to obtain average values of potential evapotranspiration (PET) and precipitation of 520 mm and 480 mm, respectively, for the entire Boreal Plains. Smerdon *et al.* (2019) used long-term (1989-2010) climate-normal values from ClimateNA gridded data (Wang *et al*., 2016) to estimate an average precipitation of 595 mm/year and reference evaporation of 525 mm/year for the area near the Town of Fox Creek, yielding a slight water surplus (70 mm/year), which was retained as a value for potential vertical recharge.

However, temporal and spatial cycling of precipitation in this region is significant. Temporally, this region is characterized by cycles of 3–5 years per decade where $P < PET$, alternating with 3–5 year cycles where $PET \cong P$, and then much longer 20-30-year cycles where $P > PET$ for 1-2 years (Devito *et al*., 2012). Spatially, precipitation rates vary considerably in West-central Alberta, and therefore in the Fox Creek area, since the originating moisture from the Pacific Ocean encounters the Rocky Mountains experiencing orographic lift causing large spatial variability in precipitation events (Smerdon *et al*., 2019). Overall, Devito *et al.* (2012) characterized the WBP as a region with a long-term moisture deficit where precipitation is generally less than or close to ET.

1.2.4 Vegetation Cover

The watershed is located within the Western Alberta Upland (WAU) ecoregion where forests are mixed with trembling aspen, white spruce, lodgepole pine, paper birch, balsam poplar, and balsam fir (Ecological Stratification Working Group, 1996). Generally in this ecoregion, dry ecosites are inhabited by aspen and lodgepole pine, whereas wet ecosites are dominated by tamarack and black spruce (Ecological Stratification Working Group, 1996). Based on a digital landcover mapping project of Alberta by the Alberta Biodiversity Monitoring Institute (ABMI), the dominant vegetation communities within the watershed itself include coniferous forests, broadleaf forests, shrubland, mixed forests, and grassland respectively (ABMI, 2010) (Figure 1.5).

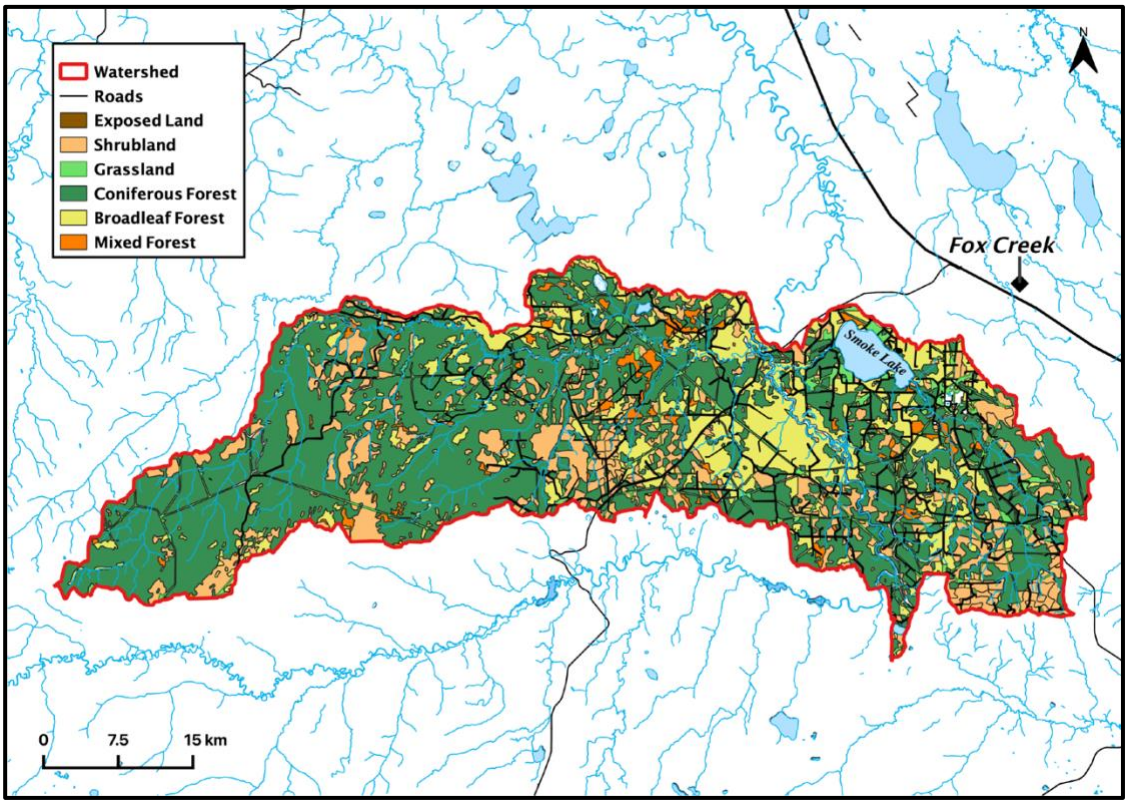

Figure 1.5: Map of the dominant landcover types within the watershed study area. Landcover polygons obtained via ABMI (2010).

1.2.5 Soil Cover

Soils within the WAU ecoregion are dominantly developed Luvisols, Gleysols, and Organic soils (Ecological Stratification Working Group, 1996). Based on a large and detailed

soil-survey report in the region of study (Knapik and Lindsay, 1983), the major soil types within the watershed are Orthic Grey Luvisols and Mesisols respectively with appreciable amounts of Gleysols, Fibrosols, and Humisols. Soil textures in the watershed range from sandy to silt loam comprised of regional till (Knapik and Lindsay, 1983) along with slightly more permeable soils generally occurring in the western part of the study area (Guarin-Martinez, 2022).

1.3 Thesis Objectives

The overall objective of this thesis was to investigate the impacts of the many lineaments created by industry, and more specifically seismic exploration lines, on soils, vegetation and especially the various components of the water budget over the course of a year in the study area. To achieve this, three specific research goals were defined: (i) to monitor soil-moisture at different depths and locations, (ii) to estimate the water budget using a 1-D physically based model known as the Simultaneous Heat and Water (SHAW) model, and (iii) to collect soil, water and snow samples, on a monthly basis for precipitation and soil water from different depths in the vadose zone, to better understand the evolution of the physio-chemical properties during infiltration along vertical soil profiles.

For this project, monitoring sites within the watershed were established and visited on a monthly basis for approximately 1.5 years. Data collection involved baseline soil sampling and vegetation surveys, as well as installing equipment to monitor soil moisture and general weather parameters on an hourly basis and to sample snow, rainwater, and soil water mostly on a monthly or bi-monthly basis. Gathering information on vegetation, physical and chemical properties of soil, along with its organic and inorganic chemical constituents, was intended to enable us to temporally quantify the water budget components and better understand their interactions in this area, as well as identify potential impacts of hydrocarbon extraction related activities.

Chapter 2 Literature Review

2.1 Western Boreal Plains

The eco-hydrological functioning of the Western Boreal Plains (WBP) landscape, where Fox Creek (Alberta) is located, is controlled by the interaction of climate and geology, which controls the degree of groundwater infiltration and recharge, the types of vegetation communities present, and wetland sustainability (Ferone and Devito 2004; Devito *et al*. 2005, 2012; Smerdon *et al*. 2005; Petrone *et al*. 2007).

The WBP Landscape consists of alternating lowlands (wetlands) and uplands (forested lands) that were formed on thick heterogeneous glacial deposits in a climate characterized by a net moisture deficit (Precipitation (P) ≤ Evapotranspiration (ET)), where P and ET are the dominant hydrologic fluxes (Devito *et al.* 2012). The close long-term relation between P:ET for WBP landscapes results in most of the water being used up and recycled to the atmosphere by vegetation and/or stored in the subsurface soil and sediments (Devito *et al.* 2012). Any moisture surplus made available during spring melt or during a year with higher than normal precipitation can move into soil storage, percolate further into groundwater storage and/or contribute to runoff (Devito *et al.*, 2012). From a hydrologic perspective, lowland areas with minimal standing water in the WBP act as water sources that exist in a regime of moisture surplus, whereas upland areas act as water sinks having a moisture deficit (Devito *et al.*, 2012).

ET is a process that combines the transfer of surface water to the atmosphere by evaporation from the soil-surface/vegetation and transpiration via leaf stomata (Devito *et al*. 2012). Generally, ET rates depend on (i) climate variables (e.g., temperature, solar radiation, humidity, vapor pressure deficit, wind), and (ii) forest characteristics (e.g., tree types and ages, canopy density, and interception capacity) (Wei *et al.* 2022). Although ET is a dominant hydrologic flux in the WBP, it is difficult to estimate for the entire WBP. This is because ET rates vary among wetland and upland landscapes, not only because climatic conditions can

change, but also because of differing vegetation communities (Nijssen and Lettenmaier 2002), percent cover of vegetation, and soil-types (Grelle *et al*. 1997; Cuenca *et al*. 1997). For instance, upland regions dominated by aspen have a large water demand and can form extensive lateral root networks that can cycle water from adjacent wetlands (i.e., water that would be otherwise detached from water in upland regions), increasing ET (Nosetto *et al*. 2005; Devito *et al*. 2012). In wetland regions dominated by bryophytes (i.e. feathermoss), ET is mainly controlled by large hydrological events and/or dew processes, limiting ET over time (Busby *et al*. 1978; Vitt and Chee 1990). Therefore, to understand the hydrologic budget for landscapes within the WBP, an accurate conceptualization of ET, groundwater recharge, and soil-water storage is required (Smerdon *et al*. 2009; Devito *et al*. 2012).

Additionally, snow water equivalent (SWE) is a key parameter in many hydrological models. It is calculated by multiplying snow-depth by snow-density. Remote sensing techniques can estimate snowpack properties at a larger spatial scale such as a watershed; however, these techniques often come with some degree of uncertainty and require validation using ground-truth data (Kinar and Pomeroy, 2015). Site-specific snow-density values are typically obtained via manual measurements with snow-cores or sensors installed on weather stations which also require manual measurements for calibration (Beaudoin-Galaise and Jutras, 2022). Estimating SWE from spring melt in boreal forests is particularly important, as it can account for up to 50% of annual runoff (Pomeroy *et al.,* 1998). However, SWE within forested regions may vary considerably in both space and time due to the complex snowpack energy balance imposed by the interactions of the vegetation canopy with climate (Sun *et al.,* 2022). For instance, by mid-winter the vegetation canopy in cold boreal forests can intercept up to 60% of cumulative snowfall, most of which will sublimate rather than fall onto the ground surface (Pomeroy and Gray, 1995).

2.2 Seismic Exploration Lines

Major anthropogenic disturbances in the Boreal Plains are caused by the construction of seismic exploration lines by the hydrocarbon industry. Seismic exploration lines comprise almost 50% of all linear disturbances in the Canadian Boreal Forest (Pasher *et al*., 2013), whereas another 12.6% corresponds to pipelines (Pasher *et al*., 2013). Timoney and Lee (2001) estimated a total length of 1.5 to 1.8 million km of lines in Alberta alone. Within the 700 km^2 watershed in this study (Figure 1.2), approximately 2200 km in total length of seismic lines exist (ABMI, 2019). Seismic lines are created during the early stages of petroleum exploration to conduct seismic surveys, which use geophones to unveil potential exploitable hydrocarbon traps (Dabros *et al*., 2018). Conventional seismic lines (i.e. legacy lines) in western Canada are roughly 5 – 8 m wide linear features intersecting many other lines over the landscape (Davidson *et al*., 2020) and were constructed up until the end of the 20^{th} century (Dabros *et al*., 2018). These conventional seismic lines were constructed using bulldozers that would clear vegetation and flatten topography to produce a landscape suitable for the seismic surveys (Lee and Boutin, 2006; Braverman and Quinton, 2016). A study on early conventional seismic lines constructed during the summer in the 1960's showed that the construction of seismic lines resulted in the removal of roots and the top layer of soil (Bliss and Wein, 1972), which takes several decades to regenerate. The great length of many seismic lines means they can intersect various ecosites types, as defined by soil moisture and nutrient conditions along with vegetation type (Revel *et al*., 1984; Beckingham and Archibald, 1996; van Rensen *et al*., 2015).

Since the 1960's, new techniques have emerged to minimize the adverse environmental impacts of seismic lines. These include limiting seismic line construction to winter months to avoid enhanced soil disturbance and the construction of narrower (< 5 m) seismic lines (i.e. low-impact seismic lines), which are meandering rather than linear features (Dabros *et al*., 2018). However, currently Alberta does not require the restoration of seismic

lines to their original state (Davidson *et al*., 2020). It has always been assumed that the altered landscape would naturally restore back to its pre-disturbed conditions over time, but the footprint may remain on the landscape for an extended period of time (Lee and Boutin, 2006; Dabros *et al*., 2018). Some current restoration and preventative measures include silviculture and site preparation techniques (Lee and Boutin, 2006).

Vegetative communities on seismic lines are typically comprised of light and disturbance tolerant species (Lee and Boutin, 2006; Finnegan *et al.,* 2018). Regeneration of vegetation to pre-disturbance conditions on seismic lines is influenced by a myriad of factors: ecosite, seismic line characteristics (width, length, aspect), disturbance history, landscape features, and anthropogenic activities (van Rensen *et al.,* 2015). A previous study demonstrated that partially recovered conventional seismic lines were dominated by an understory of grasses and herbs, whereas woody vegetation only recovers to approximately 8% of its original state after 35 years (Lee and Boutin, 2006). The moisture content of landscapes affected by seismic exploration lines has been attributed as one of the main factors influencing the degree of woody vegetation recovery (Lee and Boutin, 2006; van Rensen *et al*., 2015) with particular sensitivity in wet lowland ecosites. For example, a study in the Western Boreal Plains region of Alberta (Lee and Boutin, 2006) found that following a significant lag time (35-years), upland ecoregions are more likely to recover to > 50% woody vegetation compared to wet lowland black spruce forests, which show minimal to no recovery.

Because vegetation communities are different on a seismic line compared to adjacent undisturbed areas, this inevitably alters the hydrologic cycle (Dabros *et al*., 2018). The overall decreased abundance of vegetation on seismic lines results in reduced evapotranspiration rates relative to adjacent undisturbed areas and, hence, increased soil moisture content, and surface and subsurface runoff due to a higher surficial soil density as a result of machinery passing through (Vitt *et al*., 1975; Dabros *et al*., 2018). The higher soil moisture conditions on seismic

lines may further alter soil structure making the soil more susceptible to compaction; thus, potentially further negatively affecting vegetative recovery (Dabros *et al*., 2018). Furthermore, the soil may be compacted by frequent recreational reuse and/or animal migration on seismic lines (Revel *et al.,*1984; Lee and Boutin, 2006), which may result in impeded root growth and plant access to water and nutrients (Blouin *et al.,* 2005). Additionally, light availability on seismic lines is often limited (depending on the line width and orientation) due to shading from tall trees on the undisturbed areas and can further limit vegetation recovery (van Rensen *et al.,* 2015; Filicetti *et al.,* 2019). Snow melt on linear seismic lines is also delayed compared to adjacent natural areas due to a decreased albedo, in turn limiting plant phenology (Haag and Bliss, 1974; Bjorkman *et al*., 2015; Dabros *et al*., 2018). The longer residence time of snow on seismic lines results in an increase in albedo during the winter months, resulting in delayed thawing of the soil, the opposite being true during the summer months (Haag and Bliss, 1974; Dabros *et al*., 2018).

Canada's boreal ecosystems host substantial carbon stocks in its biomass and soil, acting as a net sink for atmospheric CO_2 (Kurz *et al.* 2013). However, the combined impacts of climate change and anthropogenic landscape disturbances may potentially transform certain boreal areas into net carbon sources in the near future (Kurz *et al.* 2013). Specifically, the cumulative effects from industrial development (which include linear disturbances such as seismic lines) are known to alter the carbon dynamics of boreal ecosystems in Canada (Pasher *et al.* 2013; Dabros *et al.* 2018). Two factors contributing to altered carbon cycling following seismic line construction are the removal of vegetation (Dabros *et al.* 2018) and enhanced microbial respiration on seismic lines in boreal peatlands where graminoids and shrubs are the dominant vegetation type (Strack *et al.* 2019). In Alberta, peatlands cover ~ 134,790 km^2 (Strack *et al*. 2019) and store ~ 48 Gt of soil carbon (Vitt *et al.* 2000). However, peatlands impacted by industrial activities may lead to enhanced CH_4 emissions due to altered vegetation communities, water table position, and soil temperature (Strack *et al.* 2019). For

instance, a study by (Strack *et al.* 2018) observed that the conversion of a 6 m wide seismic line into a winter road resulted in a tenfold increase in CH_4 emissions. The increase in CH_4 emissions was attributed to the shift to a graminoid dominated plant community and higher soil temperatures on the seismic line.

The creation of seismic lines may also result in unintended altered predatory and prey dynamics between wolves and caribou (Lee and Boutin, 2006; Dabros *et al*., 2018). The western part of our study area includes approximately 5% of the total area of the Little Smoky caribou range (Alberta Wilderness Association, 2017). Anthropogenic activities have disturbed 99% of the Little Smoky caribou range and the current estimate of the herd size is 110 caribou (Alberta Wilderness Association, 2017). The high density of seismic lines in Alberta have contributed to woodland caribou being designated as an at-risk species (Government of Alberta, 2017), as other ungulates and wolves use seismic lines as movement corridors thus changing the predatory-prey dynamics in regions with a high density of seismic lines, making caribou more vulnerable (Russell *et al*., 2016).

2.3 The Vadose Zone

2.3.1 Physical Properties

Understanding the physical properties of the vadose zone is crucial for interpreting the infiltration of meteoric water and potential for recharge to underlying groundwater resources (Hopmans and van Genuchten, 2005). The vadose (unsaturated) zone (Figure 2.1) is the region between the ground surface and the underlying water table, linking the atmosphere and groundwater. Pore spaces within the vadose zone are filled with air and water, with fluid pressure less than atmospheric pressure. The upper extent of the vadose zone consists of soil that hosts a dynamic environment where fluid and chemical fluxes constantly change due to evapotranspiration and meteoric flushing (Hopmans and van Genuchten, 2005). Underlying the soil are unsaturated sediments and/or rocks defining the lower extent of the vadose zone. The depth to the underlying water table (or more precisely to the capillary fringe, see below)

determines the vadose zone vertical thickness, which can vary typically from near-surface (< 1 m) to, quite rarely, a great depth (> 100's m) (Stephens, 1996). For instance, the greatest rooting depth of vegetation typically constrains the 'soil-zone' to 1-2 meters below the surface, whereas the location of the water table determines the thickness of the unsaturated sediments and/or rocks (Hopmans and van Genuchten, 2005).

The capillary fringe (Figure 2.1), also known as the tension-saturated zone, is a unique region where pore spaces are saturated from the underlying groundwater by capillary forces, but the fluid pressure is less than atmospheric pressure (Freeze and Cherry, 1979; Stephens, 1996). In the capillary fringe, groundwater is drawn upwards through small pores and capillary spaces in the soil and/or sediment due to capillary action. The thickness of the capillary fringe is controlled by the texture of the saturated media, with finer grained materials hosting larger capillary fringes (Freeze and Cherry, 1979; Stephens, 1996). The bottom of the capillary fringe marks the water table where fluid pressure is equal to atmospheric pressure, whereas below the water table is the saturated area where pore-spaces are completely filled with fluid, and fluid pressure is greater than atmospheric pressure (Freeze and Cherry, 1979).

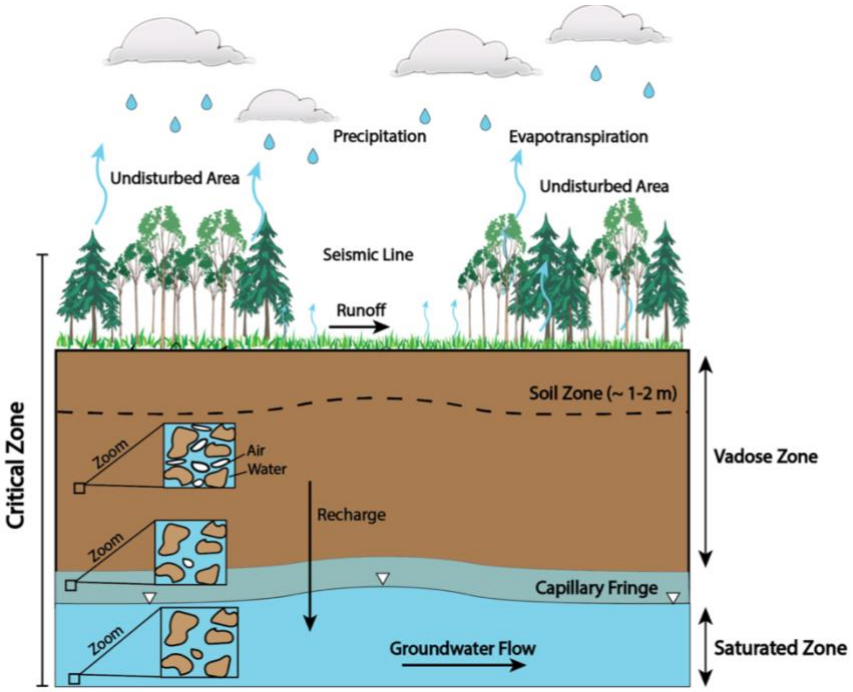

Figure 2.1: Cross-section of a generalized view of the sub-surface environment and the dominant hydrologic processes.

2.3.2 Chemistry

Understanding the chemical properties of the vadose zone is important for interpreting the fate and transport of chemicals in case of contamination. However, the vadose zone has a multitude of complex synergistic processes operating at various spatial and temporal scales, which complicate our understanding of the vadose zone (Hopmans and van Genuchten, 2005). Thus, studies observing the vadose zone require many small-scale field-measurements that can accurately delineate its complex nature (Flury *et al.,* 1994).

Physio-chemical weathering processes act to breakdown exposed bedrock resulting in an increased surface area of minerals (Pope, 2015). The exposed mineral surfaces are subsequently susceptible to chemical weathering via the interaction with meteoric water, which causes mineral dissolution resulting in solutes released into soil-water, precipitation of secondary minerals (i.e. clays), and eventually soil formation (Amundson *et al.,* 2007; Chorover *et al.,* 2011; White, 2014; Calabrese and Porporato, 2020; Kumaragamage *et al.,* 2021). Microbes and vegetation can subsequently inhabit the soils and produce CO_2 in the upper soil layers which in turn increases the chemical weathering of rocks and minerals via the production of carbonic acid (reactions 1 to 3) (Pennock, 2021).

$$H_2O + CO_2 \rightarrow H_2CO_3^0 \textbf{ (rxn. 1)}$$

$$H_2CO_3^0 \rightarrow HCO_3^- + H^+ \textbf{(rxn. 2)}$$

$$HCO_3^- \rightarrow {CO_3}^{2-} + H^+ \textbf{(rxn. 3)}$$

The intensity of chemical weathering within a soil profile generally decreases with depth (Pope, 2015); near-surface horizons (e.g. A, ~25-30 cm) show the greatest degree of weathering whereas the deeper B horizon (the following ~50 cm) shows some degree of weathering (but less than the A horizon) and the C horizon (the underlying ~45 cm) is minimally weathered closely resembling the bedrock on which the soil formed (White, 2014; Pennock, 2021). Chemical weathering of rocks is driven by a myriad of interconnected processes. Broadly speaking, the most important factors are time and the presence and

persistence of rock and mineral weathering agents such as water (Pope, 2015). Additionally, there are generally two pools of base cations in the soil: a small pool of exchangeable bases that are rapidly leached (e.g. swelling clays and organic matter) and a large pool of mineral bases that are slowly leached (i.e. dissolution of silicate minerals) due to the reaction kinetics (Schnoor and Stumm, 1986).

The variability of solute concentrations across a soil-profile depends on the residence time of water and the solid phases (including minerals) present in the soil (White, 2014). Generally, near-surface solute concentrations are lower due to a shorter interaction time between pore water and soil solids, but undergo considerable variations from various biological interactions, changing evapotranspiration fluxes, and hydrologic infiltration events (i.e. precipitation) (White, 2014). Conversely, solute concentrations increase with depth due to longer interaction time between pore water and soil solids, but exhibit less variation due to less soil water movement and biological processes (White, 2014). Shallow soil water residence times are typically less than 4 months whereas deeper soil water residence times are on the scale of years to decades (Langmuir, 1997; Pope, 2015). Soil hydraulic parameters that retard the movement of water (i.e. fine textured soils with low hydraulic conductivity) allow for more interaction time between minerals and soil-solution, which leads to a build-up of solutes and potentially the formation of secondary solid phases (White, 2014; Pope, 2015). Conversely, soil-parameters favoring higher water fluxes may flush out water-soluble products from the vadose zone resulting in a reduction of concentrations of weathering products in the soil.

Vegetation and micro-organisms in soil also influence soil weathering processes, biogeochemical cycling, and soil-water transport and fluxes, all of which are important for weathering and soil-formation (Drever, 1994; Berner *et al*., 2003). The presence of vegetation and their associated micro-biota act to increase overall weathering rates in the soil in numerous ways (Schwartzman and Volk, 1989; Drever, 1994; Pope, 2015): (i) binding fine

soil-particles increasing mineral surface area and soil-water residence times (Drever, 1994); (ii) lowering soil pH via root and microbial respiration producing CO_2 and/or generation of organic acids (Drever, 1994; Berner *et al*., 2003; Pope, 2015); (iii) root penetration providing preferential flow pathways and increased mineral surface areas (Drever, 1994; Berner *et al*., 2003; Pope, 2015); (iv) organic acid production and compounds from the decay of organic matter or root exudation resulting in a lower pH (Berner *et al*., 2003); (v) chelating agents that mobilize soluble metal complexes as well as alter nutrient exchanges (Drever, 1994; Berner *et al*., 2003); (vi) uptake of water and solutes in the rhizosphere resulting in changes of ion concentrations in soil solution (Berner *et al*., 2003); (vii) nutrient cycling: uptake of nutrients from minerals undergoing dissolution (e.g. Ca, Mg) by trees is mostly (> 90%) returned to forest litter where it is recycled back into the soil to be used by plants (Berner *et al*., 2003); and (ix) tall forest canopies can shade the soil surface, decreasing its temperature and surface albedo (Kelly *et al*., 1998). Thus weathering rates are complex and vary within a region depending on the plant species present, age of the stand, climate, rock type, and soil type (Berner *et al*., 2003). For example, a field study of a high-elevation watershed in north-central Colorado, (Arthur and Fahey, 1993) attributed increased weathering rates under forests to H^+ secretion from roots during nutrient uptake and production of organic acids in forest soils.

Subsurface root distribution is generally constrained to the upper 30 cm of a soil profile, however this can extend deeper (depending on the vegetation present) providing enhanced soil-porosity and a reserve water supply during periods of drought (Moore *et al*., 2015). Different vegetation types can modify soil properties in the uppermost soil horizon (i.e. A horizon) due to their rooting properties which in turn alter the water balance, chemical weathering and solute fluxes, in a soil profile (Páez-Bimos *et al.,* 2023). However, soil-water-vegetation interactions are complex and require further research. For example, in regions with low seasonality in precipitation and low evaporation rates, soil water flux and storage is largely explained by the physical and hydraulic properties of soils rather than properties of the

overlying vegetation (Geris *et al*., 2015). Conversely, Metzger *et al*. (2017) observed that variations in soil properties (i.e. structure) caused by vegetation (i.e. proximity to trees) can control spatial variations in soil water content and pH in humid climates.

2.4 Simultaneous Heat and Water (SHAW) Model

Soil-Vegetation-Atmosphere-Transfer (SVAT) models are increasingly used to better understand near-surface hydrological processes. The simultaneous heat and water (SHAW) model is a SVAT model developed in 1989 (Flerchinger and Saxton 1989) and has evolved into a vertical one-dimensional hydrologic model capable of simulating water, solute, and heat transfer within a system extending from the plant canopy (Flerchinger and Pierson 1997) to any specified soil-depth (Figure 2.2). The model combines snow, residue, soil, and plant canopy physics into a single solution, while calculating interrelated water, heat, and solute fluxes in the system. The model solves the exchange of heat and moisture within the soil simultaneously with the surface energy and mass balance. Infiltration is modeled using the Green and Ampt (1911) method, whereas the Richards' equation is employed to describe the movement of water through the soil layers (Gosselin *et al*. 2016). When precipitation surpasses the infiltration capacity of the soil, runoff will occur. The process of actual evaporation is directly incorporated into the energy budget equation, without relying on potential evaporation.

The user specifies the number of plant canopy layers, soil-simulation depths and defines the lower boundary of the system with initial soil-temperature and moisture conditions (Flerchinger 2017a). The upper boundary of the system is defined with user-supplied meteorological data containing precipitation, solar radiation, wind speed, air temperature and relative humidity and must be above any anticipated plant canopy height. Precipitation determines the water input into the system. The model initially calculates flux in the upper boundary followed by the heat, water, and vapor flux between layers and lastly the simultaneous calculation of heat and water flux through the entire system, where all fluxes are

defined as positive towards the surface. The basic equations relevant to this study are outlined below in this section, however, further details of the numerical parameters and assumptions the SHAW model uses are specified in the SHAW user's manual (Flerchinger 2017a).

2.4.1 Energy and Water Fluxes at the Upper Boundary

Water and energy fluxes are interrelated and computed with Equation (2.1) using the site-specific meteorological data where R_n is net radiation (W m^{-2}), H is sensible heat flux (W m^{-2}), L_vE is latent heat flux (W m^{-2}), L_v is evaporation latent heat (J kg^{-1}), E is the total evapotranspiration of the multi-layer system (kg m^{-2} s^{-1}), and G is subsurface conductive heat flux (W m^{-2}) (Flerchinger 2017a).

$$\boldsymbol{R_n + H + L_vE + G = 0} \textbf{ (Eqn 2.1)}$$

Net radiation is calculated as a function of the observed total incoming solar radiation. The net radiation that each layer within the system absorbs depends on 1) the amount of incoming solar radiation and 2) transmission and absorption of longwave and net radiation within each layer. Longwave radiation is calculated from the combination of measured ambient air temperature and daily average cloud cover calculated from measured net radiation (Flerchinger 2017a). Plant canopy transmission of radiation is influenced by leaf orientation, leaf area index, leaf albedo, and soil-surface albedo (Flerchinger 2017a).

Sensible and latent heat fluxes (Equations 2.2-2.3) between the soil-plant canopy-residue and the atmosphere are computed from temperature and vapor gradients (Flerchinger 2017a). The latent heat flux quantifies the movement of water vapor from the exchange surface to the atmosphere. With these variables known, the model computes the ground heat flux by simultaneously solving the heat flux equations for the entire soil profile along with the surface energy balance. This calculation is performed iteratively, with the ground heat flux obtained as a residual to ensure that the heat flux equations (Equations 2.2-2.3) are satisfied. Sensible and latent heat fluxes are calculated separately by the model at the upper boundary with vapor gradients between the soil-residue-canopy surface and atmosphere along with

ambient temperature. Sensible heat flux is calculated via Equation (2.2) where $\rho_a, C_a,$ and T_a are the density (kg m^{-3}), specific heat (J^{-1} kg^{-1}) and temperature (°C) of air at the measurement reference height, T is the temperature (°C) of the exchange surface, and r_h is the resistance to surface heat transfer (s m^{-1}) corrected for atmospheric stability.

$$\boldsymbol{H = -\rho_a C_a \frac{(T - T_a)}{r_h}} \textbf{ (Eqn 2.2)}$$

Latent heat flux is calculated via Equation (2.3) where ρ_{vs} and ρ_{va} are vapor density (kg m^{-3}) of the exchange surface and at the reference height and the resistance value for vapor transfer, r_v describes the transfer of water vapor from the exchange surface to the atmosphere and is taken to be equal to r_h. Lastly, the subsurface conductive heat flux (G) is calculated as a residual from Equation 2.1.

$$\boldsymbol{L_v E = \frac{(\rho_{vs} - \rho_{va})}{r_v}} \textbf{ (Eqn 2.3)}$$

2.4.2 Transpiration and Evaporation

The model assumes transpiration ceases when solar radiation is < 10 W/m^2 or when the ambient air temperature is less than a specified minimum amount for a given plant to transpire at which point plant stomates close and there is no vapor transfer from the plant canopy (Flerchinger 2017a). The model uses Equation (2.4) to calculate transpiration for a specified plant species where T is total transpiration rate (kg m^{-2} s^{-1}) for a given plant species, $\varphi_r, \varphi_l,$ and φ_s are the water potentials (m) for the roots, leaves, and soils respectively, R_{sr} and R_{rl} are the resistance to water flow (m^{-3} s kg^{-1}) through the roots of soil layer and leaves of the canopy layer, L is the leaf area index for the given plant species, ρ_{vs} is the vapor density (kg m^{-3}) within the stomata cavities (assumed to be saturated vapor density), ρ_v is the vapor density of air within the canopy layer, r_s is stomata resistance per unit of leaf area index (s m^{-1}), and r_h is resistance to conductive transfer within the layer per unit of leaf area index (s m^{-1}).

$$T = \frac{\varphi_s - \varphi_r}{R_{sr}} = \frac{\varphi_r - \varphi_l}{R_{rl}} = \frac{\rho_{vs} - \rho_v}{r_s + r_h}$$ **(Eqn 2.4)**

Water flow within the plant is controlled mainly by changes of stomatal resistance. Neglecting other effects, Equation (5) relates stomatal resistance to leaf water potential, where r_{so} is stomata resistance (s m^{-1}) with no water stress (assumed constant), φ_c is a critical leaf water potential (m) at which stomata resistance is twice its minimum value, and n is an empirical coefficient which the model sets to a value of 5.0.

$$\boldsymbol{r_s = r_{so}\left[1 + \left(\frac{\varphi_l}{\varphi_c}\right)^n\right]}$$ **(Eqn 2.5)**

The model calculates evaporation from the plant canopy via actively transpiring leaves with excess water on them or standing dead plant material via Equation (2.4) where the stomatal resistance is assumed to be zero.

2.4.3 Soil Hydraulic Properties

The hydraulic parameters of each simulation node are estimated using the method outlined by Saxton *et al*. (1986). Measurements of soil textural properties, bulk density, and organic matter content are used to estimate soil-hydraulic properties via Equations (2.6) and (2.7) after Campbell (1974). Soil unsaturated conductivity was calculated via Equation (2.6) where K_u is the unsaturated conductivity, K_s is the saturated conductivity, φ_e is the air entry potential (m), φ_s is the soil matrix potential (m), and b is the pore-size distribution parameter.

$$K_u = K_s\left(\frac{\varphi e}{\varphi_s}\right)^{2+3/b}$$ **(Eqn 2.6)**

The soil-water characteristic curve was calculated via Equation (2.7) where θ_s is the saturated water content, θ is the volumetric water content, φ_e is the air entry potential (m), and φ_s is the matrix potential (m) (Campbell 1974). This curve is used to calculate matric potential for unsaturated conditions from measured soil-water content (Flerchinger 2017a).

$$\boldsymbol{\varphi_s = \varphi_e\left(\frac{\theta}{\theta_s}\right)^{-b}}$$ **(Eqn 2.7)**

2.4.4 Soil Water Balance

The soil-water balance can be expressed using equation 2.8 where all units are in mm and P is precipitation, ET is evapotranspiration, DP is deep percolation, R is runoff, and ΔS is the storage term.

$$\boldsymbol{P - ET - DP - R - \Delta S = 0} \textbf{ (Eqn 2.8)}$$

The storage term (equation 2.9) comprises snow remaining at the end of the simulation, water retained on plant litter (residue) and the plant canopy, and soil water storage where positive values indicate soil-water has been gained whereas negative values indicate a loss of soil water.

$$\boldsymbol{\Delta S = snow + residue + plant\ canopy + soil\ storage} \textbf{ (Eqn 2.9)}$$

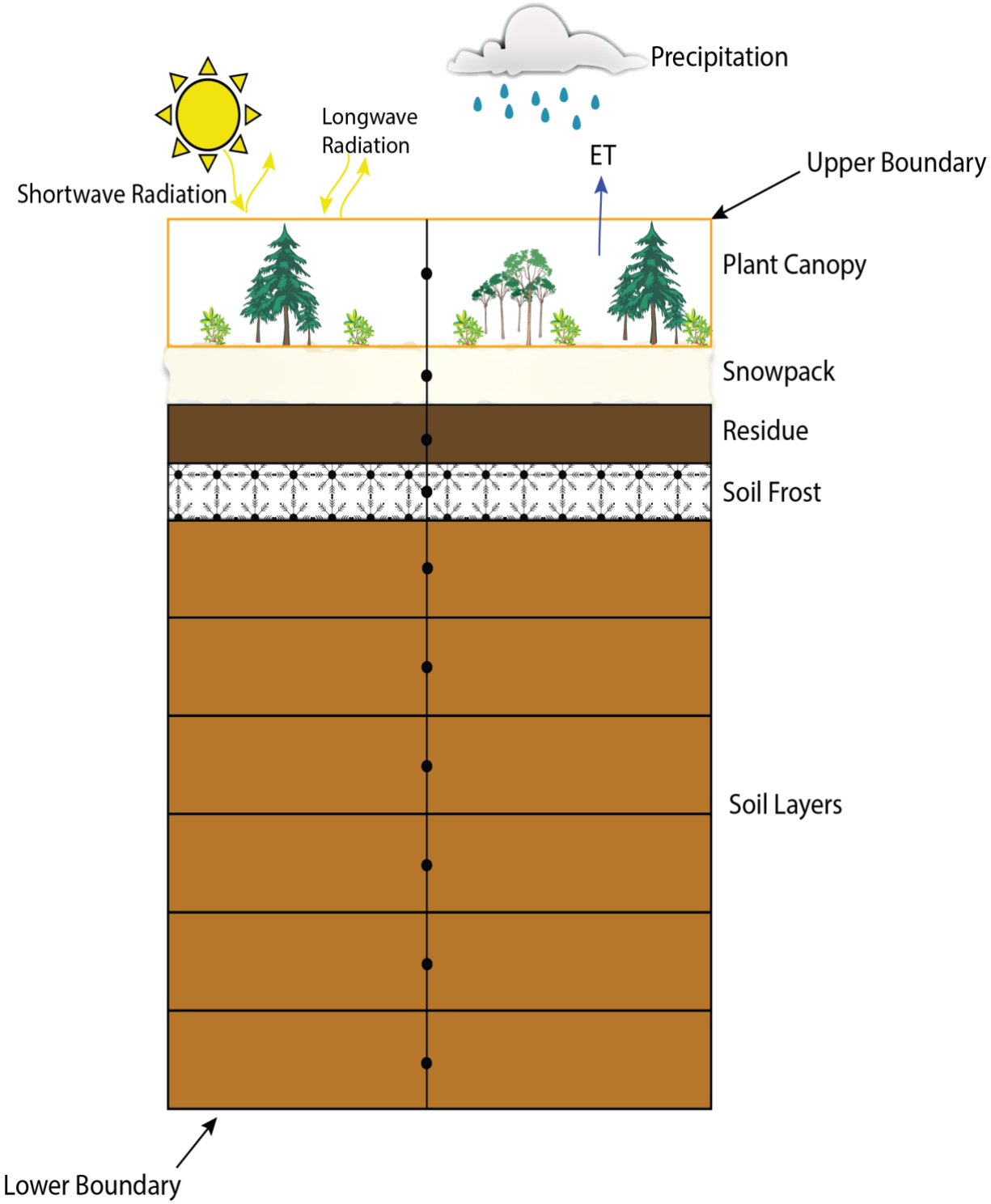

Figure 2.2: Conceptual diagram of the SHAW model after Flerchinger (2017a).

Chapter 3 Methods

3.1 Field Work and Targeted Analyses

A paired site model was used for this study and site selection was made accordingly. A site was thus composed of two distinct locations: one was placed in an area with a seismic line cutting through a forest (a disturbed site) and the other was at least 20 meters away from the edge of the first site, in the adjacent natural undisturbed area (an example is provided in Figure 3.1). This approach allowed for the comparison of the hydrology and ecosystem in areas disturbed by industrial activities and their undisturbed natural analogs. Site selection criteria included: proximity to previously established groundwater monitoring wells by GSC, soil and ecosite type, elevation, and year-round accessibility. From the initial selection of 12 sites, five sites were selected after a field visit: three in upland ecosites (U1 to U3) and two in lowland ecosites (L8 and L12) and monitoring equipment was installed at these sites in June 2021 (Figure 3.2).

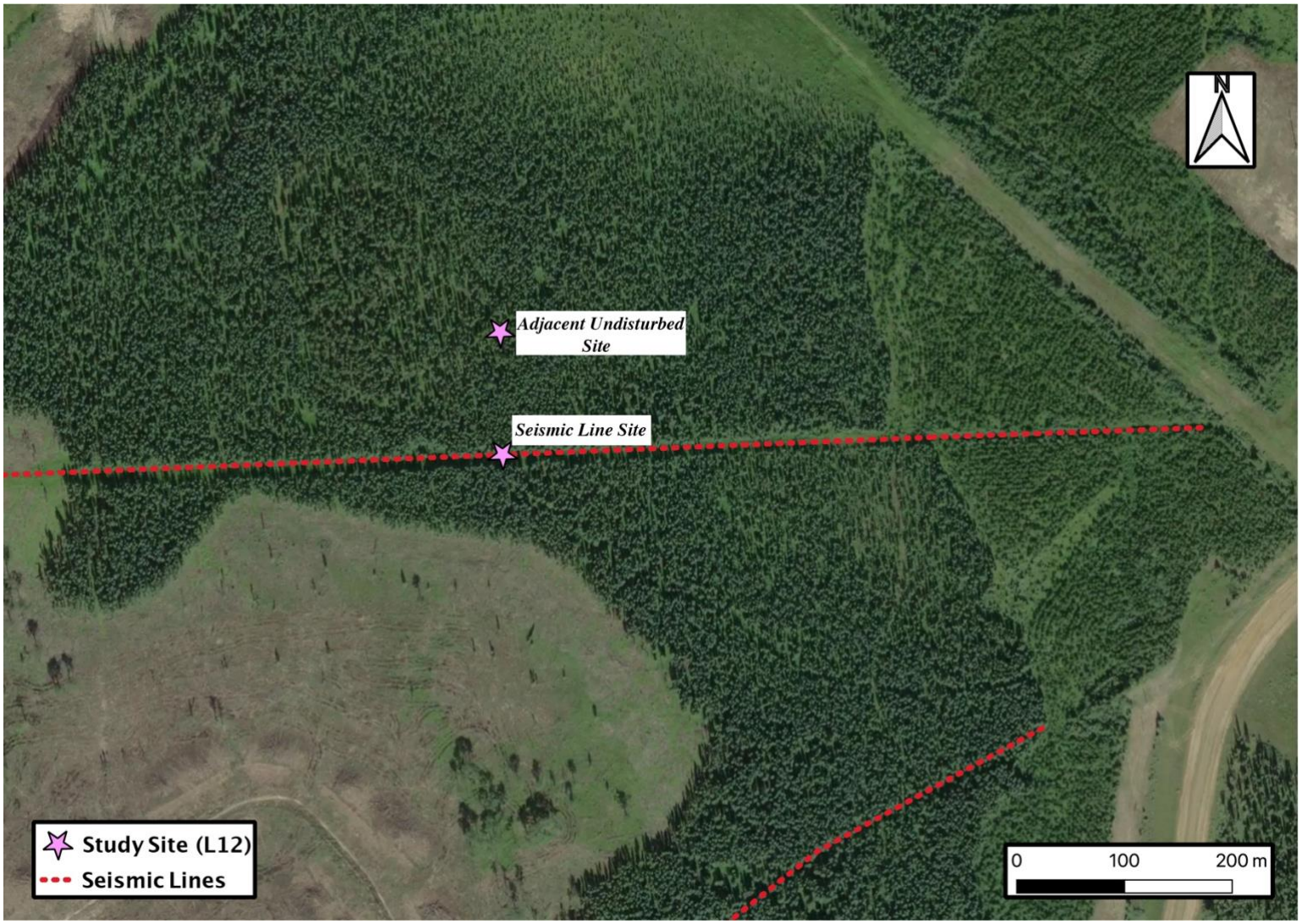

Figure 3.1: Example of the locations of the instrumentation being installed at each paired site.

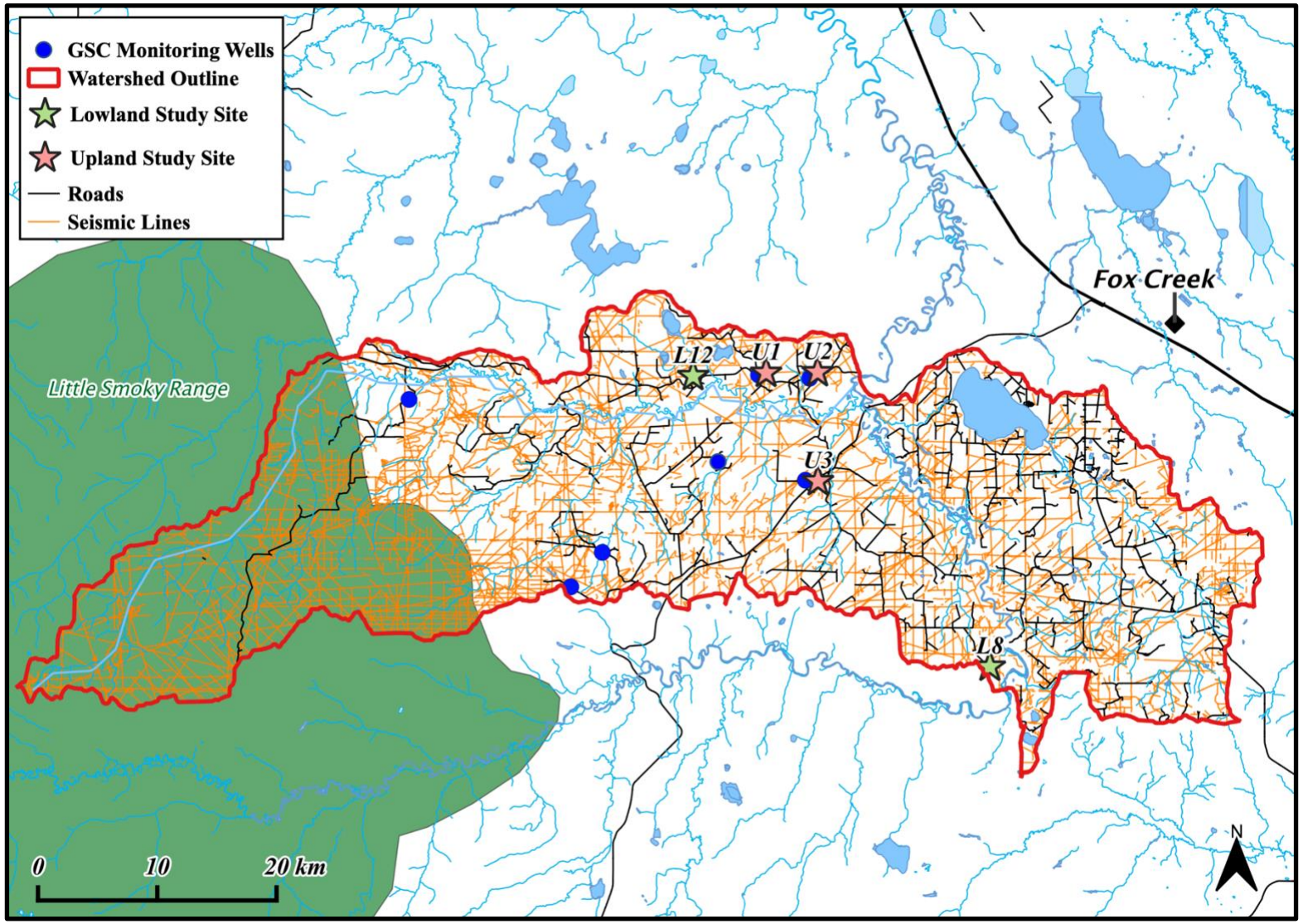

Figure 3.2: Map of the field sites chosen for this study.

Equipment installed (June 2021) on all sites included: rain gauges, suction-lysimeters and soil moisture/temperature probes at varying depths. Rain gauges were installed on all the seismic line sites to monitor cumulative monthly precipitation and were filled with ~ 1 cm of paraffin to minimize evaporative losses. Winter precipitation was measured via snow-sampling by measuring snow-pack thickness and density at each visit. Suction lysimeters were installed at depths of 30 cm, 60 cm, and 120 cm to extract soil water for the analysis of soil solution chemistry. The lysimeters at 30 and 60 cm were removed in November for the winter season to avoid damaging them. Bulk soil sampling during the installation of the equipment was performed at intervals of 0-15 cm, 15-30 cm, and 30-60 cm to obtain baseline physical (including grain-size analysis), chemical, and mineralogical characterizations of the soil in the watershed.

Data loggers (Meter Group, ZL6 data loggers) were installed at each site with soil moisture and temperature sensors (Meter Group, TEROS 10 and 5TM sensors) at 15, 30, and 60 cm depths to monitor soil water content and soil temperature. Their operating range is from -40°C to 60°C for soil temperature and a SWC of 0% to 70% for mineral soils (METER, 2021) (Table 3.1).

Table 3.1: Accuracy of TEROS 12 Soil Moisture and Temperature Sensor (METER, 2021).

Parameter		Accuracy
SWC		*± 3.0%*
Soil Temperature	0°C to - 40°C	*± 0.5°C*
	0°C to 60°C	*± 0.3°C*

Vegetation surveys were also performed at each site to help identify the most abundant plant species on the seismic lines and their adjacent undisturbed areas. Lastly, two water collectors dedicated to collecting meteoric water and minimizing possible isotopic fractionation were installed to develop a local meteoric water line for the watershed through collection of monthly cumulative precipitation.

In April 2022, 2-m-tall weather stations were installed in pairs on two sites (at Site U1 in the uplands, and at Site L8, in the lowlands) to collect the data necessary for numerical modeling, one on a seismic line and one in the adjacent undisturbed area (Figure 1.7). The weather stations contain the following equipment: Hobo U30 Data logger, 5-W solar panel, Davis wind speed and direction sensor, temperature/relative humidity sensor, silicon pyranometer sensor (solar radiation), and a Davis rain sensor. The data logger was initialized to record data on an hourly basis. Monthly leaf area index (LAI) measurements were obtained for the overstory (trees) and understory (grasses/shrubs) vegetative canopy from August – October 2022 at each site using a LAI-2200C Plant Canopy Analyzer. Field visits were conducted almost every month from June 2021 to January 2023. See Table A1 in the appendix for a summary of the monitoring equipment installed at all sites.

The analysis for all precipitation and interstitial water samples includes, in addition to the water isotopes: total organic carbon (TOC), dissolved organic carbon (DOC), trace metals, and major ions. $\delta^2 H$ and $\delta^{18} O$ isotope data were compared with meteoric values to understand groundwater-precipitation relationships and the relative influence of evapotranspiration. Sediment samples were used for grain-size analysis.

3.2 Vegetation Surveys and Study Site Descriptions

The seismic line properties (orientation and width) and ecosite types for all study sites are summarized in Table 3.2 Vegetation surveys were performed at all study sites to identify the most abundant plant species among the seismic lines and adjacent undisturbed areas in the upland and lowland ecosites. At each paired site, six 30 cm x 30 cm vegetation survey plots were analyzed. On the seismic lines, 4 plots were from the seismic line edges and 2 plots from seismic line centers, whereas plot locations in the adjacent undisturbed areas were randomly chosen and were 20 m away from the edge of the seismic line. Tree heights for an upland site (U1) and a lowland site (L8) were measured using a hypsometer.

Table 3.2: General study site characteristics. Sites labelled with U and L indicate upland and lowland sites respectively.

Site	Ecosite	Elevation (m)	Seismic Line Width (m)	Seismic Line Orientation (°)
U1	Upland low-bush cranberry (Aw)	885	8.3	78
U2	Upland low-bush cranberry (Aw)	870	6.2	76
U3	Upland low-bush cranberry (Aw)	875	6.2	72
L8	Lowland horsetail (Sw)	910	6.2	76
L12	Lowland horsetail (Sw)	850	6.9	73

3.3 Soil Solids Methods

A 60-cm deep soil-pit was dug at each site and soil-samples were obtained at 15, 30, and 60 cm depths using a soil-core sampler of known volume (140 cm^3). The LFH layer (i.e., organic soil horizons developed primarily from the accumulation of leaves, twigs and woody materials) was removed prior to sampling. Samples were stored in Whirl Pak bags, sealed, and weighed prior to placing them in a drying oven in tin-foil pans. The samples were left to dry at 70°C for ~72 hrs and reweighed multiple times ensuring they were fully dried. Following the complete drying of the samples, bulk density was calculated using equation 3.1 where ρ_b is the dry bulk density in kg/m^3, the weight of oven dried soil is in kg and the volume of soil is in m^3.

$$\boldsymbol{\rho_b = \frac{weight\ of\ oven\ dried\ soil}{volume}} \textbf{ (Eqn 3.1)}$$

Soil texture analysis was performed at Institut national de la recherche scientifique (INRS) where the samples were first sieved to remove particles > 2 mm and subsequently treated in an immersion of 30% H_2O_2 for one or more cycles to remove organic matter.

Approximately 10 mL of sodium hexametaphosphate $(NaPO_3)_6$ was added as a deflocculant to the solution, which was passed through an ultrasonic bath just before being analyzed with a Beckman Coulter LS 13 laser granulometer (Beckman Coulter Inc., Brea, CA, USA). At least 3 successive measurements were made on each sample and the average of these measurements was used to calculate the particle size parameters using the GRADISTAT software (Blott and Pye, 2001).

X-Ray diffraction (XRD) analysis was conducted at the University of Alberta to identify the mineral phases present in the soil samples. Soil samples collected from each depth interval at each site were passed through a 45-μm filter and subsequently mounted in 2 mm deep alumina pits prior to being analyzed using a Rigaku Ultima IV instrument. Data were converted using JADE MDI 9.6 software and phase identification was done using DIFFRAC.EVA software with the 2021 ICDD PDF 4+ and PDF 4+/Organics databases. Machine acquisition parameters used are available in Appendix B.

Soil pH was determined using the soil-to-water extraction method (Kalra and Maynard, 1991) where dry soil is mixed with water and placed on a reciprocating shaker for 1 hour. This mixture is then filtered using Büchner funnels and the resulting filtrate is measured for pH, EC, and water-soluble ions on the ICP-OES. Cation exchange capacity (CEC, cmol (+) / kg) was measured by the ammonium chloride method using a mechanical vacuum extractor (Kalra and Maynard, 1991). Soil total carbon (TC) and total inorganic carbon (TIC) content were measured with a Leco 828 CHN Analyzer via the Dumas Method using dry combustion with IR detection and expressed in % dry weight of soil (Kalra and Maynard, 1991). Percent soil organic matter (SOM) was subsequently calculated using equation 3.2 (Quideau *et al.,* 2021).

$$\% \text{ SOM} = 1.72 \times \% \text{ SOC} \quad \textbf{(Eqn 3.2)}$$

3.4 Soil Water and Precipitation Analysis Methods

Suction lysimeters were thoroughly cleaned prior to installation using 10% HCl and deionized water (Weihermüller *et al*., 2006). A handheld Dutch auger was used at each paired site to auger 30, 60, and 120 cm deep holes which were partially filled with a slurry mixture of deionized water and extracted soil prior to placing the suction lysimeters into the hole and backfilling with residual soil. Subsequently, upon each monthly site visit (when ground temperature was above 0°C), the suction lysimeters were evacuated of air using a vacuum pump by pressurizing to ~60 kPa and sealed allowing soil-water to accumulate in the suction lysimeters for ~ 4 to 24 hours depending on the soil-moisture. The accumulated soil-water was obtained using a sample extraction kit containing an Erlenmeyer flask and tubing was used to collect soil-water samples into clean 250 mL HDPE bottles. Soil-water sampling was limited from May to October due to frozen soil conditions during the winter months and difficulties in sample collection. It should be noted that a suction lysimeter samples a mixture of free soil water that is present at or over the soil's field capacity and soil pore water (Landon *et al*., 1999).

Soil-water samples were titrated using a Metrohm 905 Titrando at the University of Alberta to determine their alkalinity. To avoid degassing of CO_2, soil water samples were titrated within 48 hrs of sampling. All sample initial pH values were below 8.3 indicating bicarbonate is the major contributor the total alkalinity and phenolphthalein alkalinity is negligible (Jenkins and Moore, 1977). Samples were titrated with a 0.1 M HCl solution until a pH of 4.3 was reached at which point the titration was stopped. Equation (3.3) from (AWWA, n.a.) was used to calculate the total alkalinity. Samples with low alkalinity values (< 20 mg $CaCO_3$/L) were listed as below detection limit. Although alkalinity for such samples can be determined via the low alkalinity titration methods (AWWA, n.a.), sufficient sample volume was not present to achieve this.

$$\boldsymbol{Total\ Alkalinity, \frac{mg}{L}\ CaCO_3 = \frac{mL\ acid\ added * Acid\ Normality * 50{,}000}{mL\ sample}} \quad \textbf{(Eqn 3.3)}$$

Soil water and rainwater samples were analyzed for major cations and trace metals at the University of Alberta using an Agilent 8800 ICP-MS/MS. Eleven standards were prepared in a matrix of 2% HNO_3 covering a range of 0.005-300 mg/L to capture varying elemental concentrations within the samples. Samples were filtered with a 45 μm nylon membrane and analyzed in a 2% HNO_3 matrix. The ICP-MS/MS measurements were made using several collision/reaction gases to eliminate isobaric interferences (Table 3.3). Indium was used as an internal standard to account to instrumentation drift for each analysis covering all collision/reaction gas cells.

Table 3.3: Measured elements, MS/MS masses, and used collision/reaction gases.

Element	Q1 → Q2	Gas	Element	Q1 → Q2	Gas
Li	7 → 7	-	Fe	56 → 56	H2
B	11 → 11	-	Co	59 → 59	He
Na	23 → 23	He	Ni	60 → 60	He
Mg	24 → 24	He	Cu	63 → 63	He
Al	27 → 27	He	Zn	66 → 66	He
P	31 → 47	O2	As	75 → 91	O2
S	32 → 48	O2	Sr	88 → 88	He
K	39 → 39	He	Mo	95 → 95	He
Ca	40 → 40	H2	Cd	114 → 114	He
Cr	52 → 52	He	Ba	137 → 137	He
Mn	55 → 55	He	Pb	208 → 208	-
Fe	56 → 56	He	U	238 → 238	-

Soil-water anions were quantified via a colourimetric technique using a Thermo Gallery Plus Beermaster Autoanalyzer at the Natural Resources Analytical Lab (NRAL) at the University of Alberta. Counter-ions measured included SO_4-S, NO_3-N, NO_2-N, Cl^-, PO_4-P, and NH_4-N via well-known color reactions (see appendix Table A1). Samples and method reagents are injected into reaction cuvettes combining to generate colored complexes. The degree of color change in the solution correlates with the analyte concentration in the sample and is measured via light absorbance at a specific wavelength as quantified by the Beer-Lambert law.

$$A_\lambda = \varepsilon_\lambda l c \quad \textbf{(Eqn 3.4)}$$

where: A_λ is the absorbance of light at the target wavelength, ε_λ is the extinction coefficient of the colour complex at that wavelength, l is the path length of the cuvette in cm, and c is the concentration of the analyte in solution. Certified standard solutions are used for calibration, and separate certified solutions are used as external reference and check standards.

Total organic carbon (TOC), TIC, dissolved organic carbon (DOC) and dissolved inorganic carbon (DIC) analysis were conducted at the NRAL laboratory at the University of Alberta using a Shimadzu TOC-L CPH Model Total Organic Carbon Analyzer which was calibrated with known standard materials. Soil-water samples to be analyzed for TOC/TIC were filled in 50 mL centrifuge tubes unfiltered whereas those to be analyzed for DOC were filtered via 0.45 μm nylon membranes and stored in a chilled cooler during transportation. TOC was measured as non-purgeable organic carbon (NPOC) by acidifying a sample of soil-water using 1 M HCl, then sparging the sample to remove any purgeable organic and inorganic carbon. The sample was then injected into a combustion tube that is kept at 720 °C containing platinum catalyst beads, where a subsequent redox reaction occurs that evolves CO_2 gas which is detected by a non-dispersive infrared (NDIR) detector for NPOC. TIC was measured by injecting a sample into a bubble chamber and reacting it with 25% phosphoric acid. The acid reacts with inorganic carbon to form CO_2 which is sent to the NDIR detector for TIC analysis by bubbling air through the sample.

In this study, cumulative monthly precipitation was sampled from July 2021 to November 2022. During the winter months, snow was sampled in Ziploc bags and I attempted to collect fresh snowfall samples to avoid isotopic fractionation of the sample. Rainwater was collected in a simple rainwater collector, outlined in Gröning *et al.* (2012), designed to prevent evaporation fractionation and a plastic container with a funnel on top and a drain on the bottom filled with ~1 cm paraffin oil to prevent evaporative losses. Collection of soil water via the ceramic porous cup of the suction lysimeters has been shown to not cause isotopic fractionation (Wenner *et al.,* 1991).

Upon monthly sampling of rain and soil water, samples were passed through a 0.2 μm nylon membrane into 2.0 mL plastic vials ensuring no head space to prevent possible isotopic fractionation. Water samples collected from the suction lysimeters, rainwater samplers, and snow were analyzed for $\delta^{18}O$ and $\delta^{2}H$ stable isotope ratios at the University of Alberta using a Picarro L2130-i analyzer. Measured isotope values were reported relative to the Vienna Standard Mean Ocean Water-Standard Light Antarctic Precipitation (VSMOW-SLAP). Analytical error (2σ) *is* < 1.0 ‰ for $\delta^{2}H$ and < 0.3 ‰ for $\delta^{18}O$.

The global meteoric water line (GMWL) (Equation 3.5) describes the mean worldwide relationship between $\delta^{2}H$ and $\delta^{18}O$ isotope ratios for meteoric waters (Craig, 1961).

$$\delta^{2}H = 8\ \delta^{18}O + 10\ ‰ \quad \textbf{(Eqn 3.5)}$$

To account for the world-wide spatial variability of the $\delta^{2}H$ and $\delta^{18}O$ isotopic composition in meteoric waters, a local meteoric water line (LMWL) for the watershed in this study was determined by analysis of $\delta^{18}O$ and $\delta^{2}H$ stable isotopes from monthly precipitation samples (Equation 3.6), where a is the slope and b is the y-intercept.

$$\delta^{2}H = a\ \delta^{18}O + b \quad \textbf{(Eqn 3.6)}$$

Furthermore, the isotopic composition of soil-water samples was compared to the LMWL using the line-conditioned excess (LC-excess) Equation 3.7 (Landwehr and Coplen, 2004). LC-excess is a generalized form of the LMWL where a and b are the coefficients from the LMWL for a region.

$$\text{LC-excess} = \delta^{2}H - a \times \delta^{18}O - b \quad \textbf{(Eqn 3.7)}$$

LC-excess is a useful way to screen the degree of deviation from the LMWL for a water sample within that region. For instance, a negative LC-excess value indicates the water has undergone evaporative enrichment relative to the LMWL, whereas a positive LC-excess value potentially indicates a different moisture source (Landwehr and Coplen, 2004).

3.5 Measured Weather Parameters

The weather stations installed at sites U1 and L8 in April 2022 measured net radiation, temperature, relative humidity, wind speed, and precipitation. A tipping bucket type rainwater collector installed on the weather stations was used to collect liquid precipitation data from May to October 2022. During the winter months, snow-surveys were conducted from November 2022 to April 2023 to determine the amount of precipitation using snow water equivalent (SWE). To better characterize the snow conditions within the watershed, snow-depth and snow-density were measured on site and snow samples were collected and the trace elemental content analyzed monthly throughout the winter to estimate SWE. Snow surveys were conducted monthly from November 2021 to April 2022 at all study sites and from December 2022 to February 2023 at sites 1 and 8 (U1 and L8), where the weather stations had been installed. During each field-visit, the snowpack was excavated using a shovel, its thickness was measured with a tape-measure, and snow samples were collected using a PVC tube (diameter = 4.0 cm and length = 0.3 to 1.5 m) with a sharpened tip and deposited within a pre-weighed plastic bag. The snow-density of the collected samples was calculated by subtracting the empty plastic bag mass from the snow-filled bags via equation (3.8), where ρ_s is the density of the snow, m is the snow sample mass, and V_{pvc} is the volume of the PVC sampling device. To aid in a future NRCan caribou study based on remote sensing, monthly snow density data was collected from the upper 5 to 10 cm of the snowpack, in addition to total snowpack. During each site visit, four replicate samples were collected on the seismic line and the adjacent undisturbed area to account for spatial variations within a site.

$$\boldsymbol{\rho_s = \frac{m_s}{V_{pvc}}} \textbf{ (Eqn 3.8)}$$

An approximate monthly SWE can be calculated for the various study sites within the watershed using the measured monthly snow depths and total snowpack densities via

Equation (3.9) where ρ_s is the measured total snowpack density and t_s is the measured snowpack thickness.

$$\boldsymbol{SWE = \rho_s * t_s} \textbf{ (Eqn 3.9)}$$

3.6 SHAW Model Parametrization

A total of four 1D models were developed: one for the undisturbed areas and one for the seismic lines (disturbed) areas for sites U1 and L8.

3.6.1 Model Calibration

In prior studies, the SHAW model has been used successfully without calibration (Flerchinger and Hanson 1989; Flerchinger and Pierson 1991; Flerchinger *et al.* 1996, 1998; Link *et al.* 2004; Kang *et al.* 2005; McNamara *et al.* 2005). However, when accurate estimation of certain parameters is crucial or certain critical input parameters are not available, the model has been calibrated to improve simulation accuracy (Flerchinger and Pierson 1997; Flerchinger and Hardegree 2004; Huang and Gallichand 2006; Yin *et al*. 2010a, b). To obtain accurate estimates of ET, calibration of net-solar radiation and soil-water content is imperative (Flerchinger *et al*., 2012).

The SHAW model was manually calibrated with respect to net radiation and soil-moisture by comparing actual values with simulated ones and attempting to minimize the root mean square deviation (RMSD, also called root mean square error, RMSE). The simulation period was from May 2022 to May 2023. To assess model performance, the model efficiency (ME, also called the Nash-Sutcliff efficiency), which is a widely used statistic for assessing the goodness of fit of hydrologic models, root mean square deviation (RMSD), which is one of the most commonly used measures for evaluating the quality of predictions, and percentage bias error (PBIAS), that measures the average tendency of the simulated values to be larger or smaller than their observed ones, were calculated according to Equations 3.10 to 3.12 (Nash and Sutcliffe 1970; Green and Stephenson 1986; Yin *et al*. 2010a). N is the total number of

observations, X_i is the observed value at a given time step, $\hat{X}_i$ is the simulated value at a given time step, and $\overline{X_i}$ is the mean of the observed values (Yin *et al*. 2010a). ME describes the variation in measured values explained by the model with ME values from 0.0 to 1.0 being acceptable (1.0 is a perfect match between the model and observed data), while ME < 0.0 occurs when the observed mean is a better predictor than the model and, therefore, is considered an unacceptable performance (Yin *et al*., 2010). Lower values of RMSD indicate a better model performance. Lastly, PBIAS shows the percent deviation from model simulated values to the actual measured values. Negative values indicate a model bias of underestimation relative to the measured value, whereas positive values indicate a model bias to over-estimate the measured value. The ideal value for PBIAS is 1.0. Model parameters were calibrated within reasonable limits of each parameter (discussed in next sections).

$$\boldsymbol{ME = 1 - \frac{\sum_{i=1}^{N}(X_i - \hat{X}_i)^2}{\sum_{i=1}^{N}(X_i - \overline{X_i})^2}} \qquad \textbf{(Eqn 3.10)}$$

$$\boldsymbol{RMSD = \left[\frac{1}{N}\sum_{i=1}^{N}\left(X_i - \hat{X}_i\right)^2\right]^{0.5}} \textbf{(Eqn 3.11)}$$

$$\boldsymbol{PBIAS = \frac{1}{N}\sum_{i=1}^{N}\left(\hat{X}_i - X_i\right)} \quad \textbf{(Eqn 3.12)}$$

3.6.2 Study Area General Parameters

The SHAW model has numerous parameters pertaining to the characteristics of the study site, soil, and vegetation that need to be specified prior to initiating a simulation. Most parameters were determined at the field site, while some had to be estimated via literature. Site parameters used in the model for the study locations within the Fox Creek study area are listed in Table (3.4). Soil albedo and wind profile roughness values were derived from suggested values in the SHAW user's manual (Flerchinger 2017b).

Table 3.4: Site parameters used in the SHAW model.

Site Parameter	Study Site	
	U1	L8
Latitude	54° 23’	54° 21’
Slope (%)	2	2.7
Slope Aspect (°)	172.4	40.5
Elevation (m)	885	910
Wind Profile Roughness (cm)	1	1
Albedo of Wet Soil	0.3	0.3
Albedo of Dry Soil	0.15	0.15

Since the upper boundary of the model is limited by the height at which the weather data is collected, weather stations installed on seismic lines where the plant canopy is generally less than the height of the weather station (2 m) can provide appropriate simulations. However, weather data collected from the adjacent undisturbed areas are not suitable to use as the upper boundary as the plant canopy is 10 – 20 m high in these areas. Thus, for the adjacent undisturbed area sites, the climate data collected from the seismic line can be used if the wind conditions are similar among the seismic line and adjacent undisturbed area, which will be compared in section 4.5.3 [pers. commun. with Dr. Flerchinger].

3.6.3 Vegetation Parameters

The various plant parameters required by the model for these plants are listed in Table 3.5. Input parameters for plant transpiration are difficult to measure and usually need to be obtained via literature (Flerchinger *et al*., 2012). Stomatal and plant resistance values were set according to the recommended values outlined in the user’s manual (Flerchinger 2017b). Rooting depths were assigned via literature (Flinn and Wein 1977; Strong and La Roi 1983a, b). Typical albedo values for the various vegetation were derived from Betts and Ball (1997). Leaf water potential values were estimated via literature (Kaufmann 1975; Caplan and Yeakley 2010; Hébert and Thiffault 2011). Transpiration threshold temperature for plant species in the boreal forest is not well defined in literature and thus was left at the model default value of 7°C. Volumetric dry plant biomass was not measured and had to be estimated via various literature sources (Rutkowski and Stottlemyer 1993; Woo and Zedler 2002;

Hébert and Thiffault 2011; Proulx *et al*. 2015). The volumetric dry plant biomass estimates were within the range for typical plant communities within the boreal forest (Proulx *et al*. 2015). Values used for sites U1 and L8 in the SHAW model for the vegetative parameters are summarized in Table 3.5.

Sensitivity analysis revealed that adjustment of vegetative parameters, particularly plant albedo and, to a lesser extent, LAI had an impact on the simulated net radiation. Achieving a good net radiation calibration is imperative as it influences many other processes simulated by the model (Flerchinger *et al.*, 2012). Thus, plant albedo values were adjusted within a reasonable range (no more than ± 0.02 from literature recommended values) to improve the calibration. Leaf angle can be set between 1° (randomly oriented leaves) to 5° (horizontally oriented leaves.) Initially leaf angle was set to 1° and later altered to 5° to improve the net radiation calibration.

To improve transpiration simulations, LAI was measured from August to October at all sites (Table 3.6) because this parameter profoundly influences ET and canopy interception estimates. Since the simulation period is from May to September, LAI values for May were assumed to be the same as October, June the same as September, and July the same as August. To improve net radiation simulations LAI values would have had to be adjusted by at least one full unit to observe a noticeable effect on net radiation; hence, LAI measurements recorded in the field were used in modelling.

Table 3.5: Vegetative parameters used in the SHAW model for the U1 and L8 study sites. The following values were estimated from literature: plant albedo (Strong and La Roi 1983a), rooting depths (Flinn and Wein 1977; Strong and La Roi 1983a, b), stomatal resistance (Flerchinger 2017b), leaf water potential (Betts and Ball 1997; Caplan and Yeakley 2010; Hébert and Thiffault 2011), and dry plant biomass (Rutkowski and Stottlemyer 1993; Woo and Zedler 2002; Hébert and Thiffault 2011; Proulx *et al*. 2015).

Plant Parameter	Site U1			Site L8		
	Seismic Line	Undisturbed		Seismic Line	Undisturbed	
	Rubus parviflorus (understory)	*Populus balsamifera* (overstory)	*Rubus parviflorus* (understory)	Graminoids (understory)	*Picea mariana* (overstory)	*Rhododendron groenlandicum* (understory)
Plant Height (m)	1	38.1	0.9	0.5	14.1	0.65
Volumetric Dry Plant Biomass (kg/m^3)	0.25	0.45	0.25	0.10	0.42	0.28
Plant Albedo	0.1	0.15	0.1	0.1	0.1	0.1
Leaf Width (cm)	0.5	6	3	0.5	0.1	0.5
Rooting Depth (m)	0.1	0.65	0.1	0.32	0.09	0.32
Leaf Water Potential (bar)	-5	-15	-5	-20	-15	-20
Plant Resistance (m^3sec/kg)	2.97×10^6	3.0×10^5	1.2×10^5	2.97×10^6	9.9×10^4	1.2×10^5

Table 3.6: Monthly Measured LAI values for the study sites.

Site	August	September	October
U1 Seismic Line	3.72	3.35	1.51
U1 Undisturbed	4.06	3.33	2.15
L8 Seismic Line	2.6	2.04	1.90
L8 Undisturbed	2.15	2.04	1.60

3.6.4 Soil Parameters

Based on the available soil-moisture, soil-temperature, and textural data, the soil profile in the model was divided into three layers of 15 cm, 15 cm and 30 cm in thickness, the bottom of which corresponds to 15 cm, 30 cm, and 60 cm depth from the ground surface (Figure 3.3). Various textural parameters were measured in the laboratory (Table 3.7) and used as inputs for the model to calculate soil hydraulic properties to calibrate soil water content.

Table 3.7: Soil textural parameters used for the SHAW model simulation. Italicized numbers represent seismic line values whereas numbers in brackets are the adjacent undisturbed area values. The model comprises three layers ending at depths of 15, 30 and 60 cm from the surface.

Soil Parameter	U1			L8		
	Horizon 1 (15 cm)	Horizon 2 (30 cm)	Horizon 3 (60 cm)	Horizon 1 (15 cm)	Horizon 2 (30 cm)	Horizon 3 (60 cm)
Clay (%)	*10* (13.5)	*13.6* (12.3)	*15.9* (18.7)	*17.6* (5.4)	*20.4* (6.3)	*22.4* (7)
Sand (%)	*29.6* (24.1)	*23.2* (24.9)	*14.9* (24.1)	*26.9* (69.8)	*28* (67)	*8.4* (56.8)
Silt (%)	*60.4* (62.4)	*63.2* (62.8)	*69.2* (57.2)	*55.5* (24.8)	*51.6* (26.7)	*69.2* (36.2)
Organic Matter (%)	*1.6* (10.8)	*0.8* (7.5)	*0.8* (1.1)	*12.7* (1.1)	*4.21* (1.9)	*1.9* (0.3)
Bulk Density (g/cm^3)	*0.73* (0.57)	*1.5* (1.2)	*1.5* (1.3)	*1.1* (1.3)	*1.2* (1.34)	*1.36* (1.56)

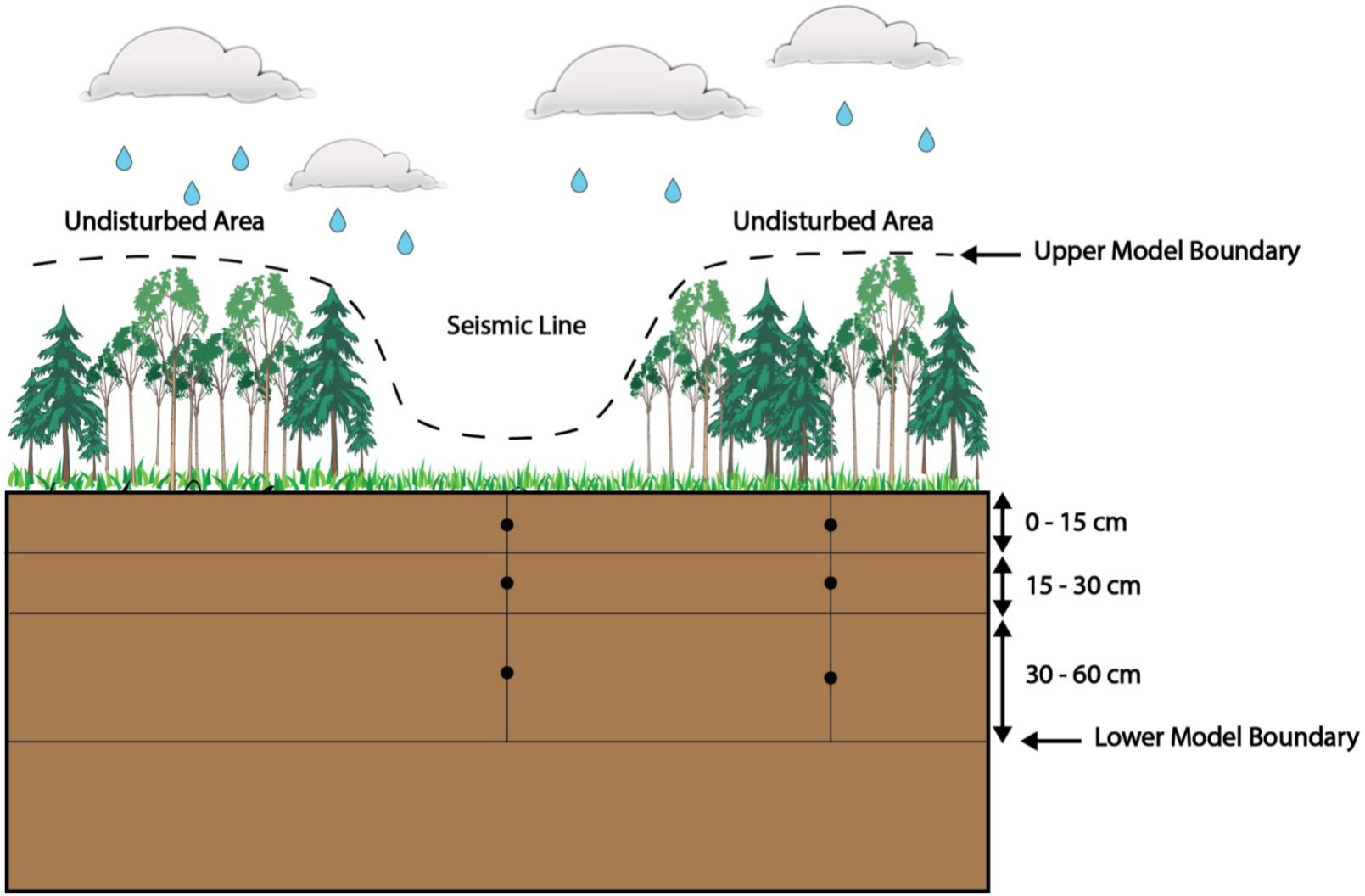

Figure 3.3: Schematics of soil simulation depths and the modified upper boundary used for simulation of the SHAW model in this study.

Soil water content (SWC) influences many output parameters in the SHAW model; thus, its optimization is crucial. However, it is one of the most difficult variables to calibrate (Flerchinger *et al*., 2012). The SHAW model calculates the SWC at each simulation node based on the water-content values defined at the lower boundary. Care must be taken to calibrate soil-hydraulic properties within reasonable limits, otherwise the outputs for various water budget components are affected substantially. Initially, soil hydraulic properties (saturated water content, saturated hydraulic conductivity, air entry potential, and pore size index) were calculated by the model according to the textural data in Table (3.7) and the lower boundary condition (at 60 cm) for water flow was specified by measured soil-water content. However, these hydraulic properties and lower boundary conditions did not yield acceptable ME and RMSD values in any of the soil-moisture calibrations. Consequently, parameter adjustments were performed on the basis that hydraulic properties such as hydraulic conductivity are known to be highly variable, even over a limited extent.. Altering a combination of physical and hydraulic parameters that are inter-related in a logical manner, rather than modifying them one by one, is a more appropriate method to calibrate the model (Hymer *et al.*, 2000). This can be accomplished by (i) an automated multi-objective parameter optimization algorithm, which is beyond the scope of this study and (ii) a trial-and-error approach, which was used in this study (Flerchinger *et al.*, 2012).

By altering the SHAW calculated hydraulic parameters to within 10% of the model calculated value for air entry potential, pore size index, and saturated hydraulic conductivity (Ks), simulated SWC changed on average by 0.005%, 0.003%, and 0.0001% SWC respectively. Initially the Ks values used for all soil depths were the model calculated values (Tables 3.8, 3.9) according to equation 2.6. To improve the SWC simulation, manipulation of the Ks values for

each soil layer was done within a reasonable limit. A reasonable limit was estimated from Ks values calculated using the Kozeny-Carman equation (Table 3.10) for the soil samples from this study (from 0.04 cm/hr to 7.0 cm/hr), and K values estimated using Guelph permeameters in various areas within the upper 60 cm (not necessarily on sites U1 and L8) that ranged between 0.002 cm/hr to 5.1 cm/hr with a median of 0.37 cm/hr. Adjustment of the Ks values for each soil layer within this range did not show a significant impact on the simulated SWC. If adjustment of Ks was done outside of this range, (i.e. < 0.002 cm/hr), this yielded a better SWC simulation, but this was deemed unrealistic based on data available (although some in situ tests using a Guelph permeameter carried out as part of the larger GSC project showed values of the order of 0.002 cm/h).

The adjustment of the air-entry potential and the pore size index resulted in significant differences to the simulated SWC. Similarly, these parameters were adjusted to within reasonable limits. For most soils, air entry potential ranges from – 0.0049 bar for a very coarse soil to – 0.49 bar for a fine soil [pers. commun. With Dr. Flerchinger]. Pore-size index was adjusted to within the model recommended values from 3.0 to 5.5. Soil property values used initially in the model (i.e., calculated by SHAW) and after calibration (outlined in bolded brackets) are presented in Tables 3.8 and 3.9 for sites U1 and L8, respectively. Most values used for the final version of the models are at or close to the values calculated by SHAW, except for Ks, which are systematically lower for both sites (typically by 1.6 times) and for the pore entry, which are higher on average by 0.8 times. Overall, the remaining discrepancies between simulated and measured SWC values can be attributed to a combination of potential errors in the model inputs from literature or field measurements, in measured SWC with the sensors, and/or in the SHAW model dynamics.

Table 3.8: Soil hydraulic properties used for Upland site 1 (U1). Italicized values are values calculated by the model based on textural parameters in Table 3.6. Bolded values in parentheses are adjusted values used to improve model simulations and were used in the final calibrated model.

Soil Hydraulic Properties	Undisturbed Area			Seismic Line		
	Horizon 1 (0 – 15 cm)	Horizon 2 (15 – 30 cm)	Horizon 3 (30 - 60 cm)	Horizon 1 (0 – 15 cm)	Horizon 2 (15 – 30 cm)	Horizon 3 (30 - 60 cm)
Saturated Water Content (m^3/m^3)	*0.46* **(0.44)**	*0.45* **(0.46)**	*0.48* **(0.48)**	*0.44* **(0.38)**	*0.46* **(0.36)**	*0.47* **(0.38)**
Saturated Conductivity (cm/hr)	*2.1* **(1.2)**	*2.3* **(1.5)**	*1.2* **(0.5)**	*2.9* **(2.5)**	*2.1* **(2.6)**	*1.8* **(0.005)**
Air Entry Potential (bars)	*0.05* **(0.065)**	*0.05* **(0.07)**	*0.04* **(0.07)**	*0.06* **(0.06)**	*0.05* **(0.06)**	*0.05* **(0.06)**
Pore Size Index	*3.8* **(4.8)**	*3.7* **(5.5)**	*4.3* **(6.8)**	*3.7* **(5.5)**	*3.8* **(4.8)**	*3.8* **(5.5)**

Table 3.9: Soil hydraulic properties used for Lowland site 8 (L8). Italicized values in red are model calculated values based on textural parameters in Table 3.6. Bolded values in parentheses are adjusted values used to improve model simulations and were used in the final calibrated model.

Soil Hydraulic Properties	Undisturbed Area			Seismic Line		
	Horizon 1 (0 – 15 cm)	Horizon 2 (15 – 30 cm)	Horizon 3 (30 - 60 cm)	Horizon 1 (0 – 15 cm)	Horizon 2 (15 – 30 cm)	Horizon 3 (30 - 60 cm)
Saturated Water Content (m^3/m^3)	0.37 **(0.44)**	*0.39* **(0.41)**	*0.40* **(0.44)**	*0.47* **(0.48)**	*0.48* **(0.44)**	*0.50* **(0.38)**
Saturated Conductivity (cm/hr)	*5.3* **(3.5)**	*4.6* **(3.0)**	*3.9* **(1.0)**	*1.3* **(2.0)**	*0.97* **(0.01)**	*1.1* **(0.005)**
Air Entry Potential (bars)	*0.014* **(0.07)**	*0.015* **(0.07)**	*0.025* **(0.08)**	*0.035* **(0.1)**	*0.03* **(0.1)**	*0.045* **(0.09)**
Pore Size Index	*4.1* **(4.8)**	*4.2* **(4.7)**	*4.0* **(4.8)**	*4.3* **(5.5)**	*4.6* **(5.5)**	*4.3* **(5.5)**

Table 3.10: Kozeny-Carman calculated saturated hydraulic conductivity for study sites U1 and L8 using a porosity (n) of 0.2.

Depth (cm)	U1 Seismic Line	U1 Undisturbed	L8 Seismic Line	L8 Undisturbed
15	0.08	0.06	0.04	7.00
30	0.06	0.06	0.04	0.31
60	0.05	0.04	0.04	0.19

Chapter 4 Results and Discussion

4.1 Soil Solids Physical Properties

4.1.1 Soil Texture and Bulk Density

Soil-samples from all study sites and depths were classified as silt-loam, with the exception of the undisturbed area at site L8 which was a sandy loam (Figure 4.1). Soil samples from site L12 could not be analyzed for grain-size as they were predominantly organic matter (peat) at all sampling depths. For all samples, soil bulk density (BD) was measured at 15 and 30 cm depths in the soil-profile. BD values ranged from a low of 0.11 g/cm^3 (L12 peat) to a high of 1.69 g/cm^3 (U3 mineral soil) with a median of 1.04 g/cm^3 (Figures 4.2A, 4.2B). These BD values are still within the typical BD range for mineral soils of 1.0 to 1.8 g/cm^3 (Brown *et al*. 2021) and thus are not considered to have experienced significant compaction. However, in this study, BD measurements from the upper 15 cm of the soil-profile were higher by 8 to 65% on the seismic lines of all study sites compared to the undisturbed sites (8.1% for U1; 65.2% for U2; and 50.5% for U3; 9.1% for L8 and 16.7% for L12), potentially indicating some compaction (Figure 4.2A). At 30 cm, BD trends are less clear (Figure 4.2B). For instance, on the seismic lines, BD values are greater on sites U1 and U3, similar at U2 and L12, and lower at L8.

Soil compaction following seismic line construction is mostly limited to the upper 20 cm of the soil-profile (Filicetti and Nielsen, 2022), which was generally observed here. Filicetti and Nielsen 2022 measured BD in the top 20 cm of the soil-profile for mesic upland forest soils near Fort McMurray, Alberta and found significantly ($p < 0.001$) higher BD values on seismic lines (0.67 g/cm^3 ($n = 146$)) compared to their respective adjacent undisturbed areas (0.50 g/cm^3 ($n = 146$)). The low mean BD in their study was attributed to the high organic matter content (Ranging from 0 – 50% with an average of 15%) for the boreal forest soils in their study area (Filicetti and Nielsen, 2022), which is similar to the organic matter content in the soils of the undisturbed areas of this study. Bulk density

measurements from peatland site L12 are similar to those obtained by Waddington and Roulet 2000 (between 0.05 and 0.15 g/cm^3) and to a study by Strack *et al.* (2018) on a boreal peatland impacted by winter road construction (0.04 to 0.16 g/cm^3). The low BD from samples from site L12 is likely due to the large SOM accumulation due to the prolonged saturated conditions which will act to inhibit mineralization and SOM decomposition (Quideau *et al.,* 2021). The variations in bulk density among sites can be attributed to many factors: (i) recent re-use of seismic lines (e.g. recreational and/or animal use) (ii) ecosite, sites with less soil organic matter (SOM) accumulation experience more compaction, (iii) degree of vegetation cover and (iv) soil-texture type (Dabros *et al.,* 2018; Davidson *et al.,* 2020; Filicetti and Nielsen, 2022).

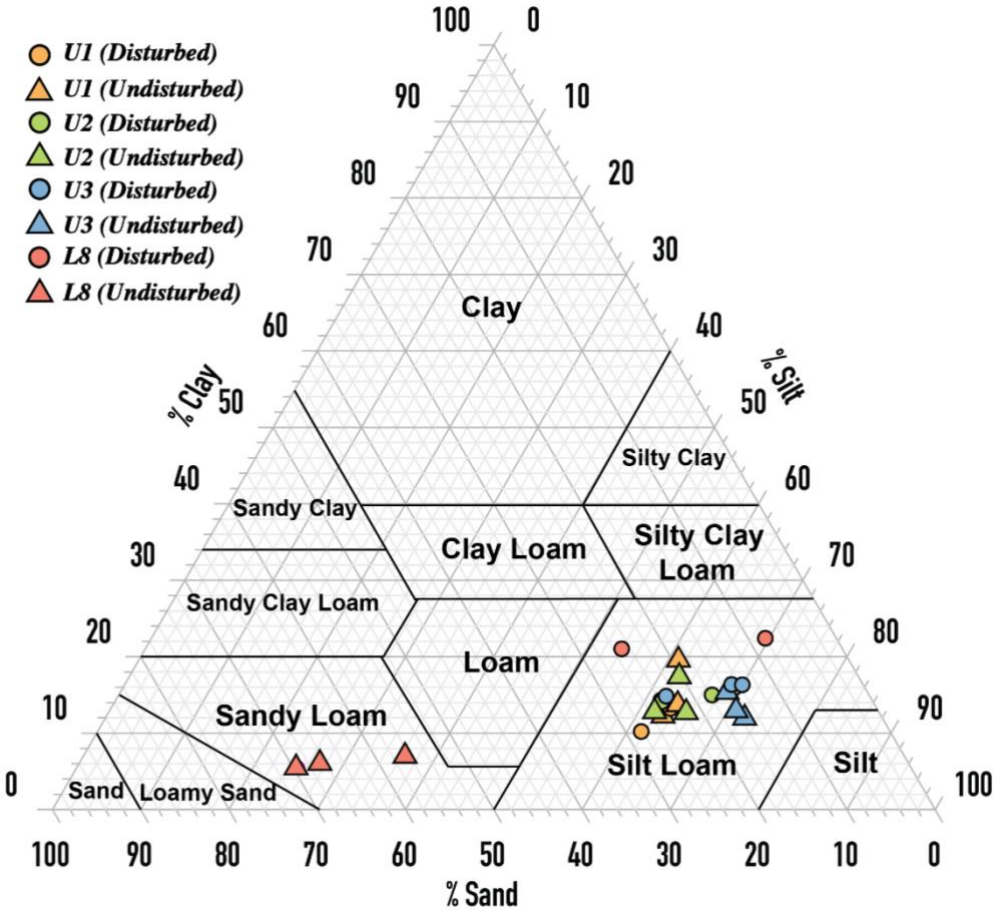

Figure 4.1: Measured soil-textures for study sites in the study area.

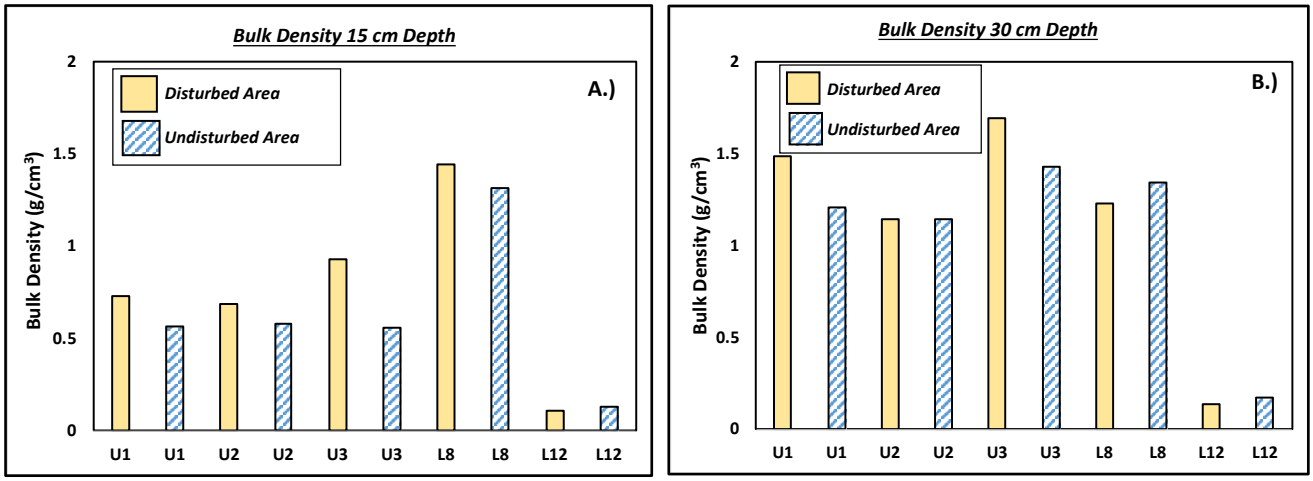

Figure 4.2: Measured soil bulk density values for the study sites at A) 15 cm depth and B) 30 cm depth.

4.2 Soil Solids Chemistry

In the following presentation of results, sites will again be separated according to upland and peatland (lowland) results. Since all of the upland sites generally showed similar results, only one of them will be presented in detail as it has a more complete dataset for all depths (again upland site 2, U2). The remaining results for upland sites U1 and U3 are available in Appendix E.

4.2.1 Soil Organic Matter Content and Cation Exchange Capacity

At U2, soil organic matter (SOM) content from the undisturbed area at 15 cm depth in the soil profile was 8% greater compared to the adjacent seismic line (Figure 4.3A). At 30 cm depth, the undisturbed area showed slightly more (0.8%) SOM compared to the seismic line, whilst at 60 cm depth, the seismic line showed 1.1% more SOM compared to the undisturbed area, both of which are unlikely to be statistically significant and are within the uncertainty of the analytical method. Conversely, for sites L8 and L12, SOM content from the seismic line at 15 and 30 cm depth were 1.6 (within analytical uncertainty) and 11.6% greater, respectively, compared to their respective undisturbed areas.

Similarly, the seismic line SOM content at 60 cm for L8 was 1.6% greater than the undisturbed area, whereas the undisturbed area on L12 had 60% more SOM than the seismic line. At U2, the cation exchange capacity (CEC) was greater on the undisturbed area by 7.0, 9.1, and 1.9 cmol (+) / kg for 15, 30, and 60 cm respectively (Figure 4.3B). Similarly, at L12, CEC was greater on the undisturbed area by 19.9, 5.4, and 4.6 cmol (+) / kg for 15, 30, and 60 cm respectively. Conversely, the seismic line on L8 showed consistently greater CEC values compared to the undisturbed area by 13.1, 20.1, and 21.43 cmol (+) / kg for 15, 30, and 60 cm respectively. XRD identified that most minerals in the soil samples were silicates and that only one site (U2) contains the carbonate mineral magnesite in detectable amounts (Table 4.1). Many clay mineral types were identified at sites U2 and L8, whereas at L12 only montmorillonite was identified.

4.2.2 pH and Major Ions

The pH of all soil samples obtained from the study area ranged from 3.4 to 6.2 with a mean of 4.9 (Figure 4.3D). At U2, the pH differences between seismic line and the adjacent undisturbed area were subtle. For instance, at 15 and 30 cm, the undisturbed area showed higher pH values by 0.1 and 0.03 pH units respectively, compared to the seismic line, whilst at 60 cm the seismic line had a higher pH by 0.08 units compared to the undisturbed area. At L8, the pH on the seismic line was significantly greater than the undisturbed area by 0.77, 0.65, and 1.05 for 15, 30, and 60 cm, respectively. Lastly, at L12, samples obtained from 15 and 30 cm depth in the soil profile of the undisturbed area showed slightly higher pH values (+0.28 and +0.22, respectively) compared to the seismic line, whilst at 60 cm, the seismic line had a higher pH (+0.12) compared to the undisturbed area.

The major water-soluble base cations (Na^+, Mg^{2+}, Ca^{2+}, K^+) across all of the soil samples were generally $Ca^{2+} > Mg^{2+} > K^+ > Na^+$ (Figure 4.4). A similar trend in major water-soluble base cations from soil samples in the study region was observed by Knapik and Lindsay (1983). At U2, the undisturbed area consistently had higher concentrations of base cations compared to the seismic line, particularly at 15 cm (Figure 4.4A). Similarly, the undisturbed area at L12 (Figure 4.4C) consistently showed higher concentrations of base cations compared to the seismic line and overall higher concentrations of base cations. Conversely, the seismic line at L8 showed higher concentrations of base cations compared to the undisturbed area (Figure 4.4B).

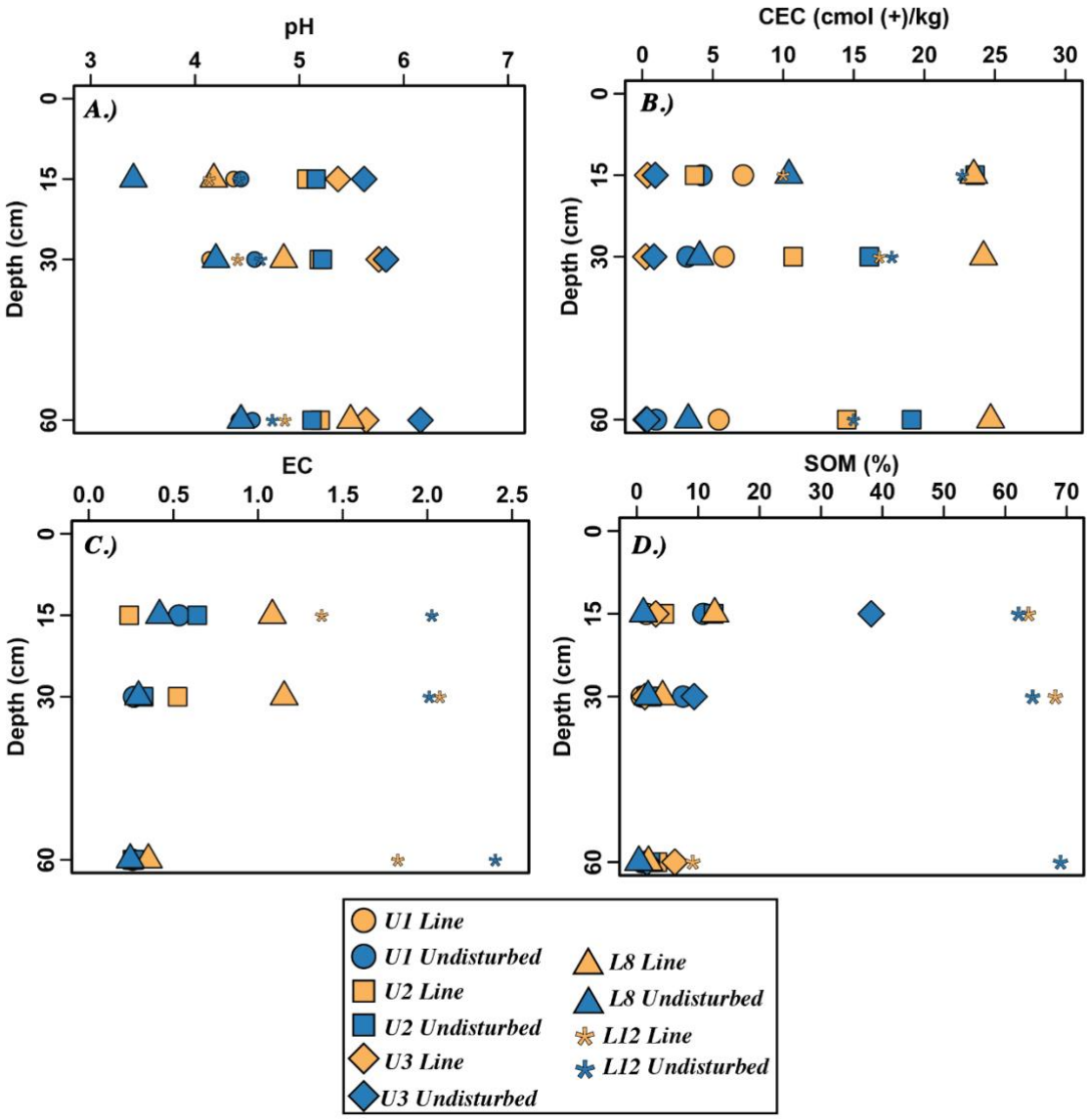

Figure 4.3: Plots of A) pH, B) Cation exchange capacity (CEC), C) Electrical Conductivity (EC) and D) Soil organic matter (SOM) obtained from solids in the soil-profile.

Table 4.1: Mineral phases identified from soil-solid samples obtained at each study site. A corresponds to the seismic line sites whereas B indicates the adjacent undisturbed areas.

Phase Identified	XRD Formula	U2A	U2B	L8A	L8B	L12A	L12B
Quartz	SiO2	✓	✓	✓	✓	✓	✓
Muscovite	(K0.7Na0.2Ca0.011)(Al0.93Fe0.016Mg0.011)2(Si0.78Al0.22Ti0.01)4O10(OH)2	✓	✓	✓	✓	✓	✓
Albite	Na0.84Ca0.16Al1.16Si2.84O8	✓	✓	✓	✓	✓	✓
Microcline	K0.86Na0.14AlSi3O8			✓	✓		
Rutile	TiO2					✓	
Orthoclase	K4Al4Si12O32	✓		✓	✓		
Pyrite	FeS2	✓	✓				
Microcline	K0.86Na0.14AlSi3O8		✓				
Anorthite	Na0.48Ca0.52(Al1.52Si2.48O8)					✓	✓
Glauconite	(K0.76Ca0.04Na0.01)(Al0.53Mg0.44Fe1.07)((Si3.58Al0.42)O10(OH)2)					✓	✓
Nacrite	Al2(Si2O5)(OH)4			✓	✓		
Kaolinite	*Al2(Si2O5)(OH)4*	✓	✓	✓	✓		
Clinochlore	*Al2Mg5(Si3O10)(OH)8*	✓	✓	✓	✓		
Montmorillonite	*Ca0.5(Al2Si4O11(OH))*	✓			✓	✓	
Vermicullite	*Na0.93Mg2.8Fe0.07Al1.2Si2.9O10(OH)2(H2O)3*	✓					
Vermicullite - 2M	*Mg3(Si4O10)(OH)2*			✓			
Saponite	*(Mg2Al)(Si3Al)O10(OH)2*4H2O*			✓			
Nontronite	*Ca0.1Fe2(Si,Al)4O10(OH)2*4H2O*		✓	✓			
Stilbite	*Na1.76Ca4(Al10Si25O72)(H2O)29.4*		✓				
Magnesite	*MgCO3*		✓				

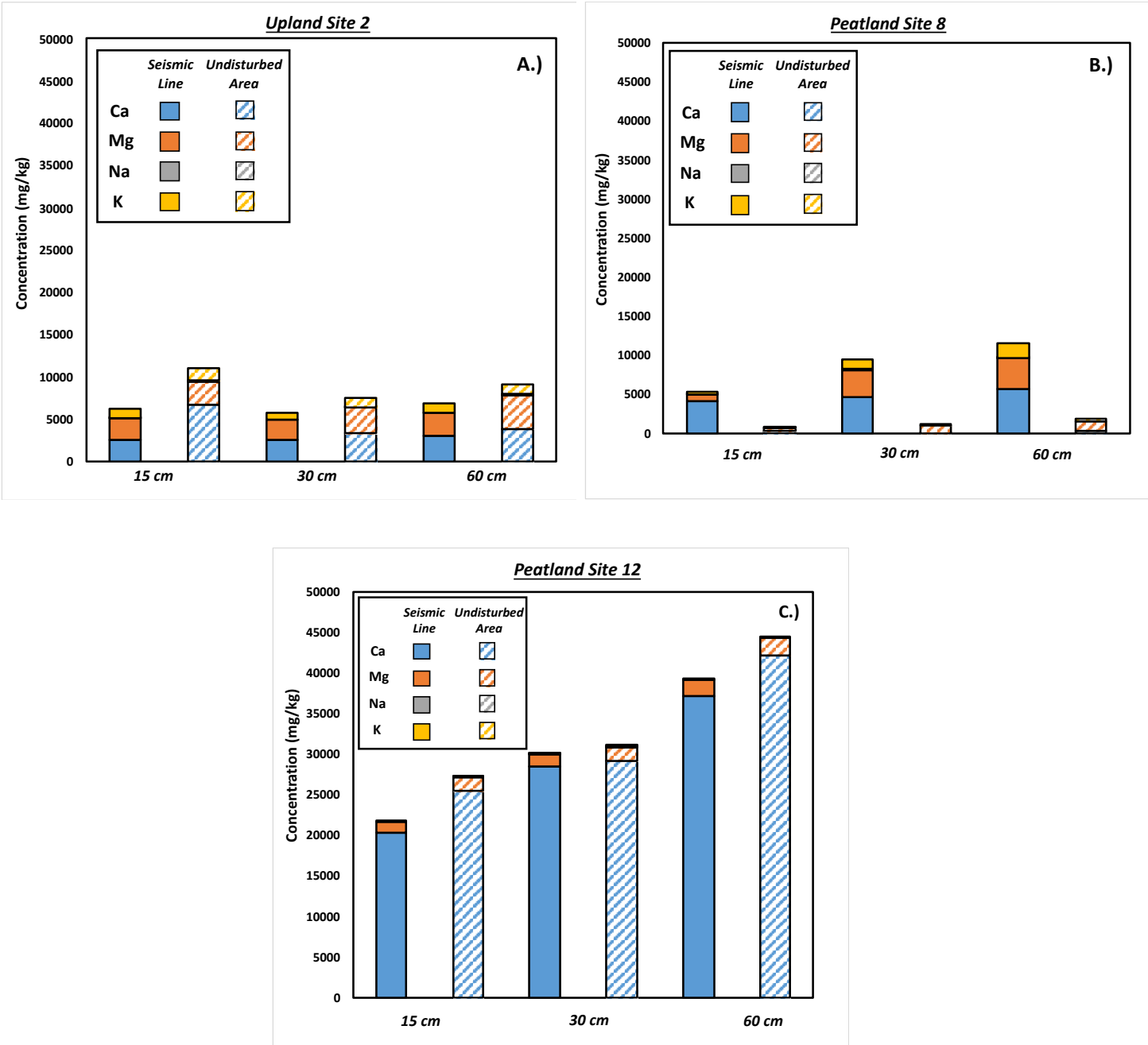

Figure 4.4: Major water-soluble ion concentrations for the soil solids obtained on a seismic line and the adjacent undisturbed area over various depths for A) Upland Site 1 (U1), B) Lowland Site 8 (L8), and C) Lowland Site 12 (L12).

Synthesis

Although chemical weathering of soil minerals can buffer against changes in soil pH, these reactions are kinetically slow and of lower importance when compared to the exchange processes in soil (Essington, 2015). Acidic soils (pH < 6.5), a category into which the soils in this study fall, can buffer against pH changes by weathering of carbonate minerals and/or exchangeable ions (e.g. Na^+, Ca^{2+}, Mg^{2+}, K^+) adsorbed onto SOM and the surfaces of soil colloids (Kumaragamage *et al.,* 2021). Although there may be input of calcareous minerals from weathering of limestone rocks of the foothills and/or from the Paskapoo Formation that contain calcareous sediments (Grasby *et al.,* 2008), limited carbonate minerals were detected by XRD in the soils of this study. Thus, soil pH is likely buffered by exchange reactions making the SOM and clay content in the soil important variables to consider when comparing between the study sites.

SOM and clay minerals (2:1 type clays) (both of which are present in the soils of this study), are key contributors to the CEC of a soil (Kumaragamage *et al.,* 2021) with the former largely being produced from belowground biomass and litterfall input (Quideau *et al.,* 2021). Because different vegetation communities are present on seismic lines compared to their adjacent undisturbed areas, the root biomass and annual litter fall inputs onto the soils are different (Dabros *et al.,* 2018). For instance, a study by Lankau *et al.* (2013) noted an overall reduction in annual litterfall inputs onto soils disturbed by seismic lines, which may explain the lower SOM content on the shallow (15 cm) soils of seismic lines in this study. Additionally, following disturbance many early-successional plant species produce litter that decomposes more rapidly than moss and coniferous litter produced in late-successional forests (Turetsky *et al.,* 2008; Moore *et al.,* 2015).

The SOM content is generally < 20% for both the seismic lines and undisturbed areas for all sites apart from L12 (a lowland/peatland site with > 40 cm of peat accumulation), which had a SOM content >60% (Figure 4.3D). The greater amount of SOM in boreal

peatlands compared to upland forested sites occurs because the rate of net primary production of vegetation (i.e. *Sphagnum* species) is greater than the rate of litter decomposition by microbes in peatlands. Additionally, boreal peatlands also have a high-water table, impeding the decomposition (Moore *et al.,* 2015). This was confirmed by the high moisture content of the soils at L12 (see section 4.5.6). Conversely, in well-drained upland forested sites the difference between the rates of net primary production by vegetation and decomposition by microbes is smaller, leading to less SOM accumulation compared to peatlands (Moore *et al.,* 2015).

For sites U1, U2, U3, and L8, CEC was positively correlated with SOM ($R^2 = 0.21$), silt content ($R^2 = 0.10$), clay content ($R^2 = 0.27$), and pH ($R^2 = 0.34$) and negatively correlated with sand content ($R^2 = 0.16$). These general correlations have been observed in other studies (Fang *et al.* 2017). However, it is difficult to decipher the relative contribution of clay minerals and SOM to the soil CEC in this study, and a further characterization of the SOM type and percentage of individual clay minerals present is needed.

CEC has been identified in a previous study as playing a crucial role in buffering against soil pH changes for acidic soils (Fang *et al*., 2017). Addition of acidity (i.e. precipitation, atmospheric deposition, organic matter decomposition) to an already acidic soil causes H^+ to adsorb onto the exchangeable sites of soil colloids resulting in the dissociation of base cations into soil-water which can then subsequently be leached by infiltrating meteoric water resulting in an overall decreases soil CEC (Watmough and Dillon, 2003; Lieb *et al.,* 2011; Fang *et al.,* 2017). The lower CEC of the soils on the seismic lines identified in this study means these areas are more susceptible to acidification and subsequent leaching of base cations. This is supported by the following: (i) the positive correlation between soil pH and CEC indicates that more acidic soils (i.e. the seismic line soils in this study) have a lower CEC, (ii) the lower CEC results in a poor buffering capacity of the soils on seismic lines, which may enable leaching of base cations from the exchangeable sites on soil colloids

releasing the base cations into soil solution, (iii) base cation leaching occurring on the seismic lines might be supported by the observation that the soil water from seismic lines had higher concentrations of ions (e.g. Ca^{2+}, Mg^{2+}) compared to their respective adjacent undisturbed areas and concentrations generally increased with depth (see section 4.3.4).

Altered SOM inputs may also affect the presence of microbial communities and microbial activities possibly increasing mineralization or decomposition (Scheffer *et al.,* 2001; Allison and Treseder, 2011). For instance, microbial respiration was observed to increase in an ancient peatland following an increase of 1°C in soil temperature particularly when graminoids and shrubs were present (Walker *et al.,* 2016), which are usually the dominant vegetation type on seismic lines compared to their adjacent undisturbed areas (Dabros *et al*., 2018) and were the observed vegetation communities on seismic lines in this study. In this study, soil temperature measurements during the summer from the 15 cm depth on the seismic lines were always significantly higher by 0.8 to 2.6°C compared to the adjacent undisturbed areas. Additionally, the SWC content from L8 was significantly higher by 5.0% compared to the adjacent undisturbed area (see section 4.6), These two factors potentially contribute to enhanced mineralization and organic matter decomposition.

Additionally, the lower amount of SOM on seismic lines may result in its destabilization by: (i) reduced complexation of SOM with base cations due to the decreased dissociation of SOM functional groups (e.g. carboxyl) resulting in less negative charge present (Essington, 2015) and/or (ii) reduced cation bridging (e.g. Ca, Al, Fe) between clay minerals and SOM making SOM more susceptible to mineralization (Lützow *et al.,* 2006; Quideau *et al.,* 2021).

4.3 Soil Solution Chemistry

4.3.1 Soil Water General Chemistry

The solute concentrations of all soil profiles generally decrease in the following order: HCO_3^- > Ca^{2+} > DOC > DSi > Mg^{2+} > Cl^- > Na^+ > K^+ ≈ Fe ≈ Al > $SO4^{2-}$ > $NO3^-$. The mean

charge balance error (CBE) was very negative: 41.7 +/- 14.8%, 40.6 +/- 17.8%, and 42.9 +/- 14.2% for soil-water samples obtained from 30, 60, and 120 cm depth respectively. This has been observed in other studies of soil waters and has been attributed to higher dissolved organic carbon (DOC) concentrations which constitute weak organic acids that account for the deficit (Arthur and Fahey, 1993). Following an empirical correction to account for the negative charge on DOC outlined in (Oliver *et al.,* 1983), CBE were improved to 23.3 +/- 17.5%, 28.3 +/- 17.5%, and 37.1 +/- 17.3% for soil-water samples obtained from 30, 60, and 120 cm depth respectively. A better CBE may be obtained via determination of the charge on the organic acids in the soil water via: (i) a conductivity detection analysis in conjunction with a Dionex QD Charge Detector Cell (QDC) analysis and/or (ii) using an FT-ICR-MS to profile the organic compounds. However, these approaches are beyond the scope of this project.

Soil-water pH increased with depth at all sites (Figure 4.5 A1 to A3). Soil water pH at sites U2 and L8 was significantly greater ($p < 0.05$ and $p < 0.001$ respectively) on the seismic line at 30 cm depth, and varied between sites for 60 and 120 cm. No significant ($p < 0.05$) differences in soil-water pH were observed at site L12 among the seismic line and the adjacent undisturbed area (Figure 4.5 A3). DOC concentrations were significantly greater on the seismic line at shallow (30 cm) depths for all sites (U2 ($p < 0.05$); L8 ($p < 0.01$); L12 ($p < 0.001$)) (Figure 4.6 F1 to F3). Ca and DOC concentrations followed a similar trend by increasing with depth for all sites (Figure 4.5B, 4.6C). For site U2 and L8, at 30 and 120 cm, Ca and DIC concentrations were significantly greater on the seismic line compared to the undisturbed area; whilst at 60 cm they were only greater on the seismic line for site L8 as U2 and L12 showed no significant differences. Mg and Si concentrations between on seismic line and the undisturbed areas at site L12 were similar at 30 and 60 cm, whereas at 120 cm the ion concentrations were significantly greater on the seismic line (Figure 4.6). For site L8, Mg and Si concentrations were consistently greater on the seismic line at all depths; whilst for site U2 they were both significantly greater only at 30 cm depth.

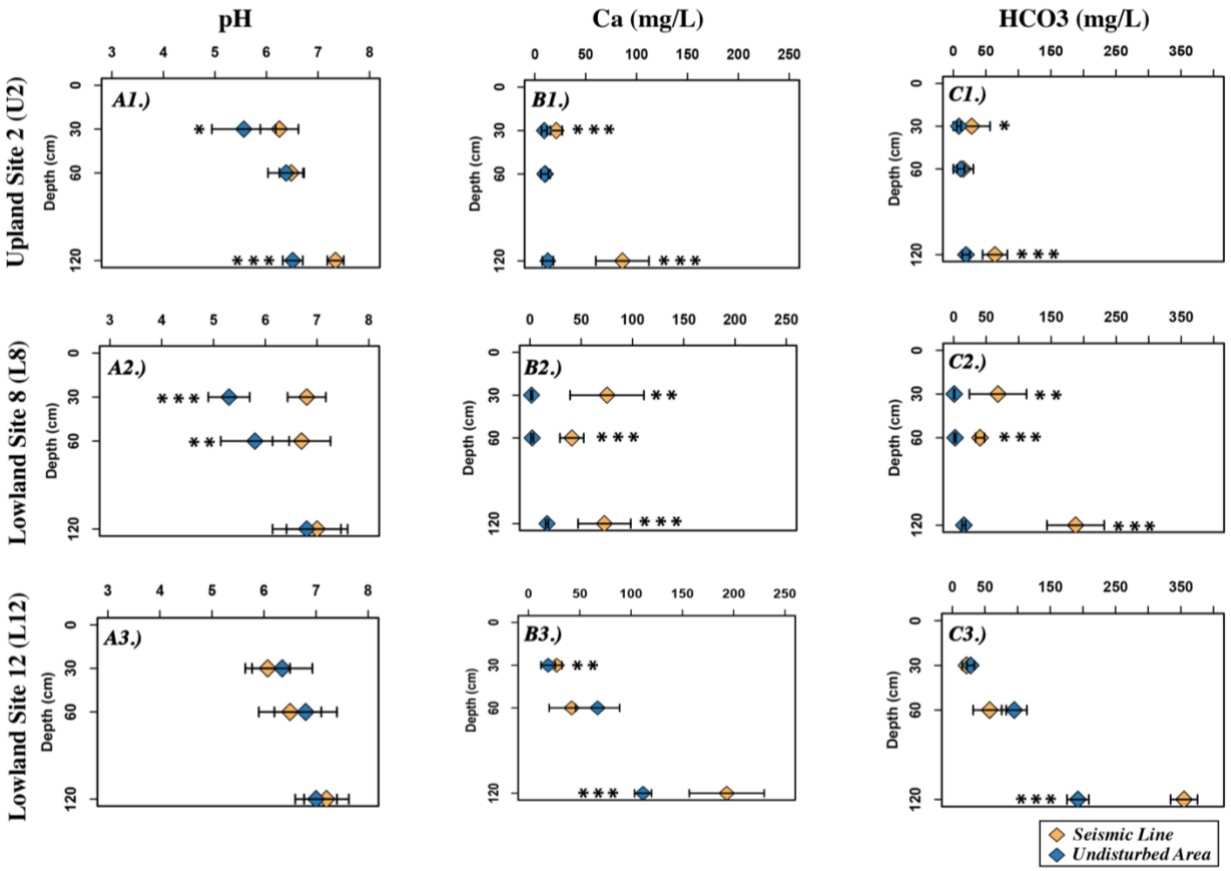

Figure 4.5: Mean values (+/- standard deviation) of soil-water pH and concentrations of Ca and HCO3 for the soil-profiles at sites U2, L8, and L12 (the yellow and blue symbols correspond to the seismic line and undisturbed area samples respectively). The Mann-Whitney U test was applied for differences between the seismic line and undisturbed area at each depth with levels of significance: *, **, *** corresponding to $p < 0.05$, $p < 0.01$, and $p < 0.001$ respectively.

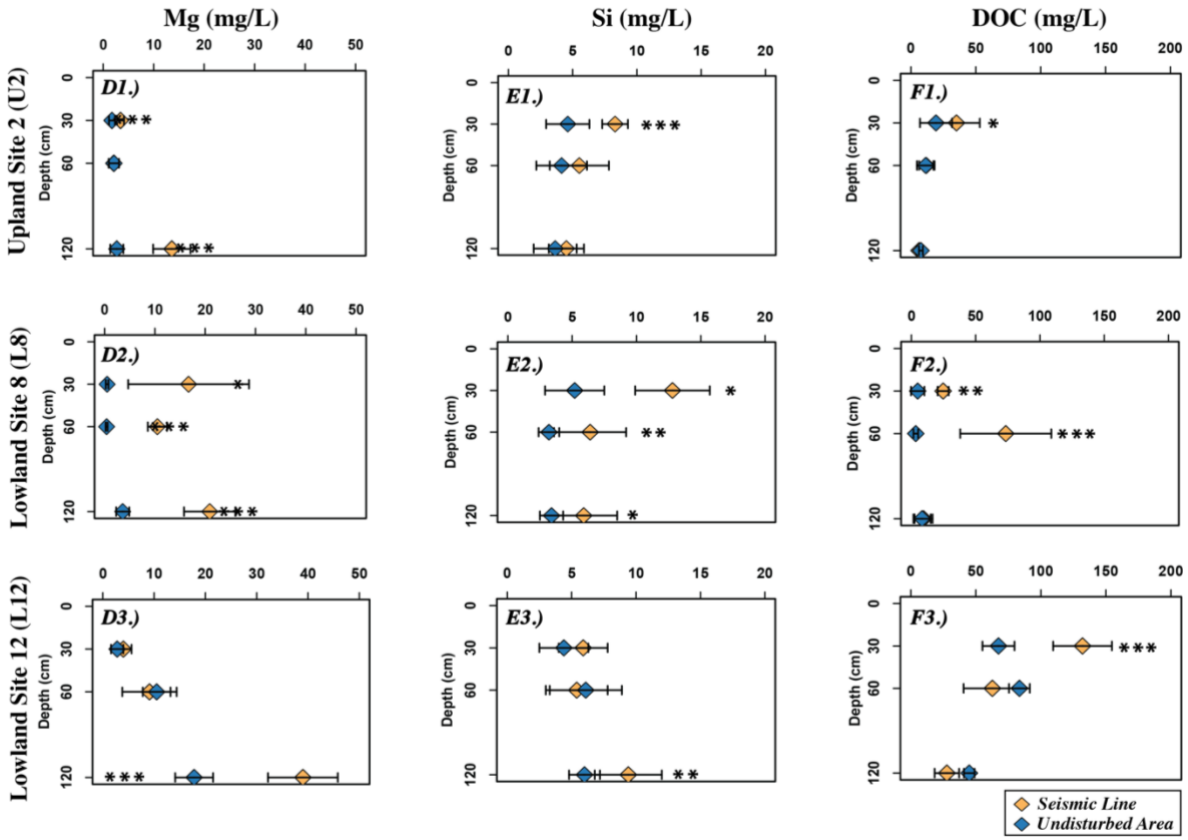

Figure 4.6: Mean values (+/- standard deviation) of soil-water Mg, Si, and DOC concentrations for the soil-profiles at sites U2, L8, and L12 (the yellow and blue symbols correspond to the seismic line and undisturbed area samples respectively). The Mann-Whitney U test was applied for differences between the seismic line and undisturbed area at each depth with levels of significance: *, **, *** corresponding to $p < 0.05$, $p < 0.01$, and $p < 0.001$ respectively.

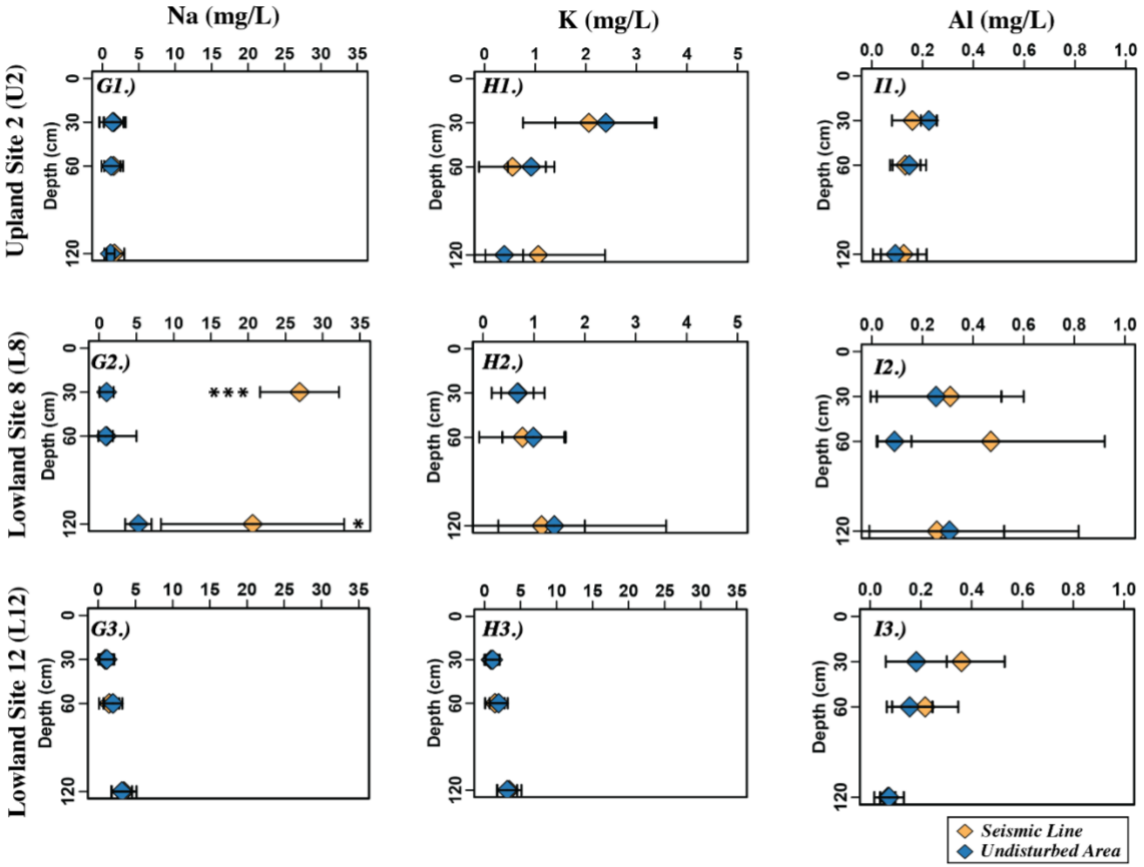

Figure 4.7: Mean values (+/- standard deviation) of soil water Na, K, and Al concentrations for the soil-profiles at sites U2, L8, and L12 (the yellow and blue symbols correspond to the seismic line and undisturbed area samples respectively). The Mann-Whitney U test was applied for differences between the seismic line and undisturbed area at each depth with levels of significance: *, **, *** corresponding to $p < 0.05$, $p < 0.01$, and $p < 0.001$ respectively

4.3.2 Precipitation $\delta^{18}O$ and $\delta^{2}H$ Isotope Data

A Wilcoxon rank sum test was performed on $\delta^{18}O$ and $\delta^{2}H$ values obtained from the brass and plastic rainwater collectors. The results showed that seasonal medians were not statistically different at the 0.05 α-level and were subsequently analyzed together yielding a total of 39 meteoric water samples collected over 18-months. Considering this, precipitation water isotopes from 2021 to 2022 ranged from a low of -31.6 ‰ for $\delta^{18}O$ (-240.7 for $\delta^{2}H$) in the winter to a high of -13.2 ‰ (-105.9 ‰ for $\delta^{2}H$) in the summer. Seasonally averaged $\delta^{18}O$ and $\delta^{2}H$ values reflect that the most depleted values were observed in the winter with progressively enriched values in the spring, fall, and summer, respectively (Figure 4.8). The largest seasonal range in $\delta^{18}O$ and $\delta^{2}H$ values was found to occur in the fall, while the smallest range occurred in the summer. $\delta^{18}O$ and $\delta^{2}H$ distributions for the winter and summer were relatively symmetrical and considered normally distributed at the 0.05 α-level using the Shapiro-Wilk test. The Wilcoxon rank sum test showed that seasonal medians were statistically different between all seasons apart from fall and spring ($p = 0.10$ and $p = 0.11$ for fall and spring $\delta^{18}O$ and $\delta^{2}H$ values, respectively).

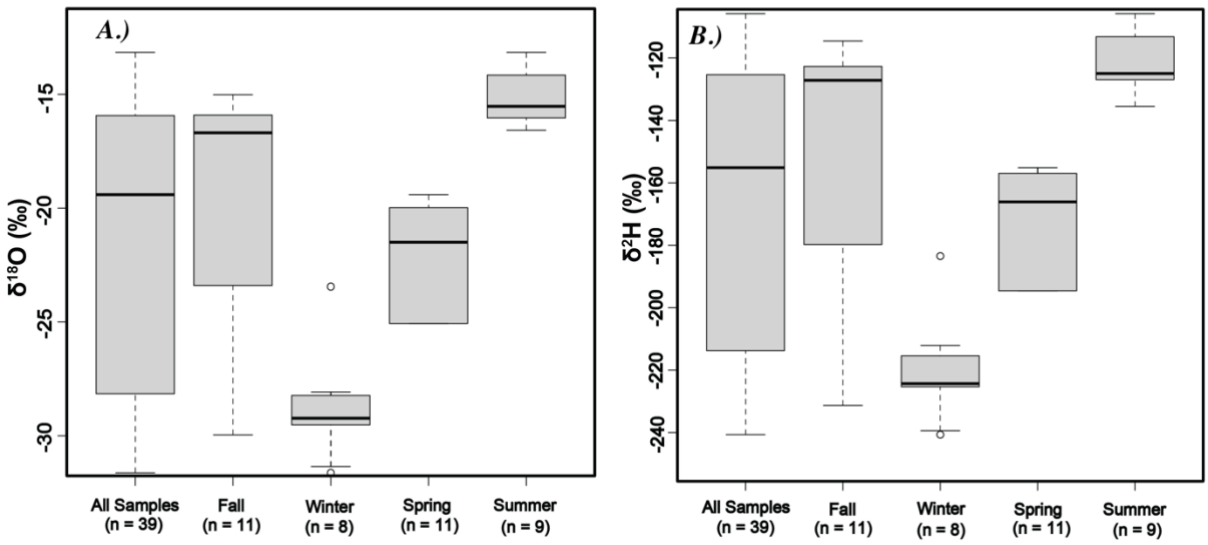

Figure 4.8: Boxplots for the seasonal distribution of $\delta^{18}O$ and $\delta^{2}H$ in precipitation. All samples were collected between July 2021 to December 2022. Seasons were divided accordingly: Fall (September to November), Winter (December to February), Spring (March to May), and Summer (June to August).

The local meteoric water line using the 2021 – 2022 data (n = 39 and $R^2 = 0.99$) (Figure 4.9) is described by Equation 4.1.

$$\delta^{2}H\ (‰) = 7.44\ \delta^{18}O\ (‰) - 6.80 \quad \textbf{(Eqn 4.1)}$$

Summer long-term (21-year) temperature and precipitation values are 13.8°C and 257.7 mm, respectively using the Fox Creek Junction weather station data. Data collected during the first summer (2021) indicates precipitation (255.5 mm) was near the long-term norm whereas the temperature was higher (16.9°C) indicating a slightly drier summer. The second summer (2022) precipitation (308.7 mm) was above the long-term norm and the average temperature was 15.6°C indicating a warmer and wetter than normal summer (these trends are also supported by the soil-moisture data). Figure 4.9 presents these values using different colours according to seasons. For

comparison, it also shows the Global meteoric water line (Craig, 1961) and the Edmonton LMWL (Maule *et al*., 1994).

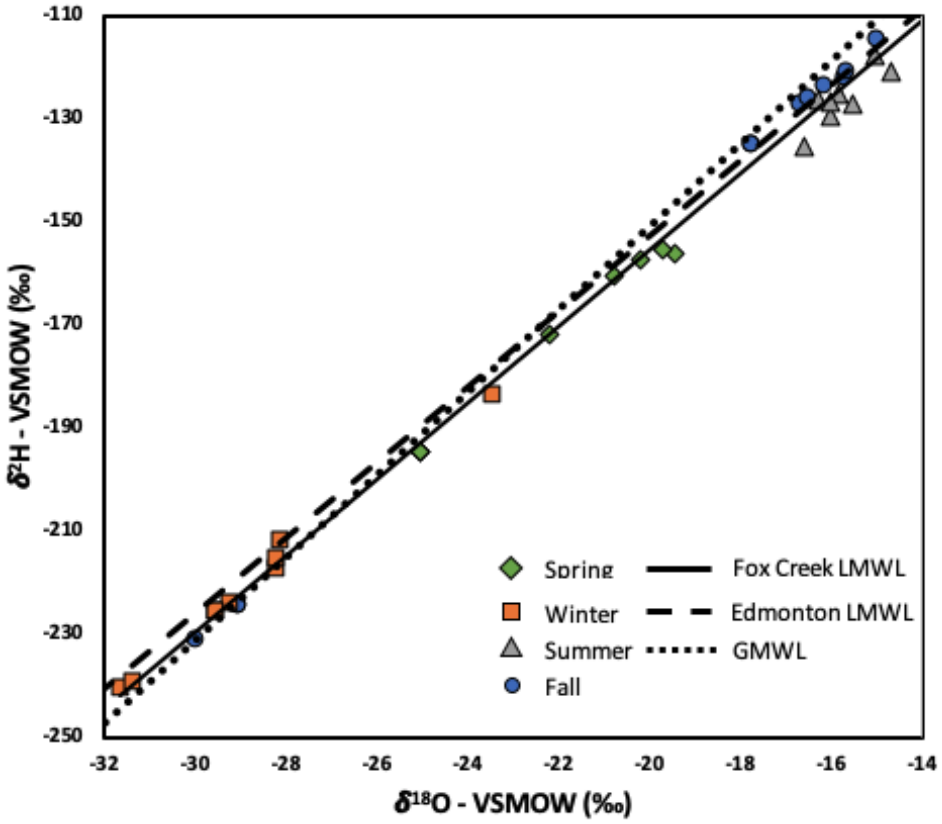

Figure 4.9: Oxygen-18 and deuterium values of Fox Creek meteoric waters from 2021 -2022. For reference, shown are the GMWL after Craig (1961) and Edmonton the LMWL after Maule *et al.* (1994).

4.3.3 Soil Water $\delta^{18}O$ and $\delta^{2}H$ Isotope Data

Cumulative $\delta^{18}O$ and $\delta^{2}H$ soil water values separated by depth for all samples reveal that the shallow soil water depths (30 and 60 cm) have similar median $\delta^{18}O$ and $\delta^{2}H$ values and spread (Figure 4.10A, 4.10B). However, the deeper (120 cm) samples have a median isotopic signature of -18.8 (+/- 0.2) ‰ and -147.5 (+/- 1.7) ‰ for $\delta^{18}O$ and $\delta^{2}H$ respectively. These values are within analytical error for $\delta^{18}O$ and near analytical error for $\delta^{2}H$. Overall, soil water $\delta^{18}O$ and $\delta^{2}H$ values generally decreased in standard deviation and became isotopically enriched

with depth (Figure 4.10A, 4.10B). The average $\delta^{18}O$ and $\delta^{2}H$ values from limited (n = 4) shallow (32 to 35 m well depths) groundwater samples from the Paskapoo aquifer obtained from nearby monitoring wells were -19.0 (+/- 0.4) ‰ and -150.6 (+/- 3.4) ‰. All soil water samples plotted on or near the LMWL (Figure 4.7C) indicating minimal evaporation and this was further supported by lc-excess values which spanned from -3.3 ‰ to 2.6 ‰ with a median of – 0.5 ‰ across 154 soil water samples (Figure 4.10D).

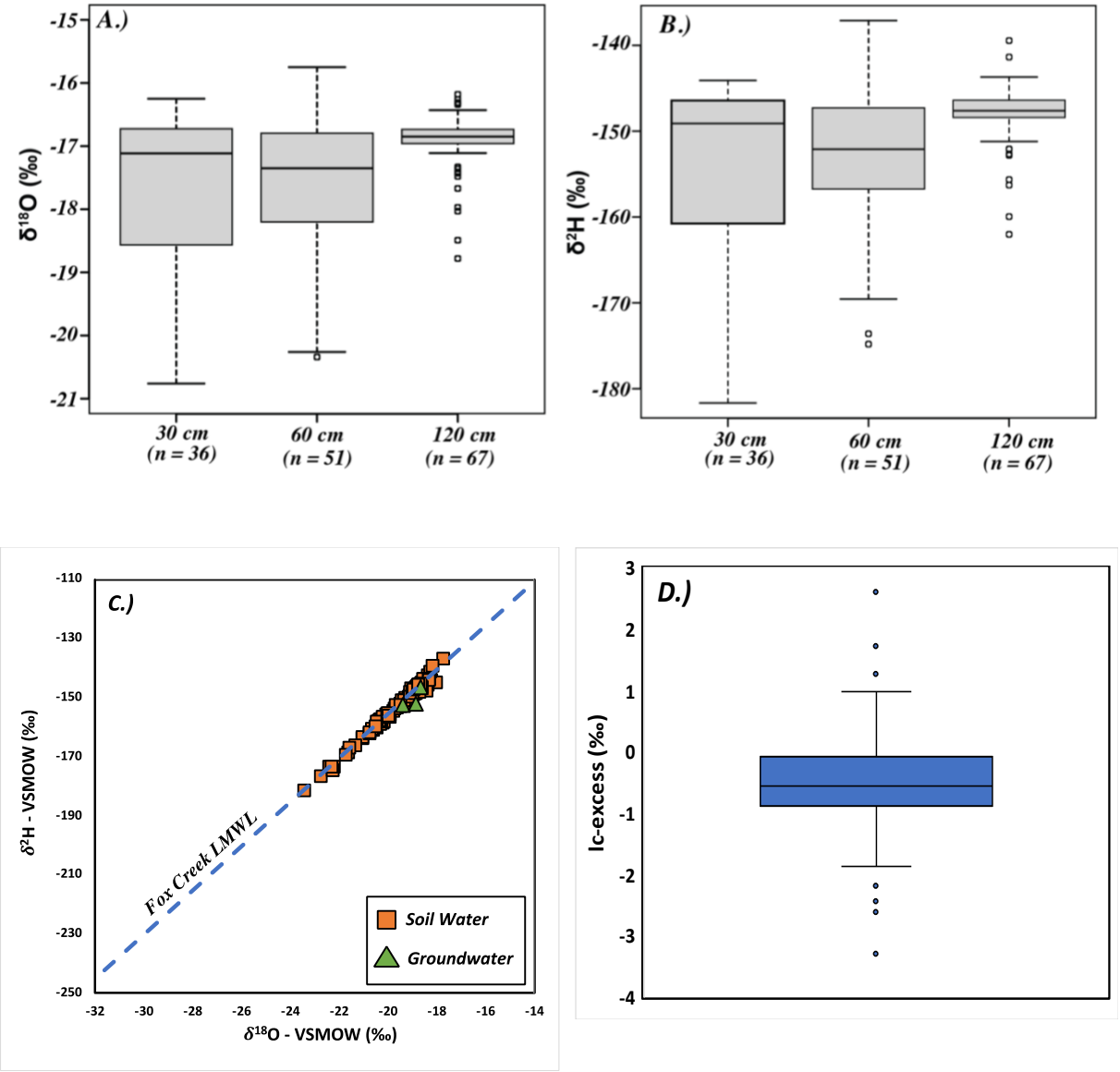

Figure 4.10: Graphs presenting isotope spread as a function of depth for all soil water samples A.) Boxplots for $\delta^{18}O$; B.) Boxplots for $\delta^{2}H$; C.) Dual-isotope plot showing the Fox Creek LMWL, all soil water samples from this study and values from shallow monitoring wells completed in the Paskapoo Fm. from the larger GSC project; D.) Boxplot of line conditioned (LC) – excess values for all soil water samples.

4.3.4 Variations in Soil Water $\delta^{18}O$ and $\delta^{2}H$ Isotopes with Depth

Upland Site (U2)

Seismic Line

The seismic line at U2 had a less complete sampling record than the adjacent undisturbed area due to sampling issues with the suction lysimeters. The shallow (30 cm) soil water from the seismic line reveals the most depleted $\delta^{18}O$ values (-21.0 ‰) in May with an evolution to more enriched values following summer sampling, however, the spread (-21.1 to -20.3 ‰) is within analytical uncertainty (0.8 ‰) (Figure 4.11A). Soil water samples from 60 cm deep indicate an evolution to more depleted values from May (-18.0 ‰) to June (-18.9 ‰) possibly indicating a slow percolation rate from the overlying shallow samples (thus involving evaporation) or simply be an artifact as the two values are near analytical uncertainty. A total of seven samples from the 120 cm sampling depth area have a consistent signature (-18.8 to -18.3 ‰), within analytical uncertainty and are similar to the shallow groundwater samples taken from the monitoring wells within the watershed (Figure 4.11A).

Undisturbed Area

The undisturbed area 30 cm soil water samples showed a larger spread (-21.7 to -19.3 ‰) compared to the seismic line (Figure 4.11A). Successive sampling from June – October at 30 cm revealed a shift to more enriched soil water isotope values. Samples at 60 cm indicate a consistent isotopic signature (-20.4 to -20.1 ‰) within analytical uncertainty. Samples from the 120 cm sampling depth have a consistent signature (-19.1 to -18.6 ‰), within analytical uncertainty and are again similar to shallow groundwater samples taken from the monitoring wells within the watershed.

Lowland Site (L8)

Seismic Line

On the seismic line at L8, the shallow (30 cm) soil water shows a similar seasonal trend as U2 where the most depleted $\delta^{18}O$ value (-19.8 ‰) occurs in May and subsequent monthly samples show an evolution to more enriched values due to mixing with summer precipitation (Figure 4.11B). The overall spread of $\delta^{18}O$ values at 30 cm was -19.8 to -18.5 ‰. Soil water at 60 cm from L8 showed a similar pattern to the 60 cm soil water samples from the seismic line at U2 where the most depleted values occur late in the growing-season (August-September) and the most enriched values occur following spring-melt, possibly reflecting a similar lag in infiltration.

Undisturbed Area

On the undisturbed area of L8, the shallow samples (30 cm) have the largest spread (-23.4 to -20.2 ‰) among all sites and show a strong seasonal response in soil water $\delta^{18}O$ values (Figure 4.11B), which can likely be attributed to its sandier texture (Figure 4.1) resulting in a faster turnover of soil water. Similar to previous sites, at 30 cm the most depleted $\delta^{18}O$ values (-23.4 ‰) occur in May with an overall seasonal evolution to more enriched values throughout subsequent sampling. At 60 cm the spread was smaller (-20.4 to -18.7 ‰) but showed a similar trend in $\delta^{18}O$ values as the shallow (30 cm) soil water. Samples from 120 cm at L8 on both the seismic line (-19.4 to -18.7 ‰) and undisturbed (-19.0 to -18.7 ‰) areas have a consistent $\delta^{18}O$ signature within analytical uncertainty and are similar to the shallow groundwater samples.

Lowland Site (L12)

Lastly, the soil water isotopes at site L12 showed little variation with depth and time and were mostly within analytical uncertainty (Figure 4.11C). The spread of $\delta^{18}O$ values at 30 cm for the seismic line and undisturbed area was -18.9 to -18.7 ‰ and -18.8 to -18.3 ‰ respectively,

whereas the spread of $\delta^{18}O$ values at 60 cm for the seismic line and undisturbed area was -17.6 to -18.8 ‰ and -18.4 to -18.9 ‰ respectively. Soil water from L12 at 120 cm at both the seismic line (-19.0 to -18.8 ‰) and undisturbed (-18.8 to -18.7 ‰) is also within analytical uncertainty and similar to the shallow groundwater samples. The minimal temporal variation in $\delta^{18}O$ values at all depths can likely be attributed to the fact that peat holds a large volume of water; thus, isotopic signatures of individual precipitation events and snowpack melt are possibly buffered into an average signal.

Table 4.2: Average soil-water isotopic values for $\delta^{18}O$ and $\delta^{2}H$ and volumetric water content (VWC) from May to September separated by depth and location of sampling; sd denotes standard deviation.

Depth (cm)	Site	Location	δ18O (+/- sd) ‰	δ2H (+/- sd) ‰	# Samples	VWC (%)
30	U1	Disturbed	-	-	-	-
	U1	Undisturbed	-	-	-	-
	U2	Disturbed	-20.7 (0.4)	-162.0 (2.5)	4	0.38 (0.01)
	U2	Undisturbed	-20.2 (1.0)	-158.0 (7.6)	6	0.34 (0.06)
	U3	Disturbed	-	-	-	-
	U3	Undisturbed	-	-	-	-
	L8	Disturbed	-18.7 (0.6)	-146.6 (4.6)	7	0.41 (0.01)
	L8	Undisturbed	-22.3 (1.3)	-173.5 (9.5)	6	0.33 (0.05)
	L12	Disturbed	-18.8 (0.1)	-147.2 (0.5)	6	0.55 (0.01)
	L12	Undisturbed	-18.6 (0.2)	-145.2 (0.9)	7	0.54 (0.04)
60	U1	Disturbed	-20.0 (0.75)	-155.7 (6.1)	6	0.38 (0.01)
	U1	Undisturbed	-19.5 (0.2)	-152.2 (0.9)	4	0.38 (0.04)
	U2	Disturbed	-18.4 (0.6)	-146.7 (2.3)	2	0.38 (0.02)
	U2	Undisturbed	-20.2 (0.1)	-156.9 (0.9)	5	0.34 (0.04)
	U3	Disturbed	-20.6 (0.7)	-161.0 (4.9)	4	0.39 (0.12)
	U3	Undisturbed	-19.4 (0.5)	-153.0 (3.0)	4	0.34 (0.05)
	L8	Disturbed	-19.6 (1.3)	-153.3 (10.3)	6	0.38 (0.01)
	L8	Undisturbed	-21.6 (0.9)	-167.2 (7.5)	5	0.36 (0.01)
	L12	Disturbed	-18.8 (0.2)	-148.0 (1.3)	6	0.54 (0.04)
	L12	Undisturbed	-18.7 (0.2)	-146.4 (0.5)	9	0.79 (0.02)
120	U1	Disturbed	-19.7 (0.8)	-152.8 (6.7)	8	-
	U1	Undisturbed	-18.9 (0.5)	-147.8 (4.2)	7	-
	U2	Disturbed	-18.7 (0.2)	-146.1 (1.7)	9	-
	U2	Undisturbed	-18.9 (0.3)	-146.7 (1.4)	5	-
	U3	Disturbed	-18.8 (0.1)	-147.8 (0.6)	6	-
	U3	Undisturbed	-19.0 (0.2)	-148.5 (1.8)	6	-
	L8	Disturbed	-18.8 (0.3)	-147.0 (2.5)	4	-
	L8	Undisturbed	-18.8 (0.1)	-145.9 (1.4)	7	-
	L12	Disturbed	-18.9 (0.03)	-148.2 (0.3)	6	-
	L12	Undisturbed	-18.8 (0.05)	-147.6 (0.2)	8	-

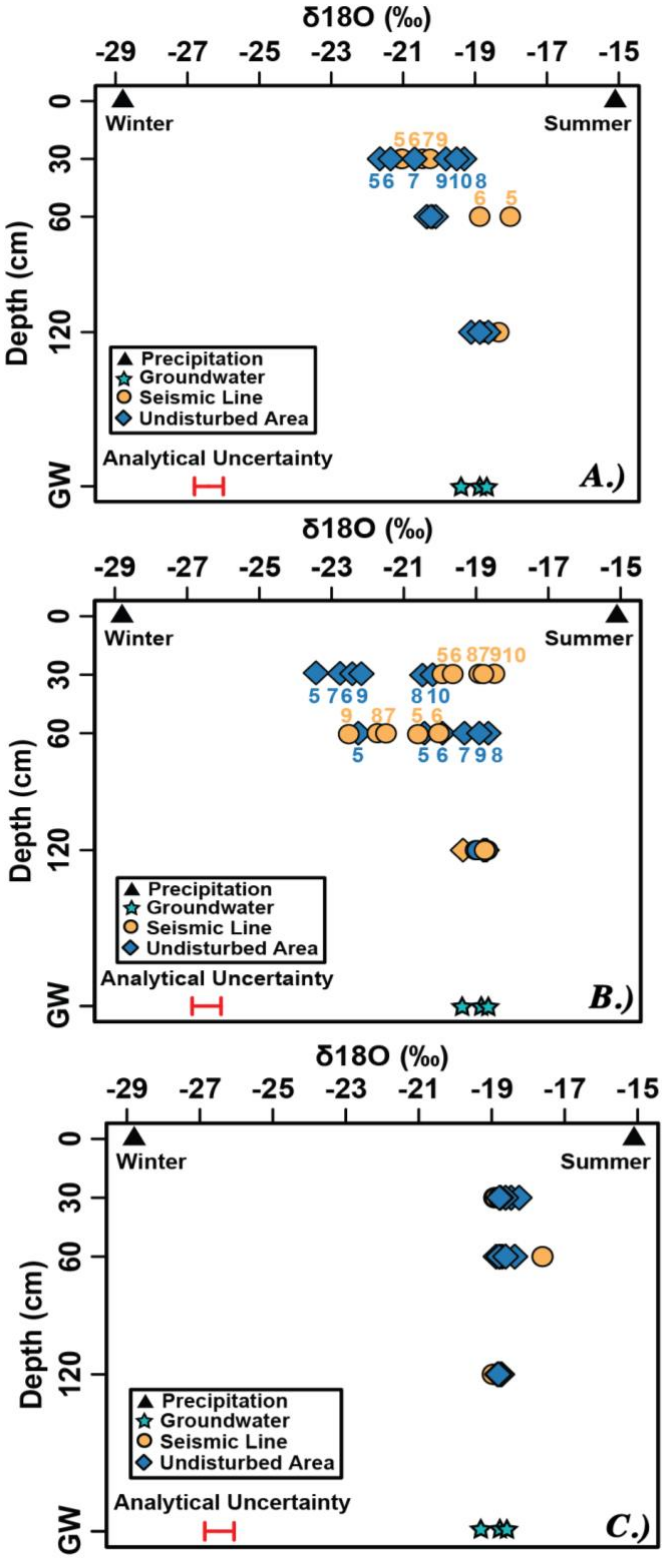

Figure 4.11: Seasonal variations in $\delta^{18}O$ values at A) U2 B) L8 and C) L12 separated by depth in the study area (numbers above points indicate month of the year). Shown for reference are shallow (~30 m) Paskapoo groundwater $\delta^{18}O$ values (+/- standard deviation) along with average winter and summer precipitation $\delta^{18}O$ values. GW denotes groundwater.

Soil Water Isotope Synthesis

Previous studies investigating the isotopic composition of soil-water differentiate between two soil-water pools: freely draining mobile water (MW) and the less mobile bulk water (BW) held by electrostatic forces on clay particles used by vegetation (Renée Brooks *et al*., 2010; Goldsmith *et al*., 2012). The isotopic signature of MW has been attributed to infiltrating meteoric water and has a strong dependence on seasonality whereas the more tightly bound BW has a complex isotopic signature (Renée Brooks *et al.* 2010; Goldsmith *et al.* 2012; Geris *et al.* 2015; Sprenger *et al.* 2018). The degree of interaction and exchange between these two soil-water pools is heavily debated and varies based on the region and method of sampling. Drier soils typically exhibit a larger isotopic difference between BW and MW due to evaporation whereas saturated soils show an isotopic signature like MW (Sprenger *et al*., 2018). For instance, BW analyzed from regions with a strong seasonal variation in precipitation and high evaporation rates is isotopically enriched relative to MW water (Renée Brooks *et al*. 2010; Goldsmith *et al*. 2012). Conversely, the difference in the isotopic composition of BW and MW has been shown to be minimal in (i) samples obtained from wetter soils at greater depths (Zhao *et al*. 2013) (ii) boreal regions with a seasonally dry northern climate (Geris *et al*. 2015) and (iii) regions with low evaporation. Overall, there is likely some exchange between MW and BW, but the relative contribution from each is difficult to quantify (Sprenger *et al*., 2018), especially with suction lysimeters, which collect a mixture of MW that is present in excess of the soil field capacity at the time of sampling and tightly bound BW (Landon *et al*., 1999) further complicating the interpretation of the soil-water $\delta^{18}O$ and $\delta^{2}H$ isotopes.

The measured isotopic signatures of soil-water in this study represents water of meteoric origin that has undergone minimal evaporation as the soil-water samples all plotted on or near the LMWL (Figure 4.10C). Other studies have noted that isotopic fractionation due to evaporation in drier regions may be captured in soil waters of shallower (10 cm) depths

(Zimmermann *et al*., 1967; Allison *et al*., 1983), which is shallower than the sampling depths in this study. Additionally, although transpiration rates are high during the growing season, transpiration does not fractionate $\delta^{18}O$ and $\delta^{2}H$ isotopes unless soil-conditions are extremely dry (Zimmermann *et al*., 1967). The observed patterns of meteoric water infiltration into the soil following spring melt and a subsequent shift to more enriched $\delta^{18}O$ and $\delta^{2}H$ values following summer precipitation events has been observed in other studies of soil water using suction-lysimeters (Landon *et al*., 1999) and was most evident in the shallow soil-water samples (30 and 60 cm) in this study. The deep (120 cm) soil water samples in this study exhibited limited variation in soil-water $\delta^{18}O$ and $\delta^{2}H$ isotopes and were similar to the shallow groundwater samples from the regional Paskapoo aquifer. The exception to this was 120 cm soil water samples from U1 (see appendix Figure 03), which showed more variation in $\delta^{18}O$ and $\delta^{2}H$ values likely indicating a faster turnover rate of soil water from infiltrating meteoric water deeper into the soil profile. However, overall, the isotopic signature of 'deeper' (1.2 m) soil waters in this study is consistent with the shallow (~ 25 m) groundwater in the study region, which is thought to receive recharge primarily via local meteoric infiltration. This vertical recharge is limited, however, having been estimated to be between 0 and 70 mm/year (Guarin-Martinez, 2022)

4.4 Vegetation Surveys

Bar plots were created to visualize percent cover of the different functional groups (graminoids, trees, forbs, shrubs, and bryophytes) on the seismic lines and the adjacent undisturbed areas in the upland (Figure 4.12) and lowland (Figure 4.13) study sites. Percent cover for each functional group was separated based on measurements obtained on the seismic centerline, edge, and randomly chosen locations in the adjacent undisturbed area. The exception to this separation scheme was for the trees and shrubs in upland sites where measurements from the center and edge of seismic lines were combined. This was done because a previous study comparing the location of survey sampling points across the width

of a seismic line for upland forests found no significant differences in tree or shrub counts (Jones *et al*. 2022).

Table 4.3: Measured tree heights for selected trees in an upland study site (U1) and a lowland study site (L8).

Location	U1		L8
	Balsam Poplar (m)	White Spruce (m)	Black Spruce (m)
Seismic Line	6.4 (n = 8)	4.6 (n = 11)	3.2 (n = 36)
Undisturbed Area	38.1 (n = 3)	15.7 (n = 5)	14.1 (n = 36)

Graminoid cover is greater on seismic lines in the upland and lowland ecoregions (Figures 4.12 – 4.13). Similarly, bryophyte cover was higher on undisturbed areas at both ecosites (Figures 4.12 – 4.13) and showed much greater abundance in the lowland study sites (Figure 4.13). Tree cover in the upland mixedwood ecosites was dominated by poplar (*Populus balsamifera*) and white spruce (*Picea galuca*), and significant differences were observed in tree height (Table 4.3) and percent cover (Figure 4.12) between on- and off seismic line. Shrub cover in the upland mixedwood ecosites was dominated by twinberry honeysuckle (*Lonicera involucrate*), thimbleberry (*Rubus parviflorus*), and red raspberry (*Rubus idaeus*). No significant differences in percent shrub cover were observed between the seismic line and adjacent undisturbed areas at our upland study sites (Figure 4.12). The lowland ecosite study areas were dominated by black spruce (*Picea mariana*) and willow (*Salix spp.*) and no significant differences in percent cover were observed between the seismic line and adjacent undisturbed areas (Figure 4.13), but significant differences were observed for tree height (Table 4.3). Shrub cover in the lowland study areas was overwhelmingly Labrador tea (*Rhododenron groenlandicum*) and significantly less shrub cover on seismic centerlines compared to the seismic line edges and the adjacent undisturbed areas (Figure 4.13).

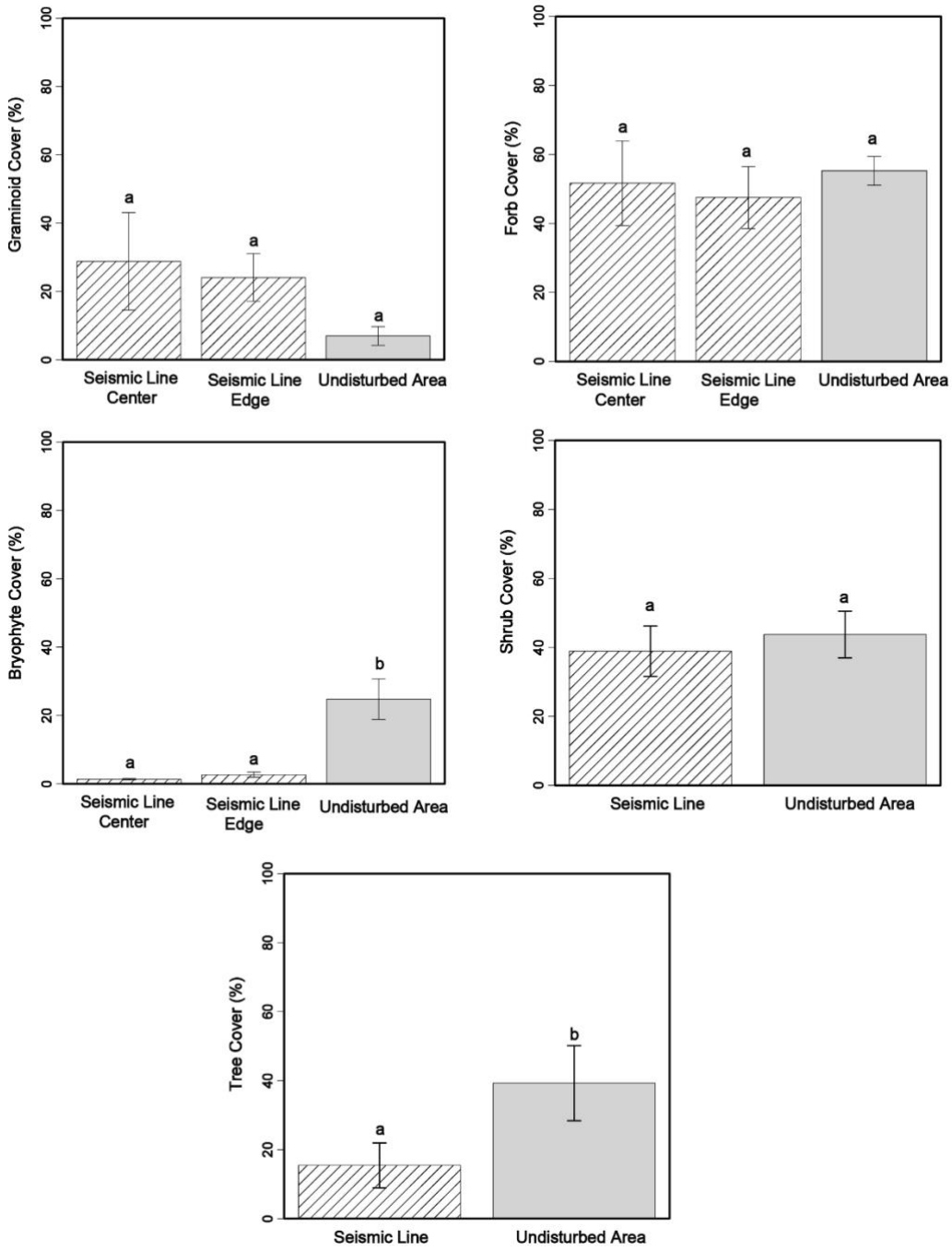

Figure 4.12: Bar charts of average percent cover by functional group of the upland study sites with standard error bars. Lower-case letters indicate significant differences among survey location based on permutational analysis of variance (perMANOVA) (Seismic Line Center: n = 6; Seismic Line Edge: n = 12; Undisturbed Area n = 18). Regions with the same letter are not significantly different at $\alpha = 0.05$.

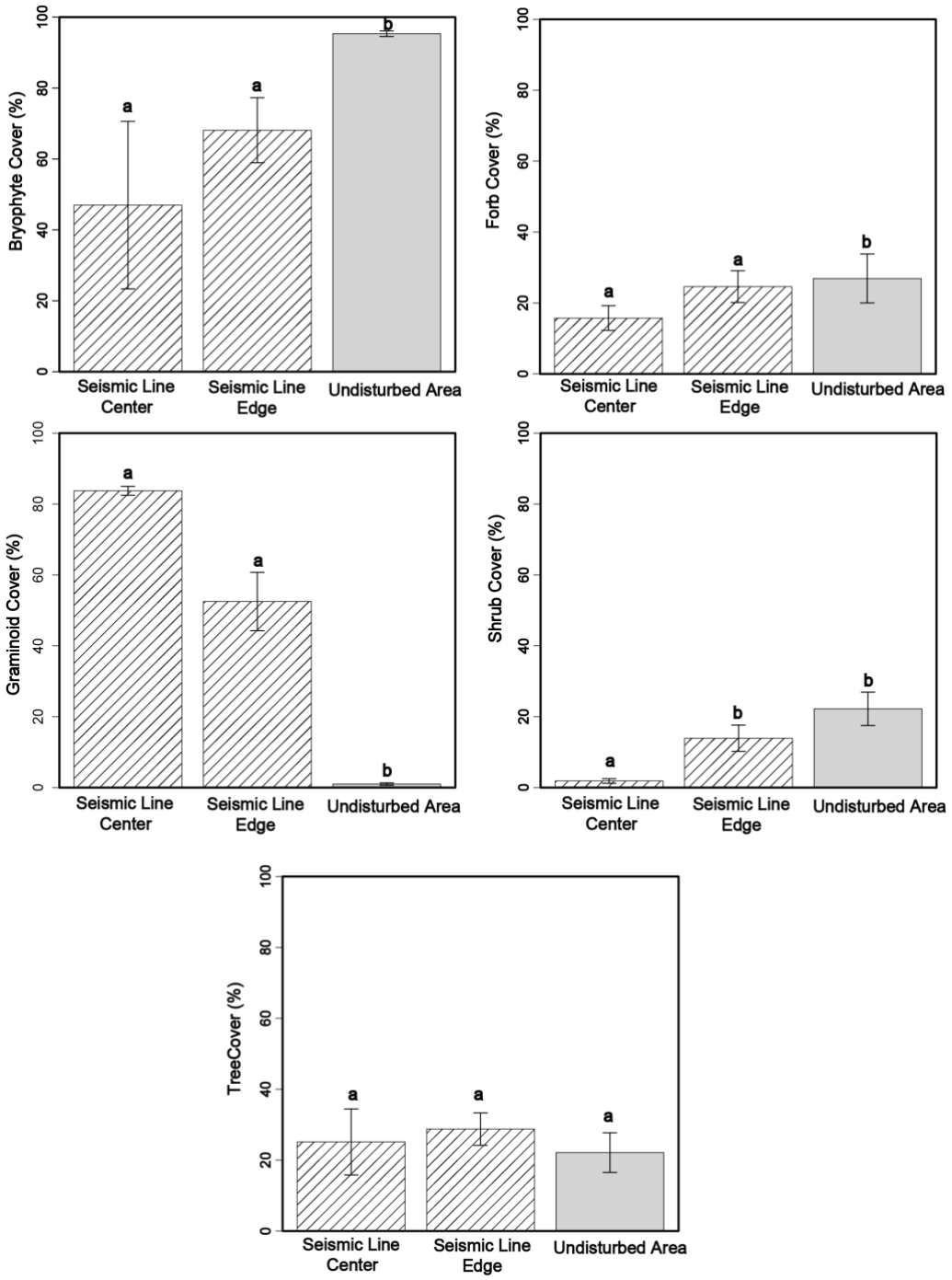

Figure 4.13: Bar charts of average percent cover by functional group of the lowland study sites with standard error bars. Lower-case letters indicate significant differences among survey location based on permutational analysis of variance (perMANOVA) (Seismic Line Center: n = 4; Seismic Line Edge: n = 8; Undisturbed Area n = 12). Regions with the same letter are not significantly different at $\alpha = 0.05$.

Vegetation Data Synthesis

The significantly greater graminoid cover on seismic lines at both ecosites (Figures 4.12 - 4.13) has been observed in other studies and has been attributed to the fact that graminoids are great colonizing species that typically outcompete native vegetation in disturbed areas such as seismic exploration lines (Dabros *et al.*, 2018). Similarly, percent cover of bryophytes is significantly higher on the undisturbed areas (Figures 4.12 - 4.13), with greater abundance in lowland sites, as bryophytes are a disturbance intolerant species and their establishment is largely dependent on moisture content and net radiation, thriving in shaded, cool, and wet regions (Jorgenson *et al.*, 2010). Given the moisture deficit and exposed canopy of seismic line impacted upland sites, bryophyte abundance is typically lower (Revel *et al.*, 1984) relative to seismic line impacted lowland sites (e.g. *sphagnum* peatlands), which have a much higher moisture content favoring the presence of bryophytes (Dabros *et al.*, 2018).

The lower density of trees on seismic lines in the upland study sites is likely because the undisturbed forest adjacent to the seismic line intercepts the majority of sunlight and shades the seismic line, which hinders the recovery of shade intolerant trees (such as Poplar trees) on seismic lines (Lee and Boutin, 2006; MacFarlane, 2013). The establishment of trees on seismic lines in lowland sites is particularly limited/slow due to the high antecedent moisture content in these sites (van Rensen *et al*., 2015; Filicetti *et al*., 2019).

The high moisture content on seismic lines is exacerbated by the combination of microtopography loss and removal of vegetation as a result from seismic line construction, both of which contribute to water ponding, especially following heavy summer rainfall events. Soil saturation limits tree rooting depth (Grossnickle, 2000) and overall tree growth because of reduced soil temperatures (Bonan, 1989; Caners and Lieffers, 2014). The significant difference in shrub cover on the seismic line center and edge of the lowland ecosite is likely attributed to greater light levels (MacFarlane, 2013) and a lower soil moisture content

on seismic line edges relative to seismic line centers allowing a greater degree of woody vegetation recovery on the seismic line edges.

4.5 Measured Weather Data

4.5.1 Temperature

The average monthly measured annual air temperature for study sites U1 and L8 for May 2022 to April 2023 was similar among all four locations (Figure 4.14). The recorded monthly high occurred in August and was 17.1°C, which was near the historical mean, whereas the lowest monthly temperature occurred in December (one month earlier than the historical mean) and was -18.2°C, below the historical low of -15.2°C. The temperature in January was markedly higher than the historical mean, close to the historical high.

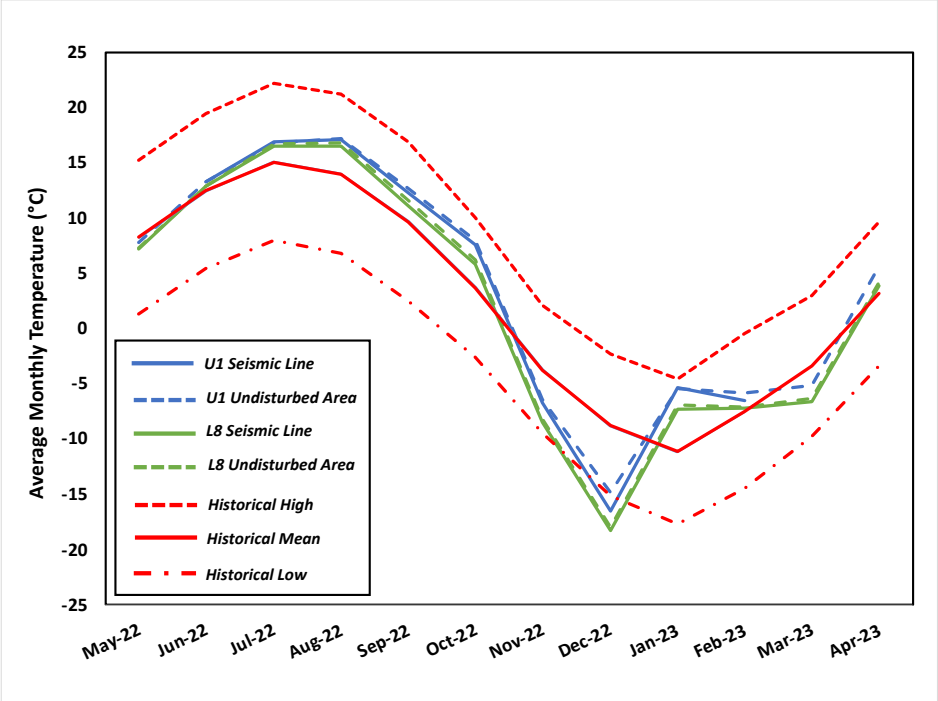

Figure 4.14: Average monthly measured air temperature among the study sites (U1 and L8, for both on and off a seismic line). Also depicted are the historical (21-year: 1991-2012) temperature low, mean, and high based on the Fox Creek Junction weather station.

4.5.2 Precipitation

The total monthly measured precipitation among the two study sites is depicted in Figure 4.15 along with the historical mean monthly precipitation in the region. The seismic line on site U1 received a total amount of 442.9 mm of precipitation over this 12-month

period, which is close to the long-term historical mean of 485.4 mm, whereas the adjacent undisturbed area received 393.8 mm. The seismic line on site L8 received 610.2 mm, which is 124.8 mm higher than the historical mean annual precipitation, whereas the adjacent undisturbed area received 484.1 mm.

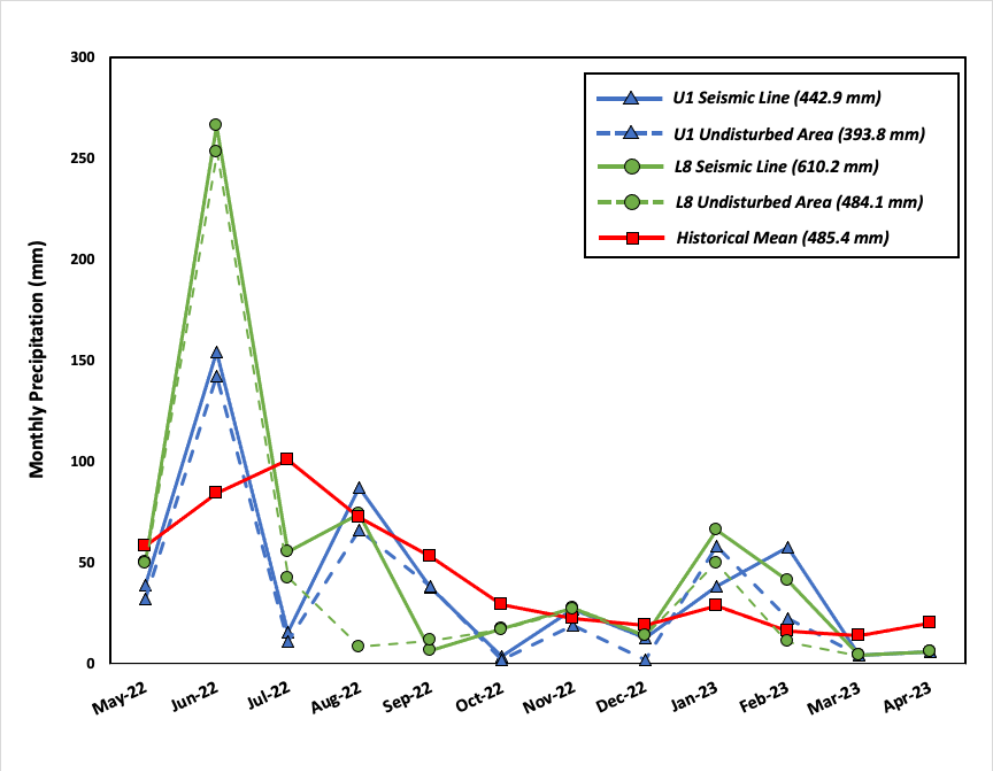

Figure 4.15: Monthly precipitation among the study sites. Also depicted are the historical (21-year: 1991--2021) precipitation means based on the Fox Creek Junction weather station.

4.5.3 Wind Speed

The monthly measured windspeed at each site is shown in Figure 4.16. To determine if it is appropriate to use the recorded weather station data on the seismic line as the upper boundary input data for the adjacent undisturbed area, windspeed was compared using the permutational multivariate analysis of variance, or PERMANOVA, method, which is a non-parametric multivariate statistical permutation test based on the daily wind speed values for each month. For site U1 at $\alpha = 0.05$, no significant differences among windspeed on the seismic line and the adjacent undisturbed area were observed across all months. Thus, it was considered reasonable to use the weather data from the seismic line to run simulations on the

undisturbed area for site U1. Conversely, for site L8, significant differences were observed for all months, with the seismic line having a statistically significantly higher windspeed each month. However, as no other data were available, the simulation for the undisturbed area in site L8 was run using the weather data from the seismic line, keeping in mind that the simulated ET was likely to be overestimated and that other water budget components would therefore be affected as well due to the higher measured windspeed on the seismic line compared to the undisturbed area for L8.

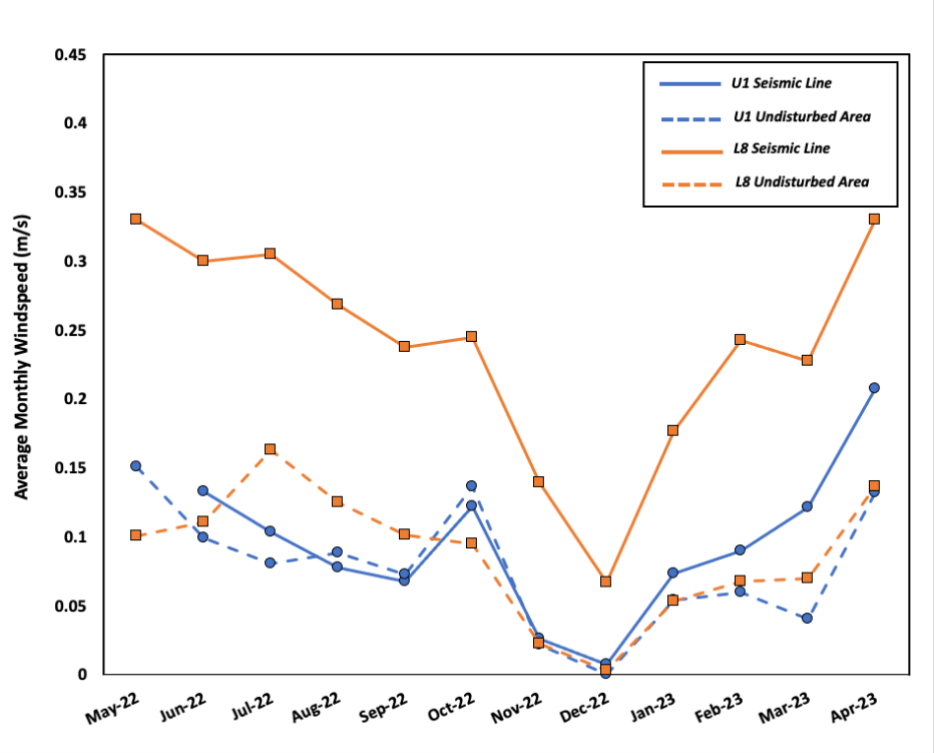

Figure 4.16: Monthly measured wind speed between the seismic line and the adjacent undisturbed area for the two study sites U1 and L8.

4.5.4 Net Radiation

The average monthly measured net solar radiation for each site is depicted in Figure 4.17. From May to August net solar radiation was higher on the seismic line compared to the adjacent undisturbed area, mainly due to the smaller and sparser vegetation. The largest recorded net radiation values occur in July where they reach up to 134 W/m^2. July is also when the largest difference in net radiation between the seismic line and undisturbed area

occurs by 31 W/m^2 and 53 W/m^2 for U1 and L8 respectively. Net radiation is lowest during the winter months and reaches its lowest value (~ 3.0 W/m^2) in December.

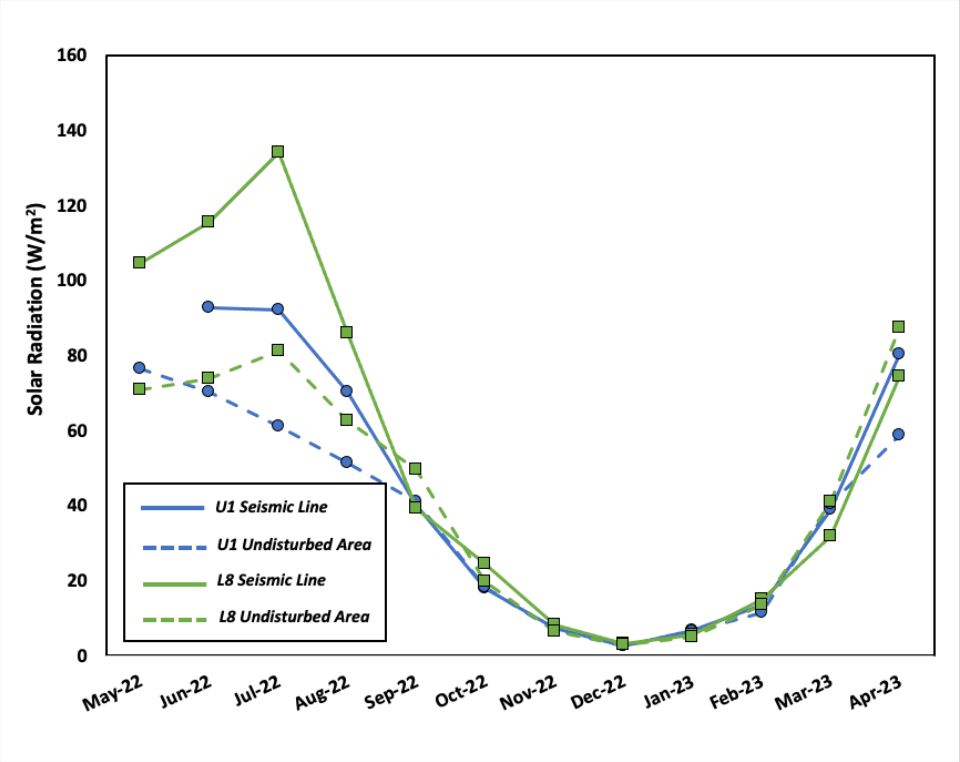

Figure 4.17: Monthly measured solar radiation among the seismic line and the adjacent undisturbed area for all study sites.

4.5.5 Snow Data

4.5.5.1 Snow Depth

Snow depth measurements at the five sites from the 2021 – 2022 winter season (November to April), ranged from 6 cm to 87 cm with a median of 33.0 cm (n = 232) (Figure 4.18). Peak snow accumulation occurred in February with a mean total depth of 60.1 (±20.1) cm across all sites. At peak snow accumulation, snow depth measurements on the seismic lines for sites U1, U3, and L12 showed statistically more accumulation (α = 0.05) than their respective adjacent undisturbed areas (Figure 4.18), receiving 37.3 cm, 52.8 cm, and 5.0 cm more snow than their adjacent undisturbed areas respectively. Conversely, the undisturbed area at site 2 (U2) showed statistically more snow accumulation than the adjacent disturbed area. For instance, at peak accumulation in February, the undisturbed area had on average 17.3 cm more snow than its adjacent disturbed area at this site. Possible reasons for this could

be that the seismic line on this site had experienced more vegetation recovery than other sites, which would enhance storage of snow on vegetation, and this could also be coupled with local topographic variations and wind redistribution. Site L8 generally showed similar amounts of snow accumulation on and off the seismic line, which could be attributed to the similar degree of canopy cover at this site based on previous leaf-area index (LAI) measurements. Following peak snow-accumulation in February, the snowpack began to melt and was completed by late May. December snow depth measurements in the following winter (2022 – 2023) again showed a similar amount of snow accumulation at L8 (Figure 4.18). Interestingly, the snow depth in February at U1 was considerably less, by ~ 35 cm for both on and off the seismic line compared to the previous year's sampling, which likely resulted from less precipitation in this area. This was not the case for site L8.

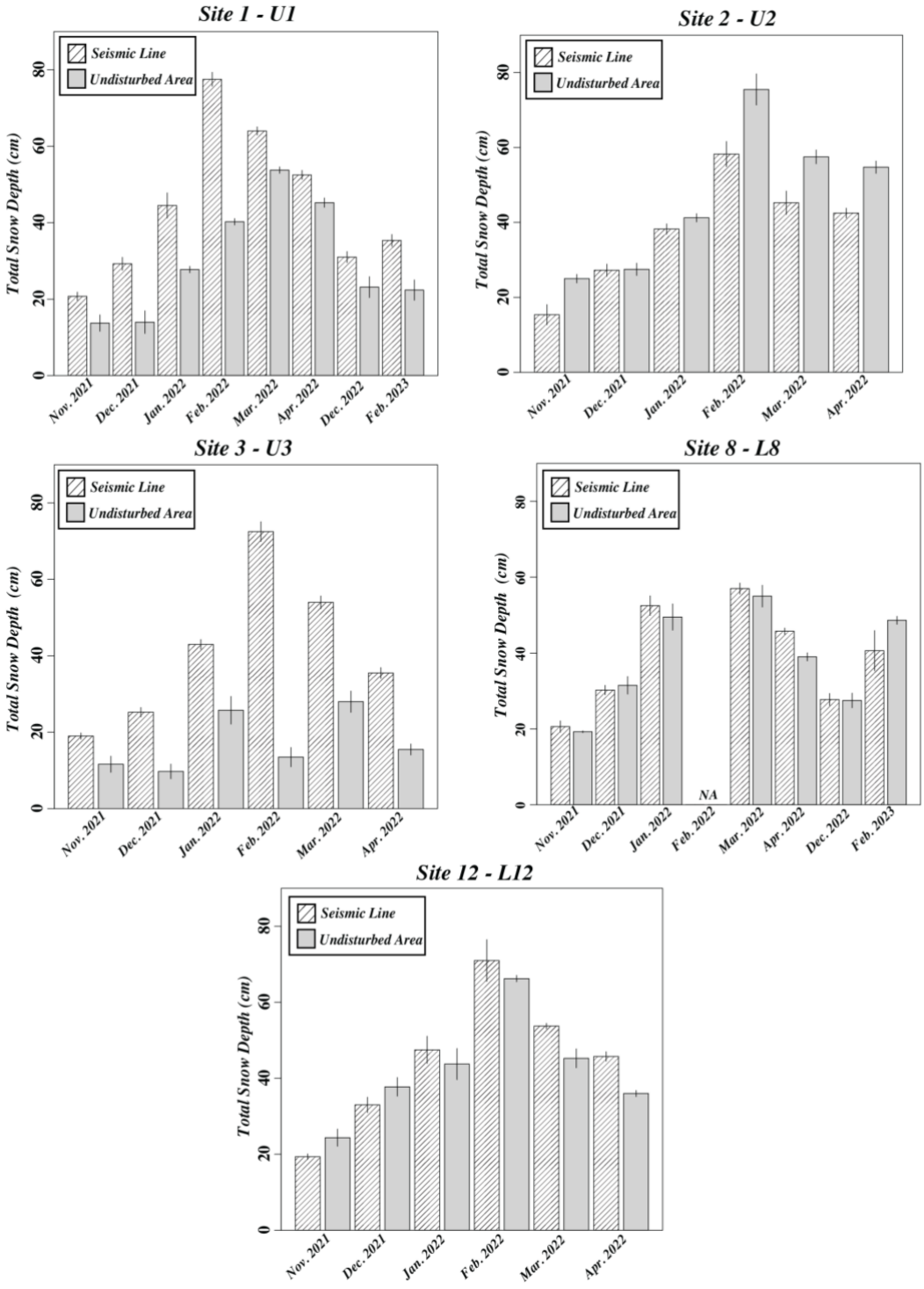

Figure 4.18: Bar graphs with ± 1 standard deviation error bars for total monthly snowpack depth measurements at each site (each bar represents 4 measurements).

4.5.5.2 Snow Density

Snow density measurements over the total thickness varied from lows of 25 kg/m^3 during the cold and dry months of November – January to 528 kg/m^3 during the warmer and wetter months of March and April when the snowpack was melting (Figures 4.19 to 4.21). Unsurprisingly, samples obtained from the upper 5 and 10 cm of the snowpack (Figures 4.19, 4.20) showed the greatest monthly variations in snow-density values compared to the monthly variations of total snowpack density (Figure 4.21). When considering the total snowpack (Figure 4.21), density generally ranged between 100 and 300 kg/m^3. It was lowest early in the winter (November – December) when fresh snow was deposited, and the density increased to a relatively unchanged mean value of 402.7 kg/m^3 (+/- 144.6 kg/m^3) in March (Figure 4.21).

Differences in snow density between the seismic line and adjacent undisturbed area are mainly observed in the upper 5-cm of the snowpack and diminish with sampling depth. Across all sites, snowpack density for the upper 5-cm and 10-cm layers was lower early in the winter (generally being <200 kg/m^3 between November and January). The lowest values at all sites are observed in January (<100 kg/m^3), likely due to the cooler weather and drier conditions. Values are typically between 200 and 300 kg/m^3 in February and between 300 and 500 kg/m^3 in March and April, with April showing the highest value. Snow samples from two upland study areas (U1 and U3) showed statistically higher snow-densities (α = 0.05) on the seismic line during mid- to late winter (February – April) compared to their adjacent undisturbed areas (Figure 4.19). Upland study site U2 showed no significant differences in snow density between the seismic line and adjacent undisturbed area, likely due to the factors described previously regarding variations in snow depth at this site (similar vegetation, local topography, wind redistribution). The higher snow density on the seismic lines at sites U1 and

U3 compared to their respective undisturbed areas are consistent with the fact that seismic lines typically receive more solar radiation due to the lack of overstory (Figure 4.17) and are exposed to higher wind speeds (Figure 4.16) than undisturbed areas (Dabros *et al*. 2018), which would contribute to the densification of snow at these areas. Interestingly, for the lowland sites (L8 and L12), the opposite trend was observed, where undisturbed areas showed higher snow-density values in the upper 5 cm of the snowpack compared to their adjacent disturbed areas (Figure 4.19).

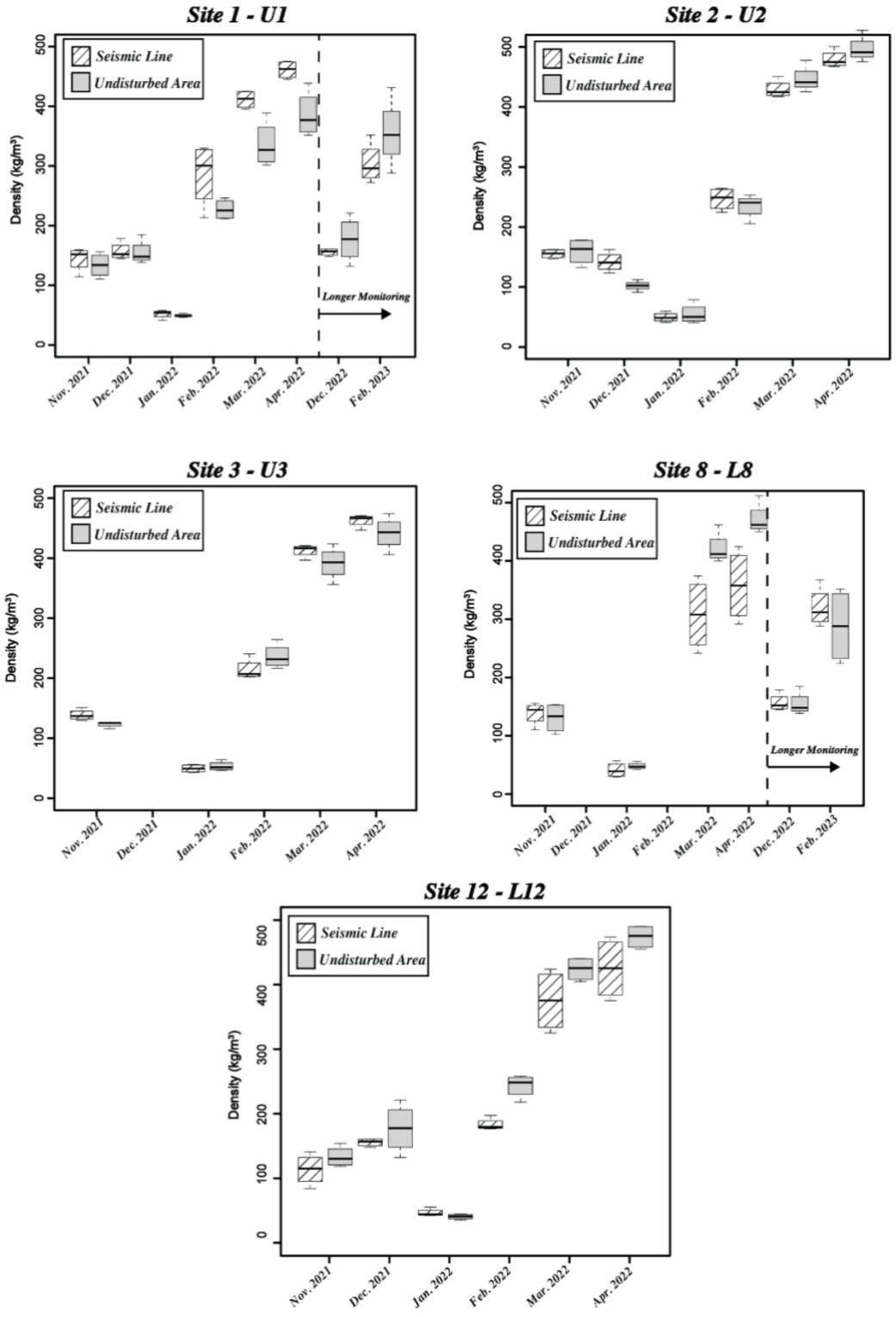

Figure 4.19: Bar graphs with ±1 standard deviation error bars for monthly upper 5-cm snowpack density at each site (each bar represents 4 measurements).

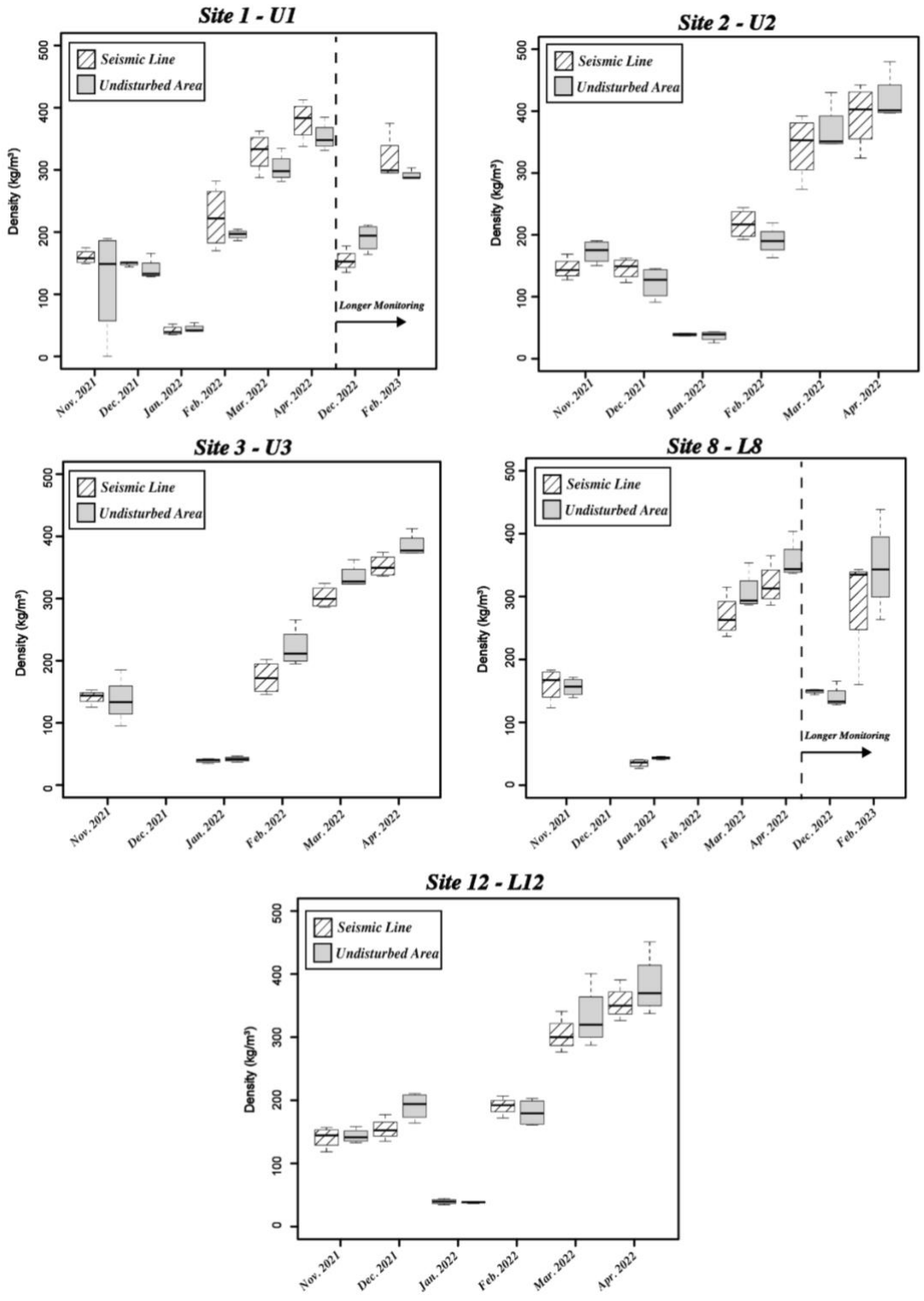

Figure 4.20: Bar graphs with ±1 standard deviation for monthly upper 10-cm snowpack density at each site (each bar represents 4 measurements).

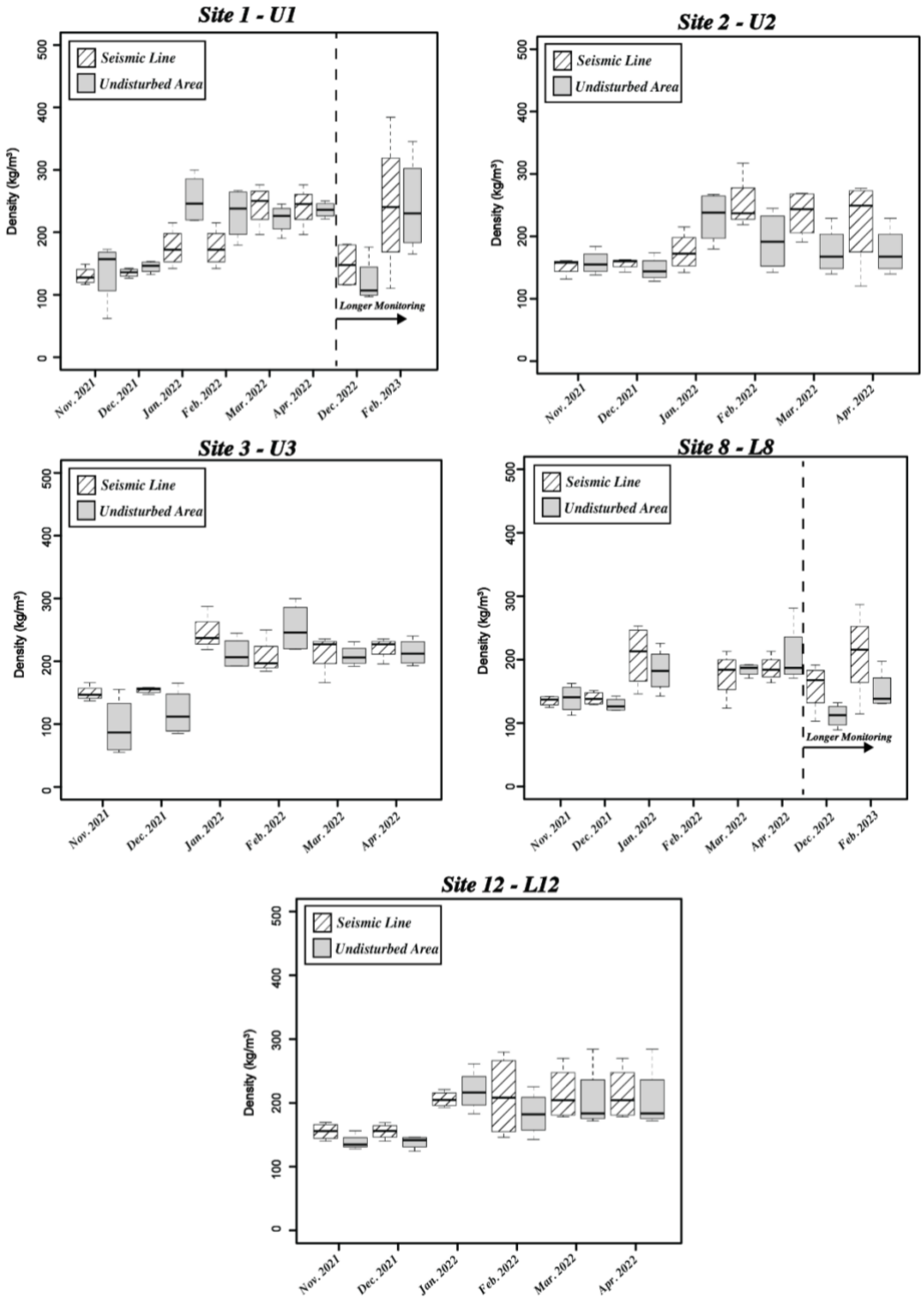

Figure 4.21: Bar graphs with ± 1 standard deviation for monthly total snowpack density at each site (each bar represents 4 measurements).

4.5.5.3 Snow Water Equivalent (SWE)

Apart from Site U2, seismic lines at all study sites showed a higher monthly SWE compared to their adjacent undisturbed areas. During the 2021 to 2022 winter season, peak SWE occurred in February for all sites with a mean value of 147.6 ±40 mm for all the seismic line sites compared to 108.3±55 mm for all the adjacent undisturbed area sites.

Table 4.4: Monthly SWE values (in mm) for study sites within the watershed based on total monthly snowpack thicknesses. Values in brackets indicate the uncertainty in SWE arising from monthly variations in replicate measurements of snow density and snow depth at each location.

Survey Date	Site 1 Seismic Line	Site 1 Undisturbed	Site 2 Seismic Line	Site 2 Undisturbed	Site 3 Seismic Line	Site 3 Undisturbed	Site 8 Seismic Line	Site 8 Undisturbed	Site 12 Seismic Line	Site 12 Undisturbed
2021										
21-Nov	27.0 (4.1)	19 (9)	23.4 (8)	39.5 (6)	28.3 (3)	11.2 (7)	27.9 (4)	26.8 (5)	46.7 (6)	33.7 (7)
20-Dec	39.6 (5.0)	21 (8)	42.6 (6)	40.5 (7)	38.9 (4)	11.6 (6)	42.1 (5)	40.6 (7)	51.2 (8)	52.2 (8)
2022										
27-Jan	78.1 (18.0)	70.1 (12)	67.1 (13)	95.2 (18)	105.4 (14)	54.7 (17)	108.3 (28)	90.6 (21)	97.8 (16)	95.8 (23)
25-Feb	135.9 (24.8)	92.8 (17)	147.1 (31)	145.3 (40)	150.0 (24)	49.9 (11)	***NA***	***NA***	149.5 (52)	121.3 (23)
24-Mar	155.7 (22.3)	92.7 (10)	107.1 (23)	101.1 (23)	115.5 (19)	27.1 (9)	100.5 (22)	101.7 (9)	115.2 (23)	93.1 (26)
21-Apr	126.4 (19.1)	95.6 (8)	89.0 (30)	88.8 (20)	96.3 (9)	28.4 (8)	91.7 (10)	92.9 (23)	103.8 (21)	82.3 (21)
20-Dec	45.9 (12.2)	28.8 (10.0)	***NA***	***NA***	***NA***	***NA***	43.7 (12)	30.7 (7)	***NA***	***NA***
2023										
16-Feb	86.3 (40.6)	54.4 (22)	***NA***	***NA***	***NA***	***NA***	84.6 (36)	73.5 (16)	***NA***	***NA***

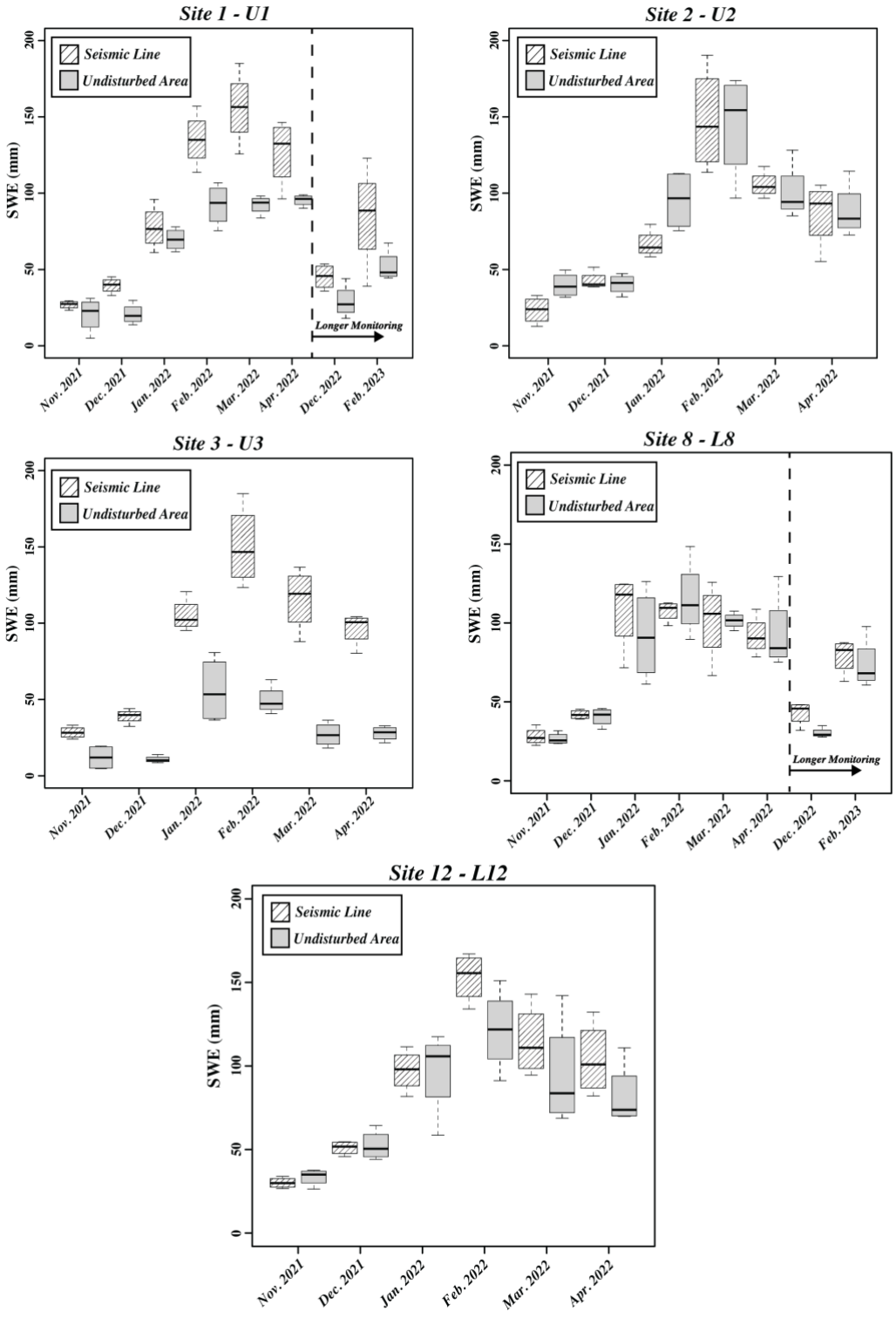

Figure 4.22: Bar graphs with ±1 standard deviation for monthly snow water equivalent (SWE) at each site (each bar represents 4 measurements).

Snow Data Synthesis

On a watershed scale, snowpack properties vary spatially and temporally with accumulation and ablation as the main drivers for snow depth and density. Although this is a good initial estimate of SWE within the Fox Creek study area, more snow measurements would be needed to have a true characterization of the study area for two reasons. First, most of the study sites in this thesis are in the central to eastern part of the watershed that typically receives less precipitation than the western portion of the watershed, which is closer to the Rocky Mountains. Thus, to quantify spatial variation of snow-cover within the watershed, more study sites would need to be established in the western portion of the watershed. Secondly, a longer snow-cover record is needed to capture the inter-annual variability of climate processes, which can interact with the vegetation canopy within a certain location producing different snow conditions from year to year (Sun *et al.* 2022).

The snow density values in this study fall within the range of snow density from other Canadian studies, which mostly range from 50 – 120 kg/m^3 for fresh snowfall during cold and dry conditions to 350 to 500 kg/m^3 for melting snowpacks (Pomeroy *et al.,* 1998). Dry snow densities for boreal forest regions with < 1 m vertical snowpack depth typically reach a maximum value of ~ 250 kg/m^3 (Gray and Prowse, 1993).

However, snow density measurements obtained via the sampling tube represent some degree of uncertainty due to potential compaction of fresh snow when using the sampling tube, snow loss when removing the tube from the snowpack, and/or sampling when ice layers are present (Beaudoin-Galaise and Jutras, 2022). The presence of ice layers can plug the sampling tube preventing further snow from entering the tube when inserted beyond the ice layer. This results in a potentially under represented snow sample with respect to the true mass and density of the undisturbed snow (Beaudoin-Galaise and Jutras, 2022). To prevent this in future measurements of snow parameters within the watershed, a larger diameter snow

sampler such as the one described by Beaudoin-Galaise and Jutras (2022) should be used, as it tends to have the lowest degree of uncertainty amongst various SWE measuring instruments.

4.6 Soil Water Content, Temperature, and Response to Precipitation

Since the upland sites (U1, U2, and U3) all showed similar results, going forth, only U2 will be fully discussed as it has a more complete sampling record. Data from U1 and U3 are available in Appendix D. Figures 4.23 to 4.25 show a time series of soil moisture for sites U2, L8 and L12 from May 1st until October 31st, 2022.

Soil Moisture and Temperature Sensors

All recorded soil-temperature measurements in this study fell within the operating range of the sensors (see section 3.1). Similarly, all SWC measurements (apart from 60 cm on the undisturbed area of L12) fell within the operating range of the sensors used in this study.

Upland Site 2 (U2)

From early winter (November) to mid-January, soil-water content (SWC) at 15 cm for the seismic line and the adjacent undisturbed area declined from 36.1% and 31.1% to 11.7% and 18.7% respectively due to a drop in soil-temperature to below 0°C and the development of soil-frost (Figure 4.23A, 4.23B). Some pore water can remain unfrozen even when the soil temperature drops below 0°C and, often, a soil temperature well below zero is required to freeze the pore water in the smaller pores. From January 20 – 26th, air-temperature was above 0°C and reached up to 6.2°C resulting in the soil-temperature at 15 cm depth for both the seismic line and the adjacent undisturbed area to increase above 0°C. As a result of this, the SWC for seismic line and the adjacent undisturbed area increased to 35% and 33.4% respectively. The thaw of soil-frost occurred first on the undisturbed area and was ahead by ~ 4 days compared to the adjacent seismic line. Other studies have also observed delayed snow melt on seismic lines compared to the adjacent undisturbed areas due to a higher surface albedo on the seismic lines because of less vegetation and more snow accumulation (Haag

and Bliss, 1974; Bjorkman *et al*., 2015; Dabros *et al*., 2018). SWC during the winter for both the 30 cm and 60 cm depths for the seismic line and the adjacent undisturbed area remains relatively constant with slight variations in late winter for the 60 cm depth on the seismic line. Following spring 2022 melt (May), the soil-profile of both the seismic line and the adjacent undisturbed area (Figure 4.23A) became saturated and the SWC at all measurement depths showed little variation or response to precipitation until mid-July.

In mid-July of 2022, SWC declined on the seismic line (apart from the 15 cm measurement depth) and the adjacent undisturbed area. On the seismic line, SWC at 30 cm and 60 cm declined by 3% and 5% SWC, respectively. In contrast, on the undisturbed area, SWC at 15 cm, 30 cm, and 60 cm declined slightly more, by 9%, 5%, and 5% respectively. The decline in SWC at this time is likely due to enhanced evapotranspiration (ET). Following the decline in SWC for on- and off-seismic line in mid-July, both soil profiles show a response in SWC following precipitation events (up to 10% increase in SWC for the off-line site at the 15 cm depth in late September). A similar pattern in SWC is observed in summer 2021 following precipitation events.

Overall, SWC at the 15 cm depth is statistically significantly higher on the seismic line compared to the undisturbed area in the fall by 8.1% SWC. This is likely because grasses and other understory species, which are dominant on a seismic line, go dormant faster and use less water compared to trees and shrubs which are dominant on the adjacent undisturbed area and use water for longer periods of time leading to a moisture accumulation (Mathys *et al.* 2013) on the seismic line. In the spring, SWC is statistically significantly higher on the adjacent undisturbed area, but only by 2.3%, this being within the sensor accuracy (+/- 3.0% SWC). Although within the sensor accuracy, the higher SWC on the undisturbed area in the spring may be because snow melt is delayed on a seismic line compared to the adjacent undisturbed area. No statistical differences in SWC are observed in the winter and summer (Figure 4.26A). In the summer, there is not a significant difference in SWC. This may be

because plant species on the seismic line and the adjacent undisturbed area, although different, are transpiring at relatively similar rates and other factors such as differences in soil temperature, drainage, and runoff between the seismic line and undisturbed area.

Similarly, SWC at 30 cm depth is significantly higher on the seismic line compared to the adjacent undisturbed area in the fall by 5.8% but is relatively similar in the other three seasons (Figure 4.26B). At 60 cm depth, SWC is always significantly higher on the seismic line (Figure 4.26C) which may be attributed to (i) the soil temperature always being significantly higher at 60 cm on the seismic line compared to the adjacent undisturbed area due to the vegetation on seismic lines having a lower albedo compared to the adjacent undisturbed area and/or (ii) limited to no trees on the seismic lines and thus no roots drawing up water from 60 cm. The largest difference in SWC between the seismic line and adjacent undisturbed area occurs in the fall where for the depths of 15 cm, 30 cm, and 60 cm it is 8.2%, 5.8%, and 3.5% greater on the seismic line respectively. As mentioned previously, this is likely because trees go dormant later compared to grasses and understory species on the seismic line. In the winter, spring, and summer, the difference in SWC between the seismic line and adjacent undisturbed area is not as significant.

Soil-temperature for the 15 cm and 30 cm depths is statistically significantly higher on the seismic line compared to the adjacent undisturbed area in the winter, however the difference is within the uncertainty of the sensors ($\pm$ 0.5°C) (Table 4.5). In the summer, soil-temperature for the 15 cm and 30 cm depths is significantly higher on the seismic line compared to the adjacent undisturbed area by at least 0.7°C. Soil temperature has similar values in the spring and fall (Figure 4.26D, 4.26E). At 60 cm depth, soil temperature is always significantly higher on the seismic line (Figure 4.26F). The largest soil-temperature difference between the seismic line and adjacent undisturbed area was observed in the summer where at depths of 15 cm, 30 cm, and 60 cm are 0.8°C, 0.7°C, and 1.2°C,

respectively greater on the seismic line. In the fall, winter, and spring, the difference in soil-temperature between the seismic line and adjacent undisturbed area is not as significant.

Lowland Site 8 (L8)

Somewhat surprisingly, SWC values for this site are quite similar to those of the upland sites, mostly varying between 30% and 40% (Figure 4.24). Similar to U2, spring melt was delayed on the seismic line compared to the adjacent undisturbed area and following spring melt at L8, the SWC increases on the seismic line (43.0%, 40.7%, and 38.5% SWC for 15 cm, 30 cm, and 60 cm respectively) and the SWC remains relatively constant for all seasons (apart from the winter) for each depth, showing little to no response to precipitation events. SWC also increased on the undisturbed area following spring melt (~ 37% for 15 cm, 30 cm, and 60 cm) and exhibits little response to precipitation events until after mid-July (with the exception of the SWC at 15 cm which shows a considerable rise in early July following large precipitation events). In August, SWC began to steadily decline at 15 cm and 30 cm depths likely due to higher ET rates during this period. In the winter, SWC for the 15 cm depth declines from 39.7% to 14.4% for the seismic line, whereas for the adjacent undisturbed area it declines from 26.5% to 15.4%, because a significant portion of the pore water becomes frozen.

Overall, SWC at the 15 cm depth is significantly higher on the seismic line compared to the undisturbed area for all seasons apart from spring (Figure 4.27D). Similarly, at both the 30 cm and 60 cm measurement depths, SWC is also significantly higher on the seismic line compared to the adjacent undisturbed area, although the differences are less marked at 60 cm. This is likely mainly because (i) the seismic line site has a silt-loam texture that does not drain well and retains more water, whereas the adjacent undisturbed site was a coarser well-drained sandy-loam and (ii) trees come out of dormancy earlier and start using water compared to understory species which use water more heavily in the summer. In the summer, soil-temperature was significantly higher at all depths on the seismic line compared to the adjacent

undisturbed area on average by 1.6°C, 1.4°C, and 1.1°C for 15 cm, 30 cm, and 60 cm respectively (Figure 4.27 D to F), likely due to the lack of protection from dense vegetation.

Lowland Site 12 (L12)

Similar to sites U2 and L8, spring-melt at site L12 was delayed on the seismic line (by around ~ 6 days) compared to the adjacent undisturbed area. Following spring melt, L12 showed a similar SWC increase to sites U2 and L8 at 15 cm on the seismic line (Figure 4.25A) and remained relatively constant for all seasons apart from: (i) the winter where it drops due to soil frost formation and (ii) the summer where fluctuations in SWC are caused by precipitation and higher plant water usage. However, unlike all other study sites, the SWC at L12 was much higher (generally > 50% SWC) at all measurement depths both on- and off the seismic line. This is likely because this site is located in a regional topographic low and has a thick (> 1 m) peat accumulation, and peat is known to have higher water holding capacity than mineral soil.

Unlike the other study sites, SWC at 15 cm was significantly higher on the undisturbed area during the winter and spring by 15.9 and 10.2% respectively compared to the seismic line, likely due to the presence of higher organic matter which has higher water holding capacity, whereas during the summer, SWC was similar and in the fall, the disturbed area was higher by 10.7% as less subject to ET (Figure 4.28A). Similarly, at 30 cm, SWC was significantly greater on the undisturbed area compared to the seismic line in the winter and spring, although less markedly, by 2.6% and 4.0% respectively, and was comparable not only in the summer, but also in the fall (Figure 4.28B). Quite surprisingly, SWC on the undisturbed area at 60 cm (Figure 4.28C) across all seasons was significantly higher than the disturbed area (and values from all other sensors) varying between 68% in the summer and peaking in the summer at approximately 80%.

Soil temperature at 15 cm depth was significantly higher on the seismic line compared to the adjacent undisturbed area in the summer and fall by 2.6°C and 1.2°C respectively (Figure 4.28D). At 30 cm depth soil temperature was significantly higher on the seismic line in the fall, winter, and spring but the differences were not as large as the 15 cm depth (Figure 4.28E). Interestingly at 60 cm, soil temperature was significantly higher on the adjacent undisturbed area in the winter and spring by 2.2°C and 1.1°C, respectively, whereas in the summer it was significantly higher on the seismic line by 5.4°C (Figure 4.28F).

Synthesis

Considering the data in this study, winter soil-frost causes a strong decline in SWC at 15 cm for all sites (up to a 44.0% decline) due to the freezing of much of the pore water; a small decline (up to 19.0%) at 30 cm for one site, while SWC at 60 cm was not impacted. In the spring, soil-frost thaw was delayed on the seismic line by up to 6 days compared to the adjacent undisturbed area. Delayed snowmelt on seismic lines compared to their adjacent undisturbed areas has been attributed to the vegetation effect on albedo (Haag and Bliss, 1974; Dabros *et al.*, 2018). For instance, seismic lines have less vegetation on them compared to their adjacent undisturbed areas, meaning more snow can accumulate on a seismic line (as observed in this study) leading to a higher surface albedo and delayed snow melt (Haag and Bliss, 1974; Dabros *et al.*, 2018). This results in a higher overall SWC on the undisturbed area following spring melt because the snow melted faster, exceeding soil water storage and contributing to enhanced runoff. In the fall, the higher SWC on the seismic line is likely because grasses and other understory species go dormant faster and use less water compared to trees and shrubs which use water for longer periods of time leading to a moisture accumulation on the seismic line. In the summer, there is not significant difference in SWC likely because plant species both on the seismic line and the adjacent undisturbed area are transpiring at similar rates. Additionally, summer albedo is typically higher on the seismic line compared to the adjacent undisturbed area resulting in higher soil temperatures (Haag and

Bliss, 1974; Dabros *et al.*, 2018), a trend that was observed at all sites and sampling depths (with a few exceptions).

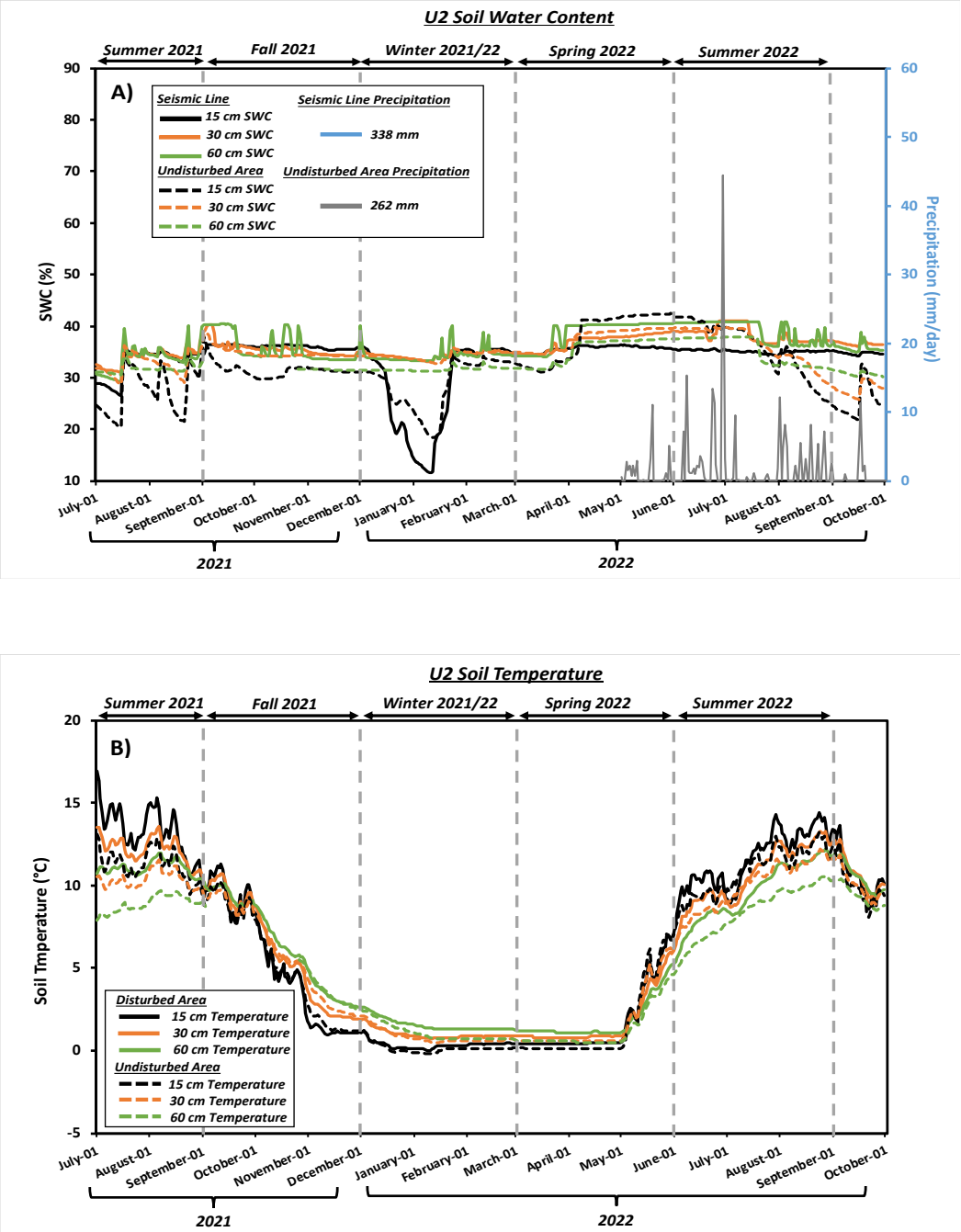

Figure 4.23: Upland Site 2 (U2) plots of A) soil-moisture and B) soil-temperature from July 2021 to October 2022. Note: Daily precipitation values for the soil-moisture plot were only available from May 2022 to October 2022.

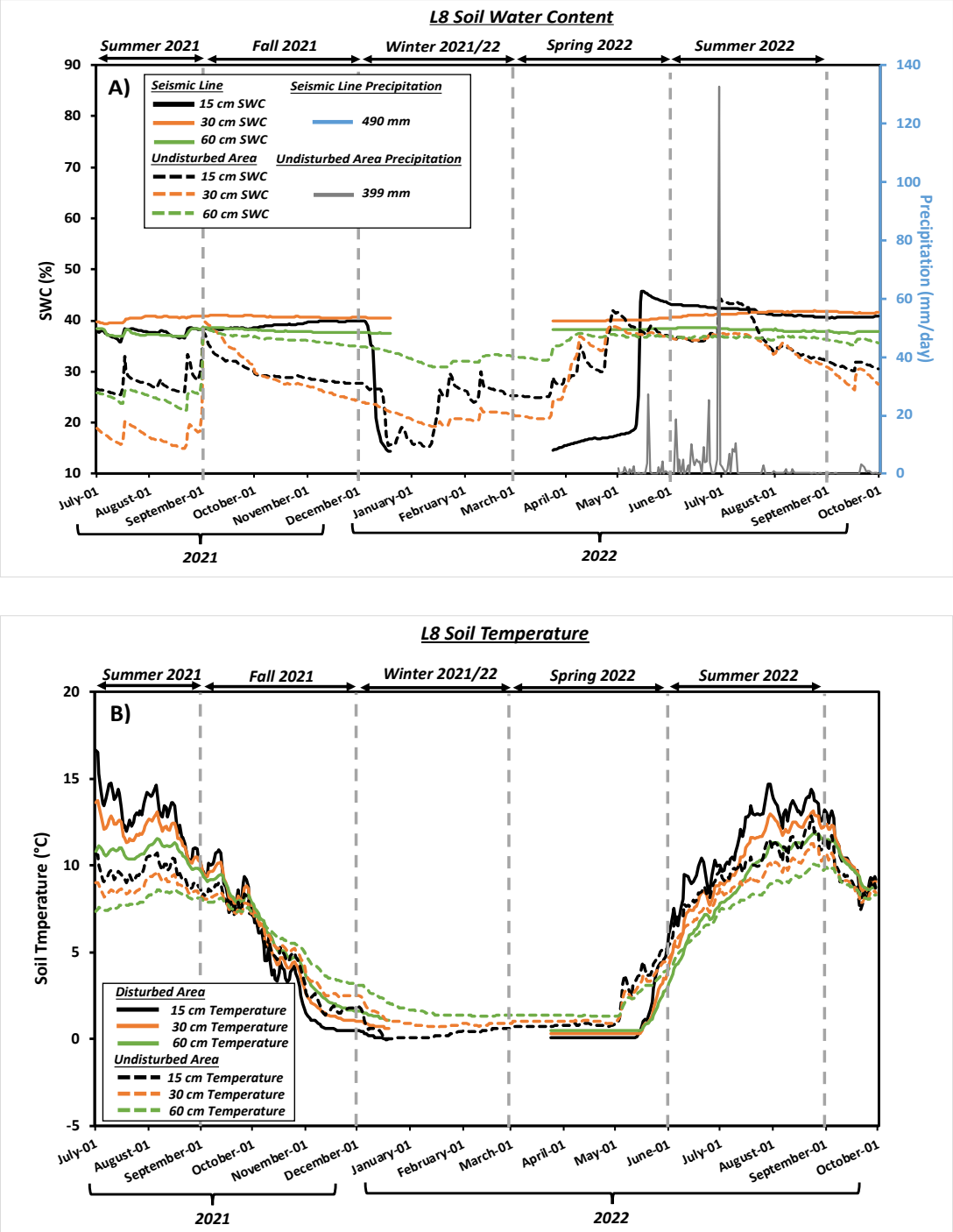

Figure 4.24: Lowland Site 8 (L8) plots of A) soil-moisture and B) soil-temperature from July 2021 to October 2022. Note: Daily precipitation values for the soil-moisture plot were only available from May 2022 to October 2022.

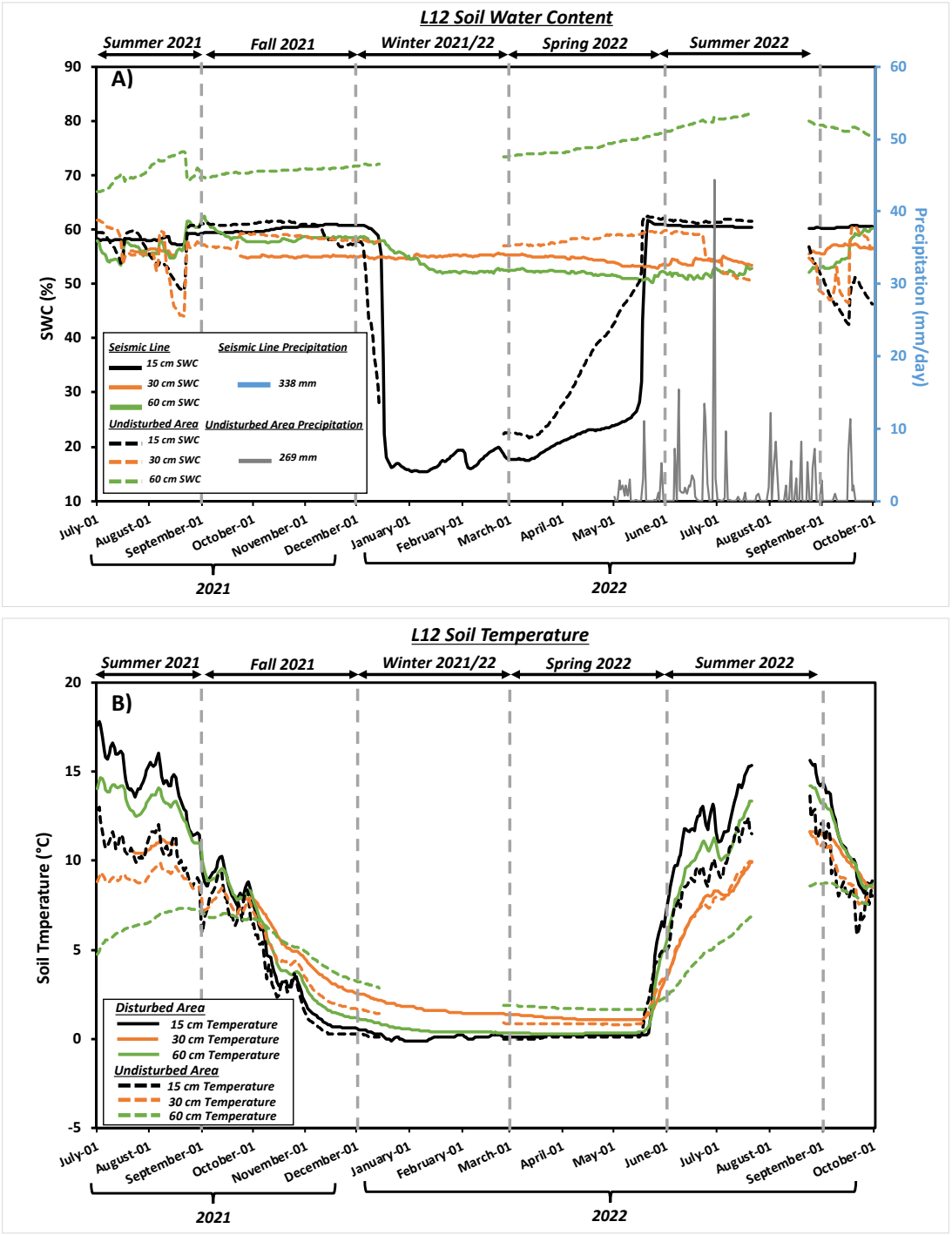

Figure 4.25: Lowland Site 12 (L12) plots of A) soil-moisture and B) soil-temperature from July 2021 to October 2022. Note: Daily precipitation values for the soil-moisture plot were only available from May 2022 to October 2022.

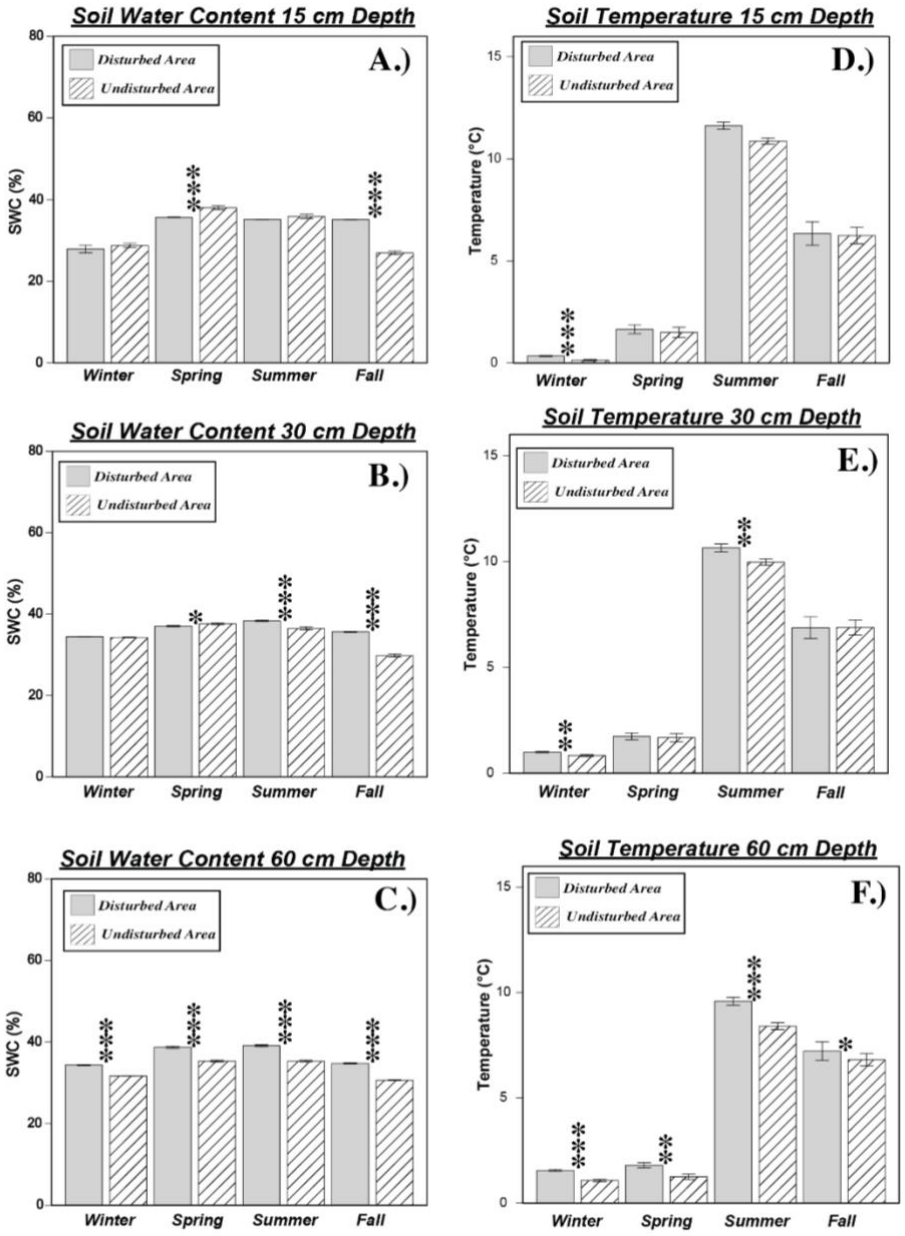

Figure 4.26: Upland site 2 (U2) bar charts of soil moisture at A) 15 cm, B) 30 cm, and C) 60 cm and soil temperature at D) 15 cm, E) 30 cm, and F) 60 cm depths in the soil-profile. Error bars represent 95% confidence intervals. A two-sample t-test was applied for differences between the seismic line and adjacent undisturbed area at each depth for each season. Levels of significance: *, **, *** correspond to $p < 0.05$, $p < 0.01$, and $p < 0.001$ respectively.

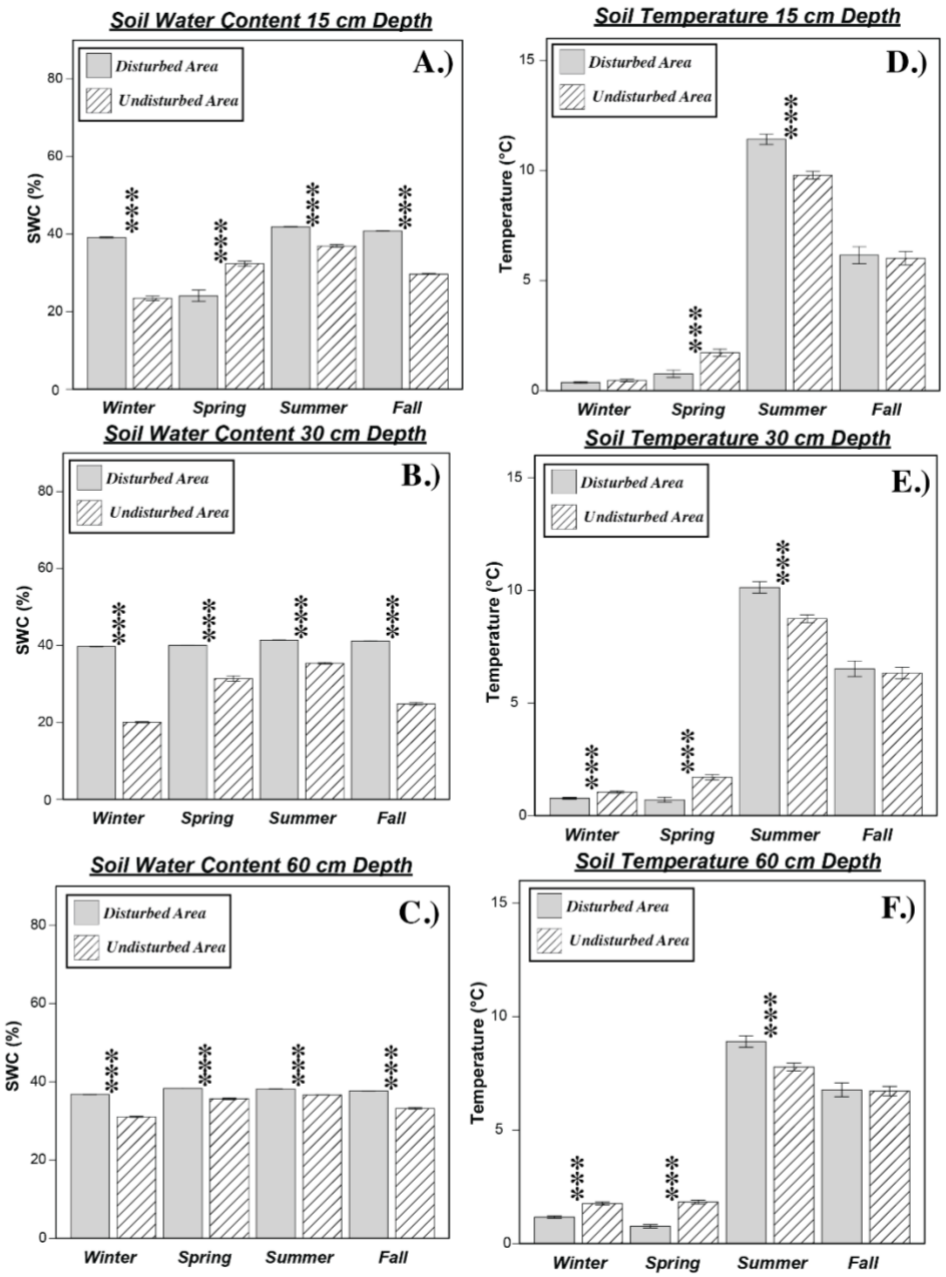

Figure 4.27: Lowland site 8 (L8) bar charts of soil moisture at A) 15 cm, B) 30 cm, and C) 60 cm and soil temperature at D) 15 cm, E) 30 cm, and F) 60 cm depths in the soil-profile. Error bars represent 95% confidence intervals. A two-sample t-test was applied for differences between the seismic line and adjacent undisturbed area at each depth for each season. Levels of significance: *, **, *** correspond to $p < 0.05$, $p < 0.01$, and $p < 0.001$ respectively.

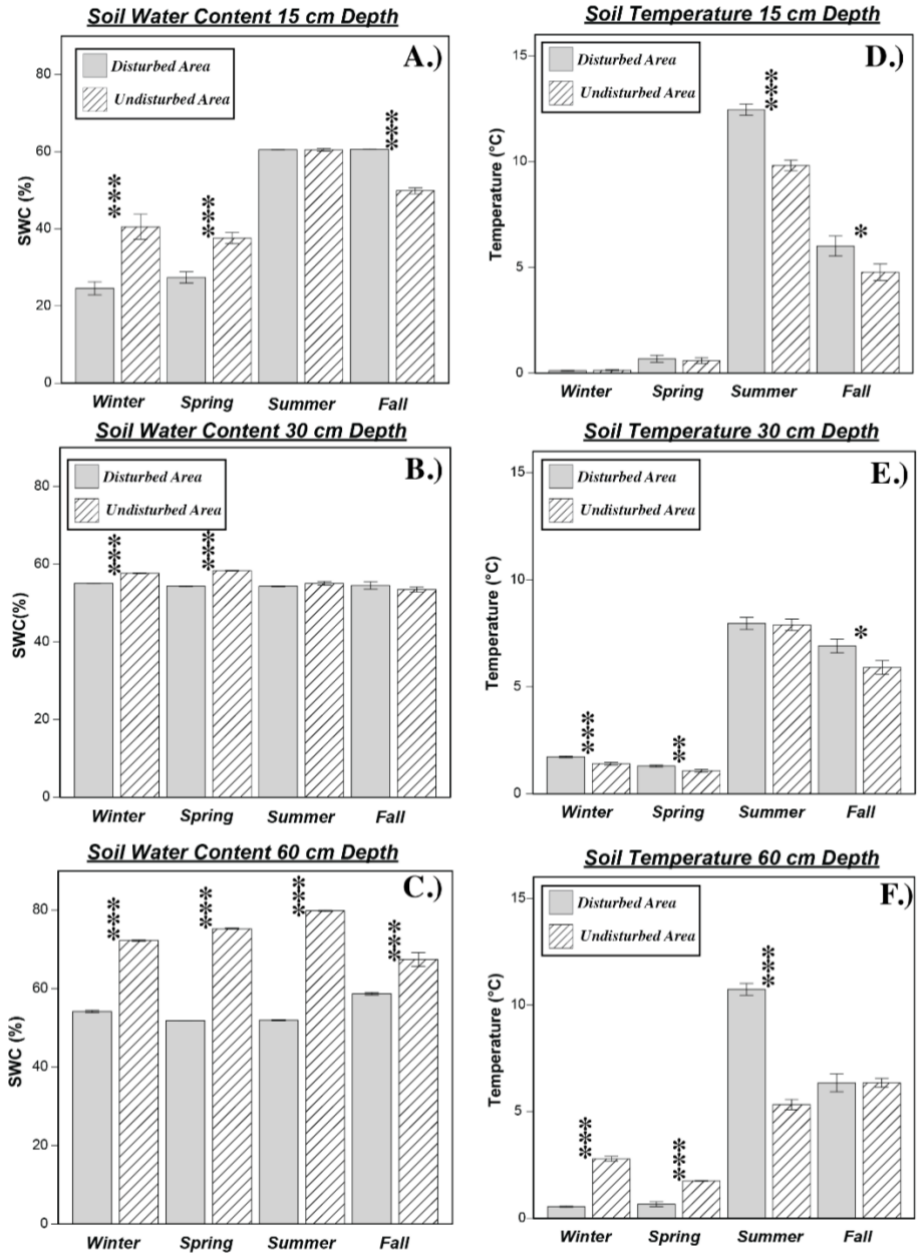

Figure 4.28: Peatland site 12 (L12) bar charts of soil moisture at A) 15 cm, B) 30 cm, and C) 60 cm and soil temperature at D) 15 cm, E) 30 cm, and F) 60 cm depths in the soil-profile. Error bars represent 95% confidence intervals. A two-sample t-test was applied for differences between the seismic line and adjacent undisturbed area at each depth for each season. Levels of significance: *, **, *** correspond to $p < 0.05$, $p < 0.01$, and $p < 0.001$ respectively.

4.7 SHAW Model Results

4.7.1 Net Solar Radiation Calibration

Net radiation was calibrated by comparing actual measured values to those simulated by the SHAW model from May 2022 to May 2023. The results for the net radiation calibration for both sites U1 and L8 are shown in Figure 4.29. ME was > 0.9 across all sites indicating the model simulates net radiation trends very well and RMSD values ranged from 0.4 W/m^2 to 1.0 W/m^2 per day for three of the locations. The model consistently under-estimates net radiation by between –12.7% and -20.7% as indicated by the PBIAS value. The PBIAS value could be further improved by manipulating LAI and plant albedo values and/or the extent of plant and residue cover; however, trials have shown that they would have to be adjusted outside a reasonable range, based on available data and our knowledge of the region (see section 3.5.2) to significantly improve the PBIAS value.

.

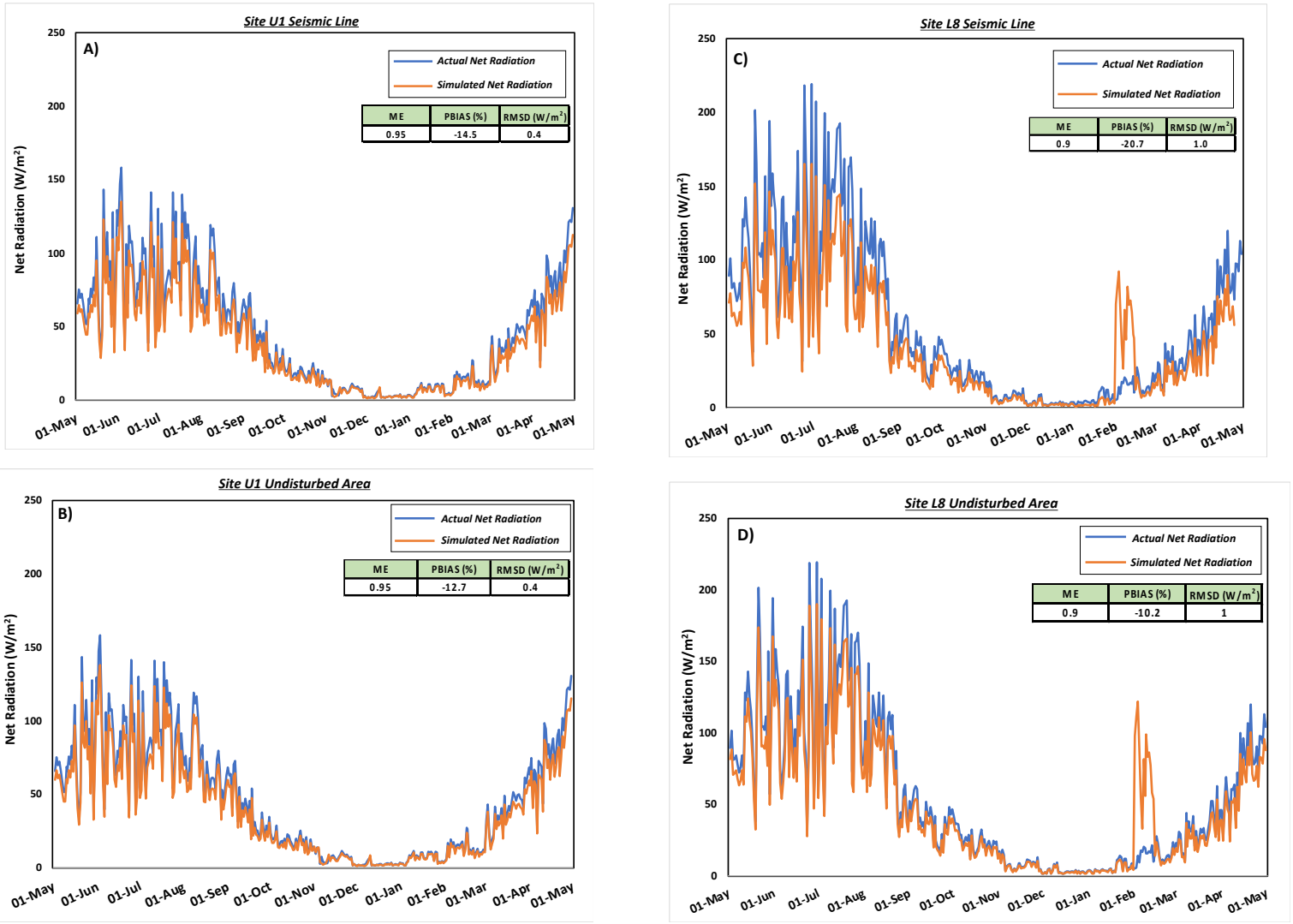

Figure 4.29: Net radiation calibration plots for A) U1 Seismic Line B) U1 Undisturbed area C) L8 Seismic Line and D) L8 Undisturbed area. Inset tables in each plot represent: ME: model efficiency, RMSD: root mean squared deviation, and PBIAS: percentage bias for each site.

4.7.2 Soil Water Content Calibration

The modeled SWC time series for all study sites are displayed in Figure 4.30. Overall, the model generally succeeds in representing SWC trends. The ME values for the simulated SWC at all depths on the seismic line for site U1 are > 0 and RMSD is < 4.4% indicating a good simulation for this site (Figure 4.30A). A good simulation was also achieved on the undisturbed area of U1 where the simulated SWC at all simulation depths had ME values > 0.26, and RMSD is < 8.9% SWC (Figure 4.30B). For the seismic line on site L8, for which variations in SWC over time are very small (nearly constant values), ME was < 0 and RMSD was < 24.4% SWC for all simulation depths. On this site, the model predicted soil-frost formation for both the 15 and 30 cm soil depths whereas soil frost was only measured at the 15 cm depth on approximately February 17th where a large drop in SWC occurred from 39.4% to 14.2% SWC (Figure 4.30C). Additionally, the model simulated two freeze-thaw cycles from November 28th to April 5th whereas only one was actually measured at the 15 cm depth. Lastly, ME values for the undisturbed area on site L8 were all > 0 with an RMSD < 5.4%, indicating an acceptable model performance (Figure 4.30D).

In the literature, trends towards both overestimation and underestimation of SWC have been reported. Preston and McBride (2004) found that the SHAW model tends to overestimate SWC particularly in the hot dry summer month and therefore underestimate ET. Hymer *et al*. (2000) found that when plant cover is present, the SHAW model underestimates SWC whereas when no plant cover is present, the SHAW model overestimates SWC. In our simulations, SWC was generally underestimated while plants are actively transpiring (from May 2022 to October 2022). However, while plants were dormant during the winter (November to April) there was no clear trend in SWC being overestimated or underestimated. Generally, the SHAW model yielded

acceptable results for SWC simulations apart from the seismic line on L8 where the measured SWC showed little variation with time, while the model simulated two episodes of significant decrease during the winter until the spring snowmelt for depths of 15 and 30cm, based on the used parameters. This could be because the recorded SWC at 15 cm and 30 cm depths for the seismic line at site L8 remained constant throughout the year suggesting limited soil frost formation, whereas the SHAW model anticipated soil frost formation at these depths during the winter.

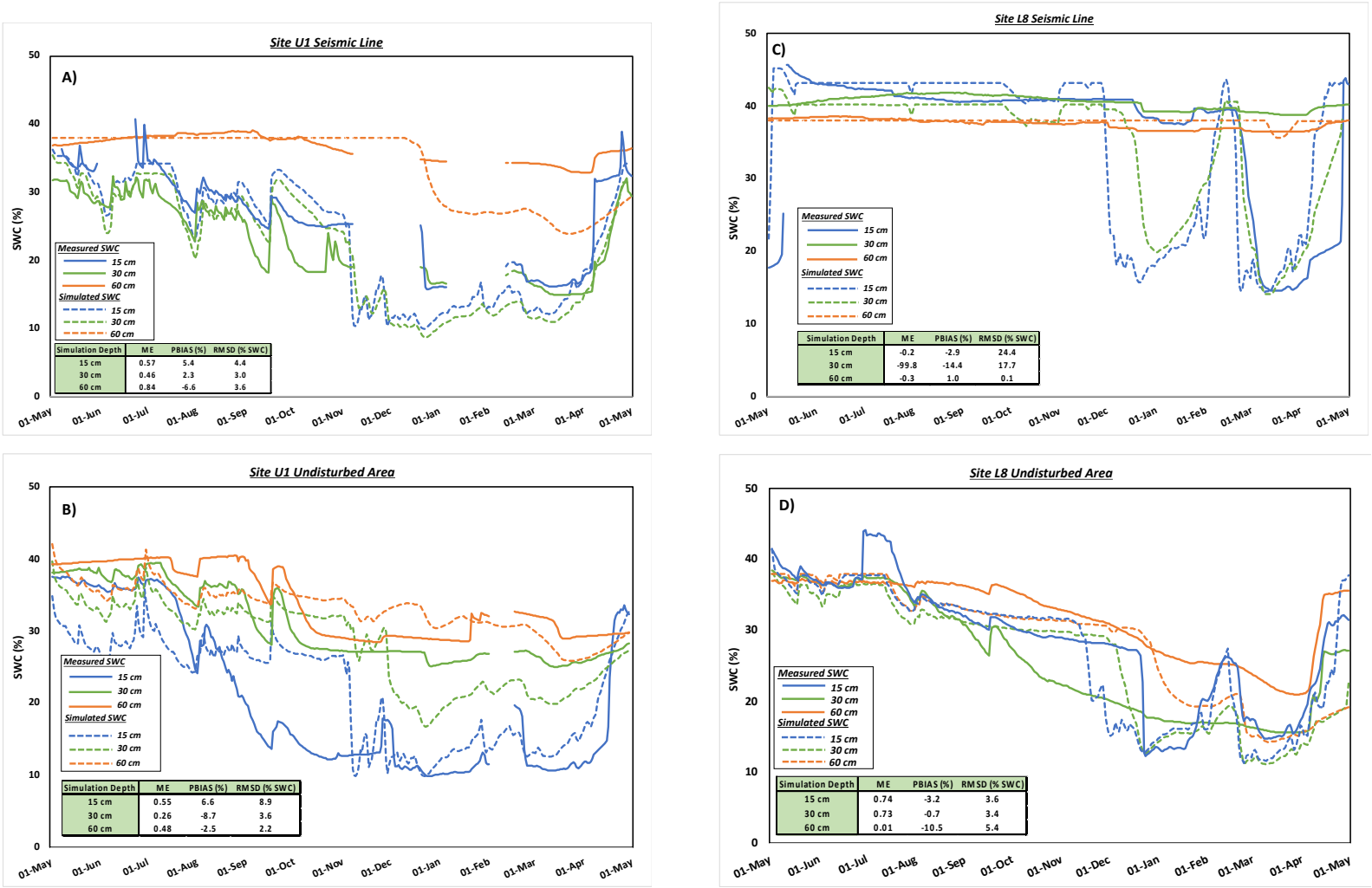

Figure 4.30: Soil moisture calibration plots for A) U1 Seismic Line, B) U1 Undisturbed area, C) L8 Seismic Line, and D) L8 Undisturbed area. Inset tables in each plot represent: ME model efficiency, RMSD: root mean squared deviation, and PBIAS: percentage bias.

After calibrating the model and assessing its performance, the SHAW model was run from May 1, 2022 to May 1, 2023 for both study sites to analyze differences in the various water budget components, which are summarized in Table 4.6 and Figure 4.33 at the end of the section.

4.7.3 Simulated Evapotranspiration

The simulated results of cumulative ET among the various study sites are summarized in Figure 4.31. Overall ET is higher on the undisturbed areas compared to the seismic lines by 40.0 mm and 225.8 mm for sites U1 and L8 respectively, with the dominant contributor being plant transpiration (apart from the seismic line on L8) (Figure 4.31). The simulated transpiration on the undisturbed areas for U1 and L8 was found to correspond to approximately 60% of total ET. Comparatively, Schlesinger and Jasechko (2014) found that, in undisturbed boreal forests, transpiration typically comprises 65% ($\pm$ 18%) of total ET, in good agreement with the SHAW simulations.

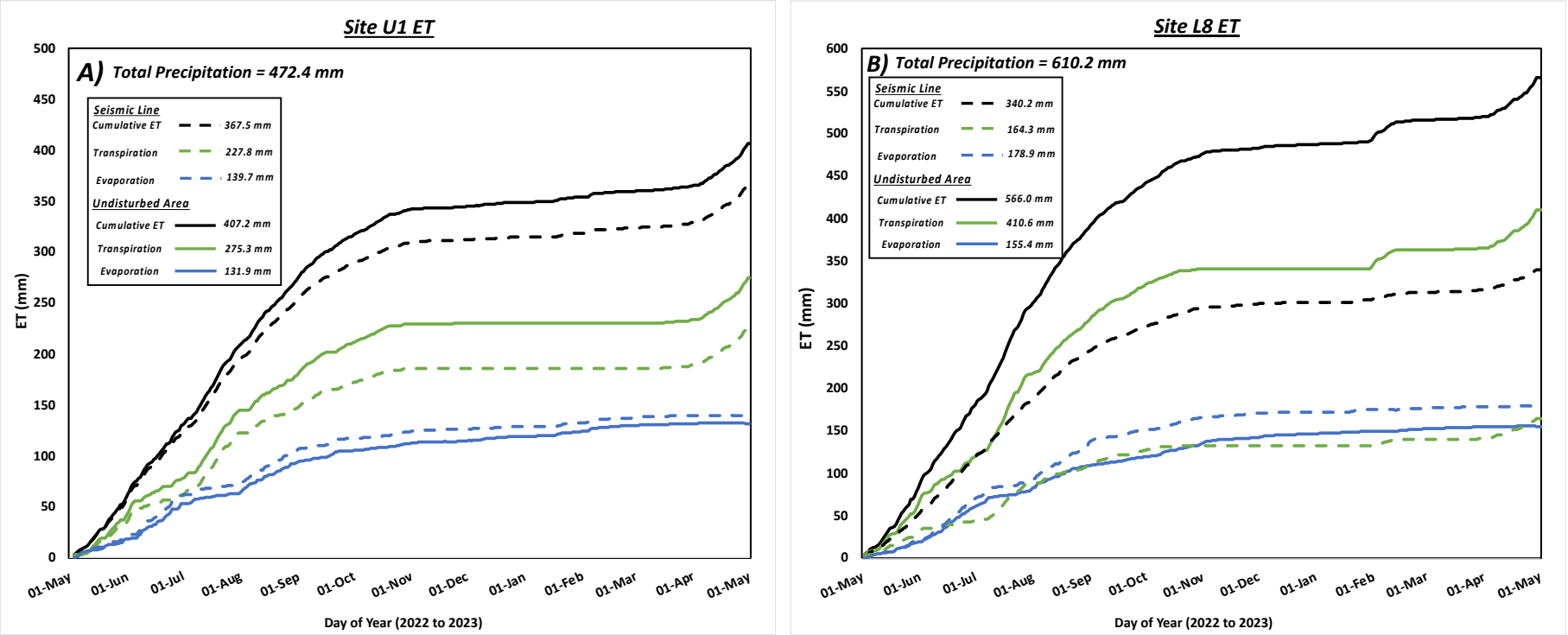

Figure 4.31: Cumulative ET plots for A) Upland Site 1 (U1) and B) Lowland Site 8 (L8) showing the contribution from transpiration and evaporation along with the total precipitation received during the simulation period.

Simulated evaporation by the SHAW model corresponds to water evaporated from the soil surface along with intercepted precipitation on the plant canopy and litter (Flerchinger 2017a) and ranged from 32 to 52% of the cumulative ET for the four locations (Figure 4.31). Correlation analysis suggests that the ET rates for these sites are highly dependent on net solar radiation and air temperature (Table 4.5), as reported other studies (e.g., Yin *et al.* 2010; Heck *et al. 2020)*. A weakly positive relationship between ET and wind speed was observed, whereas a weakly negative relationship between ET and relative humidity was observed with our datasets. The low (< 195.8 mm) simulated cumulative evaporation for the four locations is likely because evaporation rates are typically low in the boreal forest due to the cold temperatures and low precipitation amounts, which lead to the development of a plant canopy with a low LAI that resists canopy evaporation (Baldocchi *et al*. 2000). Additionally, seismic lines of the two sites are roughly east-west oriented and did not receive as much solar radiation as a southernly oriented slope would, thus potentially inhibiting evaporation further.

Table 4.5: Correlation analysis for daily weather parameters as a function of ET at the two study sites.

Parameter	U1 Seismic Line	U1 Undisturbed	L8 Seismic Line	L8 Undisturbed
Wind	0.04	0.03	0.07	0.06
Precipitation	0.03	0.03	0.14	0.07
Net Radiation	0.6	0.58	0.58	0.61
Temperature	0.52	0.53	0.54	0.52
Relative Humidity	-0.15	-0.15	-0.1	-0.16

At the four locations, the average ET rates were highest during July, which was also the month corresponding to the highest average net solar radiation and temperature (Figures 4.14 and 4.16). The average ET rates during July for the seismic line and undisturbed area for site U1

(upland) were 2.4 mm/day and 2.6 mm/day respectively (a difference of ~13%), whereas on the seismic line and undisturbed area for site L8 (lowland), the average ET rates were 2.3 mm/day and 3.0 mm/day respectively. This can be attributed to the higher LAI on the undisturbed area for both sites (Table 3.5) and/or the weather data used for the undisturbed area on site L8 (see section 2.2). The simulated average daily ET rates are similar to those measured in many studies carried out within the Canadian Boreal Forest during the growing season (e.g., Blanken *et al*. 2001; Amiro *et al*. 2006; Pejam *et al*. 2006). In the boreal plains, ET rates for deciduous stands (i.e., aspen) are up to 6 mm/day, whereas for conifer stands (i.e., black spruce) they are up to 2 – 3 mm/day (Baldocchi *et al*. 2000; Ireson *et al*. 2015). The difference in ET among deciduous stands and conifer stands has been attributed to the higher growing season LAI of the deciduous stands (the same as site U1 in this study), but also varies with available soil water capacity (Ireson *et al*. 2015). Considering this, the simulated ET rates at site L8 (primarily black spruce) and U1 (primarily balsam poplar) are near previously reported values.

The dryness index ratios (PET:P) for the seismic line and undisturbed area for site U1 based on the SHAW simulations are 0.8 (a slightly wet environment) and 1.0 (P ~ ET) respectively (Figure 4.31), which are near previously reported values in the boreal forest. For instance, long-term (25 year) studies of aspen and mixed-wood dominated upland areas within the BP indicate a median annual total precipitation of 478 – 500 mm and ET of 459 – 470 mm rendering a dryness index greater than 1 and characterising an overall moisture-deficit (Devito *et al*. 2012). As mentioned in section 1.2.3, Smerdon *et al.* (2019) used long-term (1989-2010) climate-normal values from ClimateNA gridded data (Wang *et al*., 2016) to estimate an average P of 595 mm/year and reference ET of 525 mm/year for the Town of Fox Creek, yielding a slight water surplus (70 mm/year) and a dryness index of 0.9. Guarin-Martinez (2022) also found a

value of 495 mm/year for the potential ET across the 700 km^2 watershed using the Thornthwaite method on a monthly basis and a gap-filled data series based on different weather stations located within and near the study area. This PET value corresponds to 90% of the 552 mm/year of annual precipitation of this dataset. This author also found that water surplus (that can be regarded as potential recharge) can vary spatially and temporally between 0 and 57 mm/year. Using eddy covariance techniques and an 8-year dataset, Zha *et al.* (2010) modelled an annual ET of 405 $\pm$ 84 mm for an aspen forest on a hummocky glacial moraine clayey soil with a high moisture retention, which seems relatively similar to our study area. Considering this, the simulated ET on the undisturbed area of site U1 falls within the standard deviation of the results from Zha *et al.,* (2010) and ET values from the different areas are generally in agreement with previous studies.

The dryness index for the seismic line and undisturbed area for study site L8 was 0.6 and 0.8 respectively, indicating a wet environment on the seismic line and slightly drier environment for the adjacent undisturbed area (Figure 4.31). This agrees with typical dryness index values from wetland regions with non-standing water, as is the case for site L8, which typically yields a dryness index ratio of 0.7 to 1.0 according to Devito *et al.* (2012). Long-term studies on peatland-swamp complexes with varying scales (50 to 5000 km^2) across the BP region within Alberta suggest these areas receive a mean annual total precipitation of 440 - 462 mm and have ET values of 321 – 395 mm (Devito et al. 2017). For a similar study site, Zha *et al.* (2010) had obtained an ET value of 374 $\pm$ 34 mm for a black spruce forest on a poorly drained sandy clay soil with a near-surface water table in the boreal plains near Prince Albert, Saskatchewan. However, this was not the case for site L8, which received 603.4 mm of precipitation over the studied period, well above the historical mean for the study region. Simulated ET on the seismic

line of site L8 was 355.3 mm which is near those reported in the previous studies mentioned above. Conversely, ET was 472.1 mm on the adjacent undisturbed area, representing ~ 90%, in agreement with Devito *et al.* (2017) and Zha *et al.* (2010).

A comprehensive literature review (78 studies from different countries) of western coniferous forests by Goeking and Tarboton (2020) found that forest cover loss does not always result in a decreased ET. Stand replacing disturbances (e.g. clear-cut forest harvesting, large wildfires) typically result in a net ET reduction, whereas non-stand replacing disturbances (e.g. smaller wildfires, insect attacks, drought, partial forest harvesting) may result in a net ET increase (Goeking and Tarboton 2020). The net increase occurs because (i) competitive plant species may rapidly colonize the impacted area resulting in an understory plant canopy with a high LAI and transpiration rates may offset the overstory ET losses and (ii) higher understory radiation resulting in increased evaporation (Goeking and Tarboton, 2020). For instance, using eddy covariance methods in boreal regions impacted both by mountain pine beetle attacks and partial forest clearing, Brown *et al.* (2014) found no net change in ET, while discovered a reduction of up to 62% in cumulative ET. However, in the current study, an overall reduction in ET was observed on the seismic line of sites U1 and L8 by 94.2 mm and 116.8 mm respectively. The smaller ET difference (40.0 mm) between the seismic line and the adjacent undisturbed area for site U1 compared to site L8 may be due to the greater degree of vegetative recovery and a high understory contribution to ET for U1. This is also supported by the LAI measurements (Table 3.5) which are higher by ~ 1.5 units when compared to the lowland site L8.

4.7.4 Simulated Runoff and Percolation

The SHAW model simulates deep percolation as the movement of water between the two deepest soil simulation nodes, which in this case corresponds to water flux between 0.3 and 0.6 m, therefore mostly below the root zone. Positive deep percolation values indicate downward water movement between the two deepest soil simulation nodes whereas negative values indicate upward water movement. For sites U1 and L8, no "deep" percolation was simulated on the seismic line, whereas 47.8 mm and 21.5 mm of deep percolation was simulated in the adjacent undisturbed area for sites U1 and L8 respectively (Table 4.10). The deep percolation estimates by the SHAW model for both sites are in agreement with the recharge range (0 - 70 mm/year) suggested by Guarin-Martinez (2022) for the study area.

Runoff was simulated at 57.6 mm and 3.8 mm for the seismic line and undisturbed area respectively at site U1. The enhanced runoff on the seismic lines can be attributed (i) to the higher bulk density (by 0.3 g/cm^3) of the upper soil layer on the seismic line compared to the adjacent undisturbed area (Figure 4.2), and/or more likely (ii) to less interception by plants (particularly tall trees on the seismic line), which would promote surface runoff and/or ponding. Generally, upland regions within the BP have some of the lowest annual runoff rates (20 – 30 mm) (Devito *et al*. 2017). This is because upland regions within the BP have a large water demand emplaced by the plant canopy and a high soil storage capacity because of the thick glacial deposits, thus acting as an overall water sink region (Devito *et al*. 2012). The interaction of the plant canopy and the forest floor in upland regions means that most precipitation is intercepted by vegetation and only large precipitation events (i.e. > 20 mm) are likely to infiltrate into the soil and possibly promote runoff and/or possible groundwater recharge (Devito *et al*. 2012). This pattern was observed in the SHAW simulation for site U1 as the majority of runoff

on the seismic line occurred (i) on June 29 - 30 following a large (54.9 mm) rainfall event, which accounted for 46.5 mm of runoff, and (ii) following the simulated spring-melt in May, which accounted for 4.5 mm of runoff. At the end of the model simulation (May 1st), 23.8 mm of snow was left on the seismic line of site U1, indicating that more runoff is likely to occur.

Cumulative change in soil-water storage for the undisturbed area of site U1 was -72.5 mm, indicating that most of the water is lost likely via plant transpiration and evaporation (Figure 4.32). Conversely, change in soil-water storage on the seismic line was much lower (-1.8 mm), likely attributed to less vegetative demand for soil-water. As a general rule, larger soil grain-size and surface topography in upland BP regions may reduce the suction effect of the unsaturated zone, allowing free drainage within the soils and making soil-water storage and vertical recharge important in upland regions, as surface flow (runoff) is limited to anomalous excess moisture events (Devito *et al*. 2012). This was observed, to some extent, in this simulation. On the other hand, finer textured soils limit infiltration and thereby, aquifer recharge.

.

The SHAW simulation for site L8 resulted in a cumulative change in soil-water storage on the seismic line of –7.5 mm, indicating a slight decrease in SWC over the 12-month period, whereas –126.0 mm was simulated on the undisturbed area (Figure 4.32), likely due to the enhanced ET at this site. Additionally, the simulation for site L8 resulted in no deep percolation on the seismic line and 21.5 mm occurred on the adjacent undisturbed area (Table 4.6). Deep percolation estimates were low at site L8 because runoff estimates were high: 240.7 mm for the seismic line and 247.6 mm for the adjacent undisturbed area for site L8 (Table 4.6). This is because from June 29 - 30 the weather station measured an extreme rainfall event at 146.2 mm that accounted for 140.3 mm of the annual simulated runoff.

Comparing to other studies in the BP (Devito *et al*. 2012, 2017; Barr *et al*. 2012), the simulated runoff amounts for the lowland study site L8 are reasonable. For instance, long-term median annual runoff amounts (60 to 119 mm) within BP peatlands and swamps are some of the highest in the BP (Devito *et al*. 2017). However, runoff is highly variable. A local scale study on an old undisturbed jack pine site yielded an annual runoff amount of 187 +/- 55 mm (Barr *et al*. 2012). In her study using a monthly water budget, Guarin-Martinez (2022) had found that runoff varied between 0 and 151 mm/year over the whole 700 km^2 study area, allowing her to conclude that recharge likely ranged between 0 and 70 mm/year depending on the year.

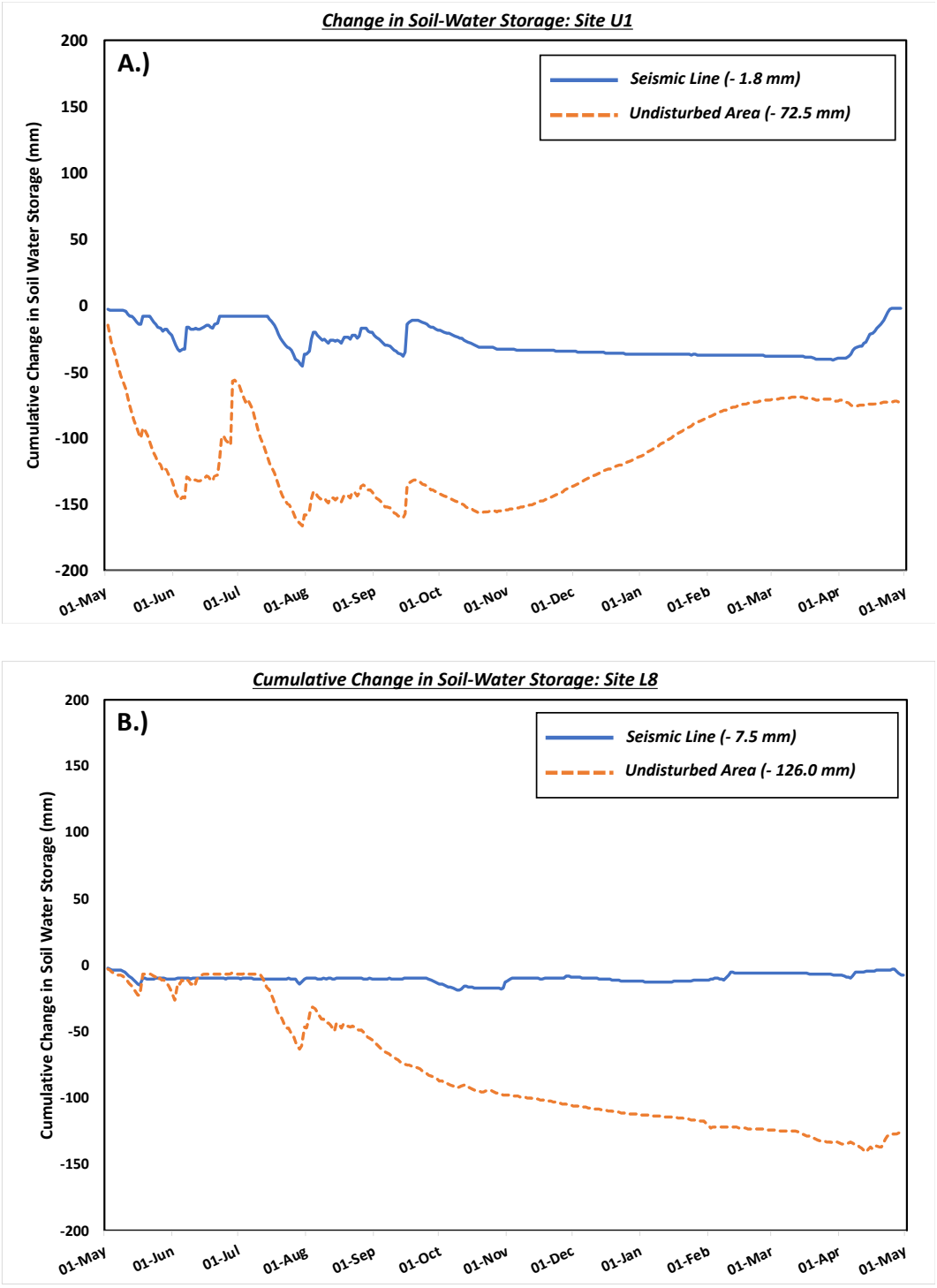

Figure 4.32: Cumulative change in soil water storage plots for A) Upland Site 1 (U1) and B) Lowland Site 8 (L8).

Table 4.6: Simulated water budget values for all study sites from May 1, 2022, to May 1, 2023.

Site	Precipitation	Runoff	ET	Deep Percolation*	Change In Storage**				Cumulative Simulation Error (mm)***
					Soil	Snow	Residue	Canopy	
U1 Seismic Line	472.4	57.6	380.4	0.0	-1.8	23.8	0.35	-0.6	-6.9 (-1.5 %)
U1 Undisturbed	472.4	3.8	414.4	47.8	-72.5	59.2	0	0.4	-0.7 (-0.2 %)
L8 Seismic Line	610.2	240.7	355.3	0.0	-7.5	0	0	-1.13	-14.9 (-2.4 %)
L8 Undisturbed	610.2	247.6	472.11	21.5	-126.0	0	0.19	-1.19	-7.8 (-1.3 %)

* Deep percolation corresponds to the water flux between the two deepest soil nodes (30 and 60 cm in this study).

** The change in storage term is comprised of soil storage (negative values indicate soil water was used up, whereas positive values indicate soil water was gained), the amount of water remaining as snow, water on the plant residue plant canopy at the end of the simulation.

***A negative simulation error value indicates an underestimation of the cumulative water balance by the model. In parenthesis is the percentage error determined from the cumulative simulation error divided by the total precipitation the area received.

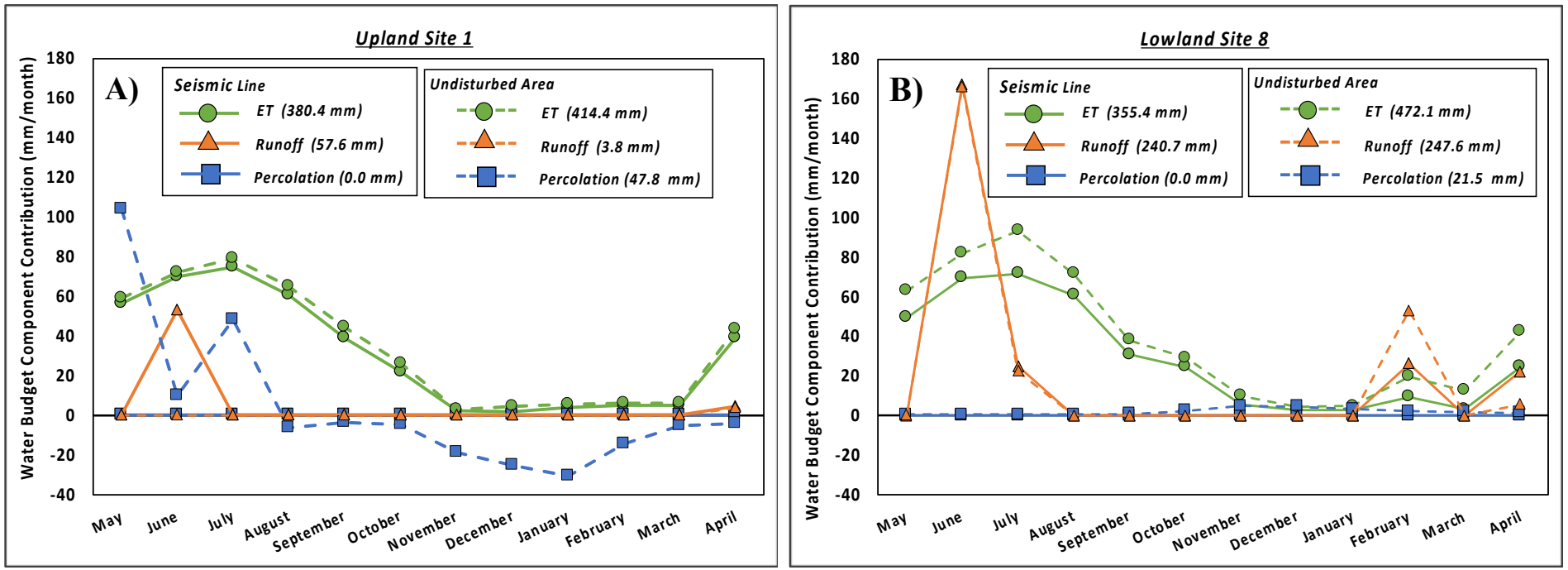

Figure 4.33: Main water budget components (ET, Runoff, and Deep Percolation) simulated by the SHAW model for A) U1 and B) L8. Positive deep percolation values indicate downward water movement between the two deepest soil simulation nodes (0.3 and 0.6 m in this study) whereas negative values indicate upward water movement.

Chapter 5 Conclusion and Future Work

5.1 Conclusion

This study investigated the impacts of seismic lines on the eco-hydrological functioning of the landscape and physio-chemical properties of the vadose zone for a 700 km^2 watershed near the Fox Creek area, in west-central Alberta. This study is a component of a broader project led by the Geological Survey of Canada aimed at evaluating cumulative impacts associated with activities from the oil and gas industry. In this master's thesis, I investigated the effects of seismic exploration lines on: (1) soil water content (SWC) within the watershed, (2) the hydrological cycle using the Simultaneous Heat and Water (SHAW) model, a physically based 1-D model, and (3) the physio-chemical properties of the vadose zone, utilizing data from both the solid and aqueous phases of the soil.

Over a period of 1.5 years, hourly SWC measurements from depths of 15 cm, 30 cm, and 60 cm revealed that most seasonal variations primarily occurred within shallower soil layers (15 cm and 30 cm). A consistent pattern observed for upland and lowland ecosites (apart from a peatland site L12 with a near-surface water table) was as follows: (1) during the fall season, SWC measured at the 15 cm depth was significantly higher on the seismic lines (up to 8.1% SWC). This was be attributed to the earlier dormancy and thus reduced water usage of graminoids and herbaceous understory species, which are the dominant vegetation communities on seismic lines. This contrasts with the adjacent undisturbed areas which are dominated by trees and shrubs that go dormant much later than understory species. (2) In early spring, SWC was significantly higher on the adjacent undisturbed area (up to 3.0% SWC), likely due to delayed snowmelt on seismic lines. No consistent variations in SWC were observed during the winter and summer seasons among the sites, and variations in SWC at greater depths (30 cm and 60 cm) between the seismic lines and adjacent undisturbed areas

become less apparent. These findings contradict the common assumption that seismic lines consistently exhibit a higher soil moisture content over the growing season.

Using the SHAW model, four simulations (two on a seismic line and two on the adjacent undisturbed areas for one upland and one lowland ecosite) were conducted for the May 2022 – May 2023 period (12 months) to estimate the water balance for a 60 cm soil profile. The model was calibrated for net radiation and SWC by comparing site measured values with the simulated values. The net radiation calibration demonstrated satisfactory results across all sites, with a model efficiency (ME) value greater than 0.9 and a root mean square deviation (RMSD) less than 1.0 W/m^2. Similarly, the calibration for SWC was deemed acceptable, as ME was always greater than 0.01 and RMSD was less than 9.0% SWC for all sites except for the seismic line on a lowland site (L8). For the latter, where measured SWC remained relatively constant over time for the 15 and 30 cm depths, the model could not accurately simulate SWC variations, resulting in an ME less than 0 and RMSD less than 24.4% SWC. This was likely because the measured SWC at depths of 15 cm and 30 cm along the seismic line at site L8 were relatively constant throughout the year indicating minimal soil frost formation, whereas the SHAW model anticipated soil frost formation at these depths during the winter.

Using the calibrated models, annual water budgets were simulated on a monthly basis for each site. Simulated evapotranspiration (ET) was consistently higher on the undisturbed areas compared to the seismic lines, with differences up to 117 mm/year. These differences in modelled ET were primarily attributed to the presence of denser vegetation on the undisturbed areas, leading to greater ET. The increase in ET on undisturbed areas resulted in a larger annual soil water deficit (up to 118 mm), whereas on seismic lines soil water deficit was much smaller (from 1.8 to 7.5 mm). Deep percolation (percolation between 30 to 60 cm depth) ranged from 0 to 47.8 mm/year, which falls within previous estimates of recharge within the watershed (0 – 70 mm/year, Guarin-Martinez, (2022)). Runoff estimates range from 3.8 to

240.7 mm/year across the four locations. At the lowland site L8, the seismic line and undisturbed area had high annual runoff estimates (240.7 mm and 247.6 mm, respectively) due to an anomalously high precipitation event measured by the weather station within one day. In contrast, for the upland sites, runoff was very low, 57.6 mm on the seismic line and 3.8 mm on the undisturbed area, also representing runoff values consistent with those previously estimated for the study region (Guarin-Martinez, 2022). Precipitation data indicate that seismic lines can receive up to 126 mm more annual precipitation compared to the adjacent undisturbed areas. However, this maximum difference is due to a single precipitation event. Excluding this anomaly, annual precipitation would be 49.1 mm higher based on our dataset. Soil-water in the study area, sampled from depths of 30 cm, 60 cm, and 120 cm using suction lysimeters, is predominantly of the $CaHCO_3$ type indicating relatively young and minimally chemically evolved water that is strongly influenced by near-surface exchange processes occurring at the interfaces of clay minerals and organic matter. This water type is also found in the underlying bedrock aquifer, particularly in its shallow and upstream parts, while the central and deeper (confined) parts of the aquifer contain more of the $NaHCO_3$ type water corresponds to somewhat more chemically evolved groundwater. The measured $\delta^{18}O$ and $\delta^{2}H$ isotopic signatures of soil-water samples (n=154) in this study indicate water of meteoric origin that has undergone minimal evaporation as they align with the LMWL: $\delta^{2}H$ (‰) = 7.44 $\delta^{18}O$ (‰) – 6.80 (n = 39 and R^2 = 0.99). Shallow soil-water samples (30 and 60 cm) show more seasonal variations in $\delta^{18}O$ and $\delta^{2}H$ values, whereas deep soil waters (120 cm) resemble the shallow groundwater (~ 25-30 m) in the study region, which is primarily recharged by local infiltration of meteoric water.

Soil solids had a bulk density ranging from 0.1 to 1.7 g/cm^3 with higher (by 8 to 65%) values observed in the upper 15 cm of the soil profile on the seismic lines compared to the adjacent undisturbed areas. However, the measured bulk-density values were within the range of typical mineral soils (1.0 to 1.8 g/cm^3) and thus not considered significantly compacted.

The soil was acidic with a mean pH of 4.9 (n = 30) and soil samples from seismic lines had a lower cation-exchange capacity (CEC) and higher concentrations of base ions (e.g., Ca^{2+}, Mg^{2+}, HCO_3^-) in the soil solution compared to undisturbed areas. The lower CEC on seismic lines indicates a poor buffering capacity of the soil, increasing its vulnerability to acidification and potential trace metal contamination.

5.2 Future Work and Recommendations

The simulations using the SHAW model in this study could be improved from direct measurements of a few additional soil hydraulic parameters (e.g., saturated water content, air entry potential, pore size index, etc.) and plant parameters (rooting depth and plant biomass), rather than relying on empirical equations and literature derived values. Moreover, considering that the lower boundary of the model was limited to 60 cm, a deeper soil profile might be necessary to estimate recharge, especially for the upland sites. To validate the model estimates of ET, separate measurements obtained through eddy covariance techniques or chamber gas flux measurements could be used. Given that the SHAW model represents a vertical 1-D profile, future modelling efforts could explore the effects of water cycling in two and three dimensions with an eco-hydrological model taking into account atmospheric fluxes and freeze-thaw periods, to potentially represent and capture flow in the study region more realistically. Manual calibration of the model through trial-and-error is time consuming and subject to bias, potentially affecting the accuracy of the results due to parameter interactions. A recommended approach for future studies using the SHAW model is to implement an automated multi-objective parameter optimization algorithm, such as AMALGAM (A Multi-ALgorithim, Genetically Adaptive Multi-Objective) developed by Vrugt and Robinson (2007). This approach allows for comprehensive evaluation of realistic parameter optimizing the objective function and yielding more reliable results (Flerchinger *et al.*, 2012). Lastly, the model should ideally be validated with data from multiple years to ensure its robustness and applicability beyond a single-year dataset.

Considering that all seismic lines studied in this paper were > 6 m wide), it would be beneficial to conduct a similar study on low-impact seismic lines, which are narrower (< 4 m wide) but exist at higher density in these landscapes (Dabros *et al*. 2018). Additionally, continuous monitoring of the vadose zone on seismic lines would be valuable to assess the long-term variations in water cycling and changes in soil properties. For instance, a future study could measure annual litterfall inputs on seismic lines and the adjacent undisturbed areas to estimate soil carbon contribution from litter fall and organic matter cycling. This could then be coupled with soil geochemical data to estimate soil weathering rates on seismic lines compared to undisturbed areas to better understand long-term consequences. While site-level monitoring is a valuable starting point for assessing the impacts of seismic lines on water cycling in the vadose zone, it would be important and beneficial to complement it with remote sensing and spatial (2D or 3D) modelling techniques. By considering the density and width of seismic lines in a region, these approaches would allow for a more comprehensive understanding of the broader landscape effects.

Overall, this study reveals that areas impacted by seismic exploration lines show profound differences in their hydrology and the physio-chemical properties of their vadose zones compared to undisturbed areas. Considering that 35% of the study area has experienced disturbances in the form of forest cuts (Le *et al.* 2023), the impacts of seismic lines on the hydrology and vadose zone of a landscape cannot be ignored. This becomes especially significant given that there is no reclamation requirement for seismic lines and that anthropogenic disturbances in general are expected to increase in western Canada (Dabros *et al.* 2018). On a larger scale the IPCC (2023) revealed that the vast amount of human disturbances in North America over the last two decades has led to a general upward trend in mean and extreme temperatures. Northern ecosystems in particular are experiencing accelerated warming compared to other terrestrial biomes (IPCC, 2023) making the sustainable management of water resources in these areas crucial. Considering that boreal

ecosystems host one third of the global carbon stock in its biomass and soil (IPCC 2007; Pan *et al.* 2011) and act as a net sink for atmospheric CO_2, human-induced climate change poses a serious threat to converting certain boreal regions into net CO_2 sources in the near future (Kurz *et al.* 2013). On a larger scale, the IPCC (2023) revealed that the large amount of anthropogenic disturbance in North America over the past two decades has led to a general upward trend in mean and extreme temperatures. Further studies aimed at determining the impacts of anthropogenic disturbances at the land surface, including seismic lines, on the hydrology and biology of boreal forests are critical to developing an understanding of changes in carbon dynamics that will occur due to climate change.

References

ABMI (2010) ABMI Wall-to-wall Land Cover Map 2010 Version 1.0

ABMI HFI (HFI) (2019) Wall-to-Wall Human Footprint Inventory Alberta. Alberta Biodiversity Monitoring Institute and Alberta Human Footprint Monitoring Program, Edmonton, AB

ACIS (2022) Alberta Agriculture, Forestry, and Rural Economic Development, Alberta Climate Information Service (ACIS). https://acis.alberta.ca. Accessed 12 Jul 2022

Alberta Wilderness Association (2017) Little Smoky. In: Alberta Wilderness Association. https://albertawilderness.ca/issues/wildlands/areas-of-concern/little-smoky/. Accessed 5 Oct 2021

Alessi DS, Zolfaghari A, Kletke S, et al (2017) Comparative analysis of hydraulic fracturing wastewater practices in unconventional shale development: Water sourcing, treatment and disposal practices. Canadian Water Resources Journal / Revue canadienne des ressources hydriques 42:105–121. https://doi.org/10.1080/07011784.2016.1238782

Allison GB, Barnes CJ, Hughes MW (1983) The Distribution of Deuterium and 18O in Dry Soils 2. Experimental. Journal of Hydrology 64:377–397

Allison SD, Treseder KK (2011) Climate change feedbacks to microbial decomposition in boreal soils. Fungal Ecology 4:362–374. https://doi.org/10.1016/j.funeco.2011.01.003

Amiro B, Barr A, Black T, et al (2006) Carbon, energy and water fluxes at mature and disturbed forest sites, Saskatchewan, Canada. Agricultural and Forest Meteorology 136:237–251. https://doi.org/10.1016/j.agrformet.2004.11.012

Amundson R, Richter DD, Humphreys GS, et al (2007) Coupling between Biota and Earth Materials in the Critical Zone. Elements 3:327–332. https://doi.org/10.2113/gselements.3.5.327

Arthur MA, Fahey TJ (1993) Controls on Soil Solution Chemistry in a Subalpine Forest in North-Central Colorado. Soil Science Society of America Journal 57:1122–1130. https://doi.org/10.2136/sssaj1993.03615995005700040040x

Atkinson LA, Hartman GMD (2017) AER/AGS Report 93: 3D Rendering of the Regional Stratigraphy of Paleogene−Quaternary Sediments in West-Central Alberta. Alberta Energy Regulator/Alberta Geological Survey Report 93:51

AWWA (2) 2320 Alkalinity. Standard Methods for the Examination of Water and Wastewater 4. https://doi.org/10.2105/SMWW.2882.023

Baldocchi D, Kelliher FM, Black TA, Jarvis P (2000) Climate and vegetation controls on boreal zone energy exchange. Global Change Biology 6:69–83. https://doi.org/10.1046/j.1365-2486.2000.06014.x

Barr AG, van der Kamp G, Black TA, et al (2012) Energy balance closure at the BERMS flux towers in relation to the water balance of the White Gull Creek watershed 1999–2009. Agricultural and Forest Meteorology 153:3–13. https://doi.org/10.1016/j.agrformet.2011.05.017

Beaudoin-Galaise M, Jutras S (2022) Comparison of manual snow water equivalent (SWE) measurements: seeking the reference for a true SWE value in a boreal biome. The Cryosphere 16:3199–3214. https://doi.org/10.5194/tc-16-3199-2022

Beckingham JD, Archibald JH (1996) Field Guide to Ecosites of Northern Alberta. Northern Forestry Center

Berner EK, Berner RA, Moulton KL (2003) 5.06 - Plants and Mineral Weathering: Present and Past. Treatise on Geochemistry: Pergamon. https://doi.org/10.1016/B0-08-043751-6/05175-6

Betts AK, Ball JH (1997) Albedo over the boreal forest. J Geophys Res 102:28901–28909. https://doi.org/10.1029/96JD03876

Bjorkman AD, Elmendorf SC, Beamish AL, et al (2015) Contrasting effects of warming and increased snowfall on Arctic tundra plant phenology over the past two decades. Glob Change Biol 21:4651–4661. https://doi.org/10.1111/gcb.13051

Blanken PD, Black TA, Neumann HH, et al (2001) The seasonal water and energy exchange above and within a boreal aspen forest. Journal of Hydrology 245:118–136. https://doi.org/10.1016/S0022-1694(01)00343-2

Bliss LC, Wein RW (1972) Plant community responses to disturbances in the western Canadian Arctic. Can J Bot 50:1097–1109. https://doi.org/10.1139/b72-136

Blott SJ, Pye K (2001) GRADISTAT: a grain size distribution and statistics package for the analysis of unconsolidated sediments. Earth Surf Process Landforms 26:1237–1248. https://doi.org/10.1002/esp.261

Blouin VM, Schmidt MG, Bulmer CE, Krzic M (2005) Mechanical disturbance impacts on soil properties and lodgepole pine growth in British Columbia's central interior. Can J Soil Sci 85:681–691. https://doi.org/10.4141/S04-077

Bonan GB (1989) Environmental factors and ecological processes controlling vegetation patterns in boreal forests. Landscape Ecol 3:111–130. https://doi.org/10.1007/BF00131174

Brantley SL, Goldhaber MB, Ragnarsdottir KV (2007) Crossing Disciplines and Scales to Understand the Critical Zone. Elements 3:307–314. https://doi.org/10.2113/gselements.3.5.307

Braverman M, Quinton WL (2016) Hydrological impacts of seismic lines in the wetland-dominated zone of thawing, discontinuous permafrost, Northwest Territories, Canada. Hydrological Processes 30:2617–2627. https://doi.org/10.1002/hyp.10695

Brown MG, Black TA, Nesic Z, et al (2014) Evapotranspiration and canopy characteristics of two lodgepole pine stands following mountain pine beetle attack:

EVAPOTRANSPIRATION FOLLOWING MOUNTAIN PINE BEETLE ATTACK. Hydrol Process 28:3326–3340. https://doi.org/10.1002/hyp.9870

Brown S, Biswas A, Caron J, et al (2021) Soil Physics

Busby JR, Bliss LC, Hamilton CD (1978) Microclimate control of growth rates and habitats of the boreal forest mosses, Tomenthypnum nitens and Hylocomium splendens. Ecol Monogr 48:95–110

Calabrese S, Porporato A (2020) Wetness controls on global chemical weathering. Environ Res Commun 2:085005. https://doi.org/10.1088/2515-7620/abad7b

Campbell GS (1974) A Simple Method for Determining Unsaturated Conductivity from Moisture Retention Data. Soil Science 117:311–314

Caners RT, Lieffers VJ (2014) Divergent Pathways of Successional Recovery for In Situ Oil Sands Exploration Drilling Pads on Wooded Moderate-Rich Fens in Alberta, Canada: Divergent Pathways of Succesional Recovery. Restor Ecol 22:657–667. https://doi.org/10.1111/rec.12123

Caplan JS, Yeakley JA (2010) Water relations advantages for invasive Rubus armeniacus over two native ruderal congeners. Plant Ecol 210:169–179. https://doi.org/10.1007/s11258-010-9747-4

Chorover J, Troch PA, Rasmussen C, et al (2011) How Water, Carbon, and Energy Drive Critical Zone Evolution: The Jemez–Santa Catalina Critical Zone Observatory. Vadose zone j 10:884–899. https://doi.org/10.2136/vzj2010.0132

Corlett H, Playter T, Babakhani M, et al (2019) AER/AGS Open File Report: Regional Stratigraphic Correlation and 3D Geological Modelling of West-Central Alberta

Craig H (1961) Isotopic Variations in Meteoric Waters. Science 133:1702–1703. https://doi.org/10.1126/science.133.3465.1702

Cuenca RH, Stangel DE, Kelly SF (1997) Soil water balance in a boreal forest. J Geophys Res 102:29355–29365. https://doi.org/10.1029/97JD02312

Dabros A, Pyper M, Castilla G (2018) Seismic lines in the boreal and arctic ecosystems of North America: environmental impacts, challenges, and opportunities. Environ Rev 26:214–229. https://doi.org/10.1139/er-2017-0080

Davidson SJ, Goud EM, Franklin C, et al (2020) Seismic Line Disturbance Alters Soil Physical and Chemical Properties Across Boreal Forest and Peatland Soils. Front Earth Sci 8:. https://doi.org/10.3389/feart.2020.00281

Dawson FM, Kalkreuth WD, Sweet AR (1994) Stratigraphy and coal resource potential of the Upper Cretaceous to Tertiary Strata of northwestern Alberta. Geological Survey of Canada, Ottawa, Ont

Devito K, Creed I, Gan T, et al (2005) A framework for broad-scale classification of hydrologic response units on the Boreal Plain: is topography the last thing to consider? Hydrol Process 19:1705–1714. https://doi.org/10.1002/hyp.5881

Devito K, Mendoza C, Qualizza C (2012) Conceptualizing water movement in the Boreal Plains. Implications for watershed reconstruction. 165

Devito KJ, Hokanson KJ, Moore PA, et al (2017) Landscape controls on long-term runoff in subhumid heterogeneous Boreal Plains catchments. Hydrol Process 31:2737–2751. https://doi.org/10.1002/hyp.11213

Drever JI (1994) The effect of land plants on weathering rates of silicate minerals. Geochimica et Cosmochimica Acta 58:2325–2332. https://doi.org/10.1016/0016-7037(94)90013-2

ECCC (2011) Historical Climate Data - Climate - Environment and Climate Change Canada. https://climate.weather.gc.ca/. Accessed 12 Jul 2022

Ecological Stratification Working Group (1996) A national ecological framework for Canada. Centre for Land and Biological Resources Research, Research Branch, Agriculture and Agri-Food Canada, Ottawa

Environment Canada (2013) A National Ecological Framework for Canada - GIS data. https://sis.agr.gc.ca/cansis/nsdb/ecostrat/gis_data.html. Accessed 6 Sep 2022

Essington ME (2015) Soil and Water Chemistry An Integrative Approach, 2nd edn. CRC Press Taylor & Francis Group

Fang K, Kou D, Wang G, et al (2017) Decreased Soil Cation Exchange Capacity Across Northern China's Grasslands Over the Last Three Decades: CEC dynamics across grasslands. J Geophys Res Biogeosci 122:3088–3097. https://doi.org/10.1002/2017JG003968

Ferone JM, Devito KJ (2004) Shallow groundwater–surface water interactions in pond–peatland complexes along a Boreal Plains topographic gradient. Journal of Hydrology 292:75–95. https://doi.org/10.1016/j.jhydrol.2003.12.032

Filicetti A, Cody M, Nielsen S (2019) Caribou Conservation: Restoring Trees on Seismic Lines in Alberta, Canada. Forests 10:185. https://doi.org/10.3390/f10020185

Filicetti AT, Nielsen SE (2022) Effects of wildfire and soil compaction on recovery of narrow linear disturbances in upland mesic boreal forests. Forest Ecology and Management 510:120073. https://doi.org/10.1016/j.foreco.2022.120073

Finnegan L, MacNearney D, Pigeon KE (2018) Divergent patterns of understory forage growth after seismic line exploration: Implications for caribou habitat restoration. Forest Ecology and Management 409:634–652. https://doi.org/10.1016/j.foreco.2017.12.010

Flerchinger GN (2017a) The Simultaneous Heat and Water (SHAW) Model: Technical Documentation 3.0

Flerchinger GN (2017b) The Simultaneous Heat and Water (SHAW) Model: User's Manual Version 3.0.x

Flerchinger GN, Hanson CL (1989) Modeling Soil Freezing and Thawing on a Rangeland Watershed. Transactions of the ASAE 32:1551–1554

Flerchinger GN, Hanson CL, Wight JR (1996) Modeling Evapotranspiration and Surface Energy Budgets Across a Watershed. Water Resour Res 32:2539–2548. https://doi.org/10.1029/96WR01240

Flerchinger GN, Hardegree SP (2004) Modelling near-surface soil temperature and moisture for germination response predictions of post-wildfire seedbeds. Journal of Arid Environments 59:369–385. https://doi.org/10.1016/j.jaridenv.2004.01.016

Flerchinger GN, Kustas WP, Weltz MA (1998) Simulating Surface Energy Fluxes and Radiometric Surface Temperatures for Two Arid Vegetation Communities Using the SHAW Model. J Appl Meteor 37:449–460. https://doi.org/10.1175/1520-0450(1998)037<0449:SSEFAR>2.0.CO;2

Flerchinger GN, Pierson FB (1997) Modelling plant canopy effects on variability of soil temperature and water: model calibration and validation. Journal of Arid Environments 35:641–653. https://doi.org/10.1006/jare.1995.0167

Flerchinger GN, Pierson FB (1991) Modeling plant canopy effects on variability of soil temperature and water. Agricultural and Forest Meteorology 56:227–246. https://doi.org/10.1016/0168-1923(91)90093-6

Flerchinger GN, Saxton KE (1989) Simultaneous heat and water model of freezing snow-residue-oil system I theory and development. Transactions of American Society of Agricultural Engineers 32:565–571

Flinn MA, Wein RW (1977) Depth of underground plant organs and theoretical survival during fire. Canadian Journal of Botany 55:2550–2554

Flury M, Flühler H, Jury WA, Leuenberger J (1994) Susceptibility of soils to preferential flow of water: A field study. Water Resour Res 30:1945–1954. https://doi.org/10.1029/94WR00871

Fox Creek Historical Association (1992) Iosegun Reflections: A History of Fox Creek. Fox Creek Historical Association

Freeze RA, Cherry JA (1979) Groundwater. Prentice-Hall, Englewood Cliffs, N.J

G. N. Flerchinger, T. G. Caldwell, J. Cho, S. P. Hardegree (2012) Simultaneous Heat and Water (SHAW) Model: Model Use, Calibration, and Validation. Transactions of the ASABE 55:1395–1411. https://doi.org/10.13031/2013.42250

Geris J, Tetzlaff D, McDonnell J, Soulsby C (2015) The relative role of soil type and tree cover on water storage and transmission in northern headwater catchments. Hydrological Processes 29:1844–1860. https://doi.org/10.1002/hyp.10289

Gibson DW (1977) Upper Cretaceous and Tertiary coal-bearing strata in the Drumheller-Ardley region, Red Deer River valley, Alberta, Paper 76-35. Geological Survey of Canada

Goeking SA, Tarboton DG (2020) Forests and Water Yield: A Synthesis of Disturbance Effects on Streamflow and Snowpack in Western Coniferous Forests. Journal of Forestry 118:172–192. https://doi.org/10.1093/jofore/fvz069

Goldsmith GR, Muñoz-Villers LE, Holwerda F, et al (2012) Stable isotopes reveal linkages among ecohydrological processes in a seasonally dry tropical montane cloud forest: TROPICAL MONTANE CLOUD FOREST ECOHYDROLOGY. Ecohydrol 5:779–790. https://doi.org/10.1002/eco.268

Gosselin J-S (2022) jnsebgosselin/gwhat

Gosselin J-S (2016) ESTIMATION DE LA RECHARGE À PARTIR DE SÉRIES TEMPORELLES DE LA TEMPÉRATURE DU SOL, DES NIVEAUX D'EAU DANS LES PUITS ET DE DONNÉES MÉTÉOROLOGIQUES: DÉVELOPPEMENT MÉTHODOLOGIQUE ET ÉVALUATION DE L'INCERTITUDE - Ph.D. Thesis

Gosselin JS, Rivard C, Martel R, Lefebvre R (2016) Application limits of the interpretation of near-surface temperature time series to assess groundwater recharge. Journal of Hydrology 538:96–108

Government of Alberta (2017) Provincial Woodland Caribou Range Plan. 212

Grasby SE, Chen Z, Hamblin AP, et al (2008) Regional characterization of the Paskapoo bedrock aquifer system, southern AlbertaGeological Survey of Canada Contribution 2008-0479. Can J Earth Sci 45:1501–1516. https://doi.org/10.1139/E08-069

Gray DM, Prowse T (1993) Snow and floating ice. In: Handbook of Hydrology. McGraw-Hill Inc., New York, p 7.1-7.58

Green IRA, Stephenson D (1986) Criteria for comparison of single event models. Hydrological Sciences Journal 31:395–411

Green WH, Ampt G (1911) Studies on soil physics. Journal of Agricultural Sciences 4:1–24

Grelle A, Lundberg A, Lindroth A, et al (1997) Evaporation components of a boreal forest: variations during the growing season. Journal of Hydrology 197:70–87. https://doi.org/10.1016/S0022-1694(96)03267-2

Gröning M, Lutz HO, Roller-Lutz Z, et al (2012) A simple rain collector preventing water re-evaporation dedicated for δ18O and δ2H analysis of cumulative precipitation samples. Journal of Hydrology 448–449:195–200. https://doi.org/10.1016/j.jhydrol.2012.04.041

Grossnickle SC (2000) Ecophysiology of Northern Spruce Species: The performance of Planted Seedlings. NRC Research Press 409

Guarin-Martinez LI (2022) CHARACTERIZATION AND NUMERICAL MODELING OF THE BEDROCK AQUIFER IN THE FOX CREEK AREA, ALBERTA. Maîtrise en sciences de la terre, Université du Québec

Haag RW, Bliss LC (1974) Energy Budget Changes Following Surface Disturbance to Upland Tundra. The Journal of Applied Ecology 11:355. https://doi.org/10.2307/2402027

Hathway B, Plint AG (2011) Late Maastrichtian paleovalley systems in west-central Alberta: Mapping the Battle Formation in the subsurface. Bulletin of Canadian Petroleum Geology 59:195–206. https://doi.org/10.2113/gscpgbull.59.3.195

Hayhoe HN (1994) Field testing of simulated soil freezing and thawing by the SHAW model. Canadian Agri Eng 36:279–285

Hébert F, Thiffault N (2011) The Biology of Canadian Weeds. 146. *Rhododendron groenlandicum* (Oeder) Kron and Judd. Can J Plant Sci 91:725–738. https://doi.org/10.4141/cjps2010-012

Heck K, Coltman E, Schneider J, Helmig R (2020) Influence of Radiation on Evaporation Rates: A Numerical Analysis. Water Resour Res 56:. https://doi.org/10.1029/2020WR027332

Hopmans JW, van Genuchten MT (2005) Vadose Zone: Hydrologic Processes. Elsevier

Huang M, Gallichand J (2006) Use of the SHAW model to assess soil water recovery after apple trees in the gully region of the Loess Plateau, China. Agricultural Water Management 85:67–76. https://doi.org/10.1016/j.agwat.2006.03.009

Hughes AT, Smerdon BD, Alessi DS (2017) Hydraulic properties of the Paskapoo Formation in west-central Alberta. Can J Earth Sci 54:883–892. https://doi.org/10.1139/cjes-2016-0164

Hymer DC, Moran MS, Keefer TO (2000) Soil Water Evaluation Using a Hydrologic Model and Calibrated Sensor Network. Soil Sci Soc Am J 64:319–326. https://doi.org/10.2136/sssaj2000.641319x

IPCC (2023) Climate Change 2022 – Impacts, Adaptation and Vulnerability: Working Group II Contribution to the Sixth Assessment Report of the Intergovernmental Panel on Climate Change, 1st edn. Cambridge University Press

IPCC (ed) (2007) Climate change 2007: the physical science basis: contribution of Working Group I to the Fourth Assessment Report of the Intergovernmental Panel on Climate Change. Cambridge University Press, Cambridge ; New York

Ireson AM, Barr AG, Johnstone JF, et al (2015) The changing water cycle: the Boreal Plains ecozone of Western Canada. WIREs Water 2:505–521. https://doi.org/10.1002/wat2.1098

Jenkins SR, Moore RC (1977) A Proposed Modification to the Classical Method of Calculating Alkalinity in Natural Waters. AWWA 69:56–60. http://www.jstor.org/stable/41268672

Jones C, Van Dongen A, Harvey J, Degenhardt D (2022) Field sampling methods on seismic lines: a comparison between circular plots and belt transects. Restoration Ecology 30:. https://doi.org/10.1111/rec.13619

Jorgenson JC, Hoef JMV, Jorgenson MT (2010) Long-term recovery patterns of arctic tundra after winter seismic exploration. Ecological Applications 20:205–221. https://doi.org/10.1890/08-1856.1

Kalra YP, Maynard DG (1991) Manual for forest soil and plant analysis. Forestry Canada, Northwest Region

Kang E, Cheng G, Song K, et al (2005) Simulation of energy and water balance in Soil-Vegetation-Atmosphere Transfer system in the mountain area of Heihe River Basin at Hexi Corridor of northwest China. Sci China Ser D-Earth Sci 48:538–548. https://doi.org/10.1360/02yd0428

Kaufmann MR (1975) Leaf Water Stress in Engelmann Spruce: Influence of the Root and Shoot Environments. Plant Physiol 56:841–844. https://doi.org/10.1104/pp.56.6.841

Kelly EF, Chadwick OA, Hilinski TE (1998) The Effects of Plants on Mineral Weathering. Biogeochemistry 42:21–53. https://doi-org.login.ezproxy.library.ualberta.ca/10.1023/A:1005919306687

Kinar NJ, Pomeroy JW (2015) Measurement of the physical properties of the snowpack: MEASUREMENT OF SNOWPACK. Rev Geophys 53:481–544. https://doi.org/10.1002/2015RG000481

Knapik LJ, Lindsay JD (1983) Reconnaisance Soil Survey of the Iosegun Lake Area, Alberta

Kumaragamage D, Warren J, Spiers G (2021) Soil Chemistry

Kurz WA, Shaw CH, Boisvenue C, et al (2013) Carbon in Canada's boreal forest — A synthesis. Environ Rev 21:260–292. https://doi.org/10.1139/er-2013-0041

Landon MK, Delin GN, Komor SC, Regan CP (1999) Comparison of the stable-isotopic composition of soil water collected from suction lysimeters, wick samplers, and cores in a sandy unsaturated zone. Journal of Hydrology 224:45–54. https://doi.org/10.1016/S0022-1694(99)00120-1

Landwehr JM, Coplen TB (2004) Line-conditioned excess: A new method for characterizing stable hydrogen and oxygen isotope ratios in hydrologic systems (IAEA-CN--118)

Langmuir D (1997) Aqueous Environmental Geochemistry. Prentice Hall, Upper Saddle River, New Jersey

Le T, Ha T, Darling S, Xu B (2023) Historical Land Use Changes and Lichen-Rich Ecosites near Fox Creek, Alberta. UNpublished manuscript

Lee P, Boutin S (2006) Persistence and developmental transition of wide seismic lines in the western Boreal Plains of Canada. Journal of Environmental Management 78:240–250. https://doi.org/10.1016/j.jenvman.2005.03.016

Lieb AM, Darrouzet-Nardi A, Bowman WD (2011) Nitrogen deposition decreases acid buffering capacity of alpine soils in the southern Rocky Mountains. Geoderma 164:220–224. https://doi.org/10.1016/j.geoderma.2011.06.013

Link TE, Flerchinger GN, Unsworth M, Marks D (2004) Simulation of Water and Energy Fluxes in an Old-Growth Seasonal Temperate Rain Forest Using the Simultaneous Heat and Water (SHAW) Model. J Hydrometeor 5:443–457. https://doi.org/10.1175/1525-7541(2004)005<0443:SOWAEF>2.0.CO;2

Lützow M v., Kögel-Knabner I, Ekschmitt K, et al (2006) Stabilization of organic matter in temperate soils: mechanisms and their relevance under different soil conditions - a

review: Mechanisms for organic matter stabilization in soils. European Journal of Soil Science 57:426–445. https://doi.org/10.1111/j.1365-2389.2006.00809.x

Lyster S, Andriashek LD (2012) Geostatistical Rendering of the Architecture of Hydrostratigraphic Units within the Paskapoo Formation, Central Alberta. 115

MacFarlane AK (2013) Vegetation response to seismic lines: edge effects and on-line succession. University of Alberta

Mathys A, Black TA, Nesic Z, et al (2013) Carbon balance of a partially harvested mixed conifer forest following mountain pine beetle attack and its comparison to a clear-cut. Biogeosciences 10:5451–5463. https://doi.org/10.5194/bg-10-5451-2013

Maule CP, Chanasyk DS, Muehlenbachs K (1994) Isotopic determination of snow-water contribution to soil water and groundwater. Journal of Hydrology 155:73–91. https://doi.org/10.1016/0022-1694(94)90159-7

McNamara JP, Chandler D, Seyfried M, Achet S (2005) Soil moisture states, lateral flow, and streamflow generation in a semi-arid, snowmelt-driven catchment. Hydrol Process 19:4023–4038. https://doi.org/10.1002/hyp.5869

METER (2021) TEROS 12. In: METER. https://www.metergroup.com/en/meter-environment/products/teros-12-soil-moisture-sensor. Accessed 8 Jun 2023

Meyer G, Black TA, Jassal RS, et al (2017) Measurements and simulations using the 3-PG model of the water balance and water use efficiency of a lodgepole pine stand following mountain pine beetle attack. Forest Ecology and Management 393:89–104. https://doi.org/10.1016/j.foreco.2017.03.019

Moore G, McGuire K, Troch P, Barron-Gafford G (2015) Chapter 8 - Ecohydrology and the Critical Zone: Processes and Patterns Across Scales. Elsevier: Developments in Earth Surface Processes 19:239–266. https://doi.org/10.1016/B978-0-444-63369-9.00008-2

Nash JE, Sutcliffe JV (1970) River flow forecasting through conceptual models: Part 1 - a discussion of principles. Journal of Hydrology 44:282–290

Nijssen B, Lettenmaier DP (2002) Water balance dynamics of a boreal forest watershed: White Gull Creek basin, 1994-1996: WHITE GULL CREEK BASIN, 1994-1996. Water Resour Res 38:37-1-37–12. https://doi.org/10.1029/2001WR000699

Nosetto MD, Jobbagy EG, Paruelo JM (2005) Land-use change and water losses: the case of grassland afforestation across a soil textural gradient in central Argentina. Global Change Biol 11:1101–1117. https://doi.org/10.1111/j.1365-2486.2005.00975.x

NRCan (2020) Statistical data | Natural Resources Canada. https://cfs.nrcan.gc.ca/statsprofile/inventory/borealplains. Accessed 25 Nov 2022

Oliver BG, Thurman EM, Malcolm RL (1983) The contribution of humic substances to the acidity of colored natural waters. Geochimica et Cosmochimica Acta 47:2031–2035. https://doi.org/10.1016/0016-7037(83)90218-1

Páez-Bimos S, Molina A, Calispa M, et al (2023) Soil–vegetation–water interactions controlling solute flow and chemical weathering in volcanic ash soils of the high Andes. Hydrol Earth Syst Sci 27:1507–1529. https://doi.org/10.5194/hess-27-1507-2023

Pan Y, Birdsey RA, Fang J, et al (2011) A Large and Persistent Carbon Sink in the World's Forests. Science 333:988–993. https://doi.org/10.1126/science.1201609

Pasher J, Seed E, Duffe J (2013) Development of boreal ecosystem anthropogenic disturbance layers for Canada based on 2008 to 2010 Landsat imagery. Canadian Journal of Remote Sensing 39:42–58. https://doi.org/10.5589/m13-007

Peel MC, Finlayson BL, McMahon TA (2007) Updated world map of the Ko¨ppen-Geiger climate classification. Hydrol Earth Syst Sci 12

Pejam MR, Arain MA, McCaughey JH (2006) Energy and water vapour exchanges over a mixedwood boreal forest in Ontario, Canada. Hydrol Process 20:3709–3724. https://doi.org/10.1002/hyp.6384

Pennock DJ (2021) Soil Genesis

Petrone RM, Silins U, Devito KJ (2007) Dynamics of evapotranspiration from a riparian pond complex in the Western Boreal Forest, Alberta, Canada. Hydrol Process 21:1391–1401. https://doi.org/10.1002/hyp.6298

Pomeroy JW, Gray DM (1995) Snowcover accumulation, relocation, and management

Pomeroy JW, Gray DM, Shook KR, et al (1998) An evaluation of snow accumulation and ablation processes for land surface modelling. Hydrol Process 12:2339–2367. https://doi.org/10.1002/(SICI)1099-1085(199812)12:15<2339::AID-HYP800>3.0.CO;2-L

Pope GA (2015) Regolith and Weathering (Rock Decay) in the Critical Zone. In: Developments in Earth Surface Processes. Elsevier, pp 113–145

Proulx R, Rheault G, Bonin L, et al (2015) How much biomass do plant communities pack per unit volume? PeerJ 3:e849. https://doi.org/10.7717/peerj.849

Quideau S, Simpson M, Gillespie A (2021) Soil Organic Matter

Renée Brooks J, Barnard HR, Coulombe R, McDonnell JJ (2010) Ecohydrologic separation of water between trees and streams in a Mediterranean climate. Nature Geosci 3:100–104. https://doi.org/10.1038/ngeo722

Revel R, Dougherty TD, Downing DJ (1984) Forest Growth and Revegetation Along Seismic Lines. United States

Richardson JB (2017) Critical Zone. In: Bobrowsky P, Marker B (eds) Encyclopedia of Engineering Geology. Springer International Publishing, Cham, pp 1–5

Rivard C, Lavoie D, Lefebvre R, et al (2014) An overview of Canadian shale gas production and environmental concerns. International Journal of Coal Geology 126:64–76. https://doi.org/10.1016/j.coal.2013.12.004

Russell T, Pendlebury D, Ronson A (2016) Alberta's Caribou: A Guide to Range Planning. Canadian Parks and Wilderness Society Northern Alberta (CPAWS) Vol. 2: Little Smoky:

Rutkowski DR, Stottlemyer R (1993) Composition, Biomass and Nutrient Distribution in Mature Northern Hardwood and Boreal Forest Stands, Michigan. American Midland Naturalist 130:13. https://doi.org/10.2307/2426271

Saxton KE, Rawls WJ, Romberger JS, Papendick RI (1986) Estimating Generalized Soil-water Characteristics from Texture. Soil Science Society of AMerica Journal 50:1031–1036

Scheffer RA, Van Logtestijn RSP, Verhoeven JTA (2001) Decomposition of *Carex* and *Sphagnum* litter in two mesotrophic fens differing in dominant plant species. Oikos 92:44–54. https://doi.org/10.1034/j.1600-0706.2001.920106.x

Schnoor JL, Stumm W (1986) The role of chemical weathering in the neutralization of acidic deposition. Schweiz Z Hydrol 48:171–195. https://doi.org/10.1007/BF02560197

Schwartzman DW, Volk T (1989) Biotic enhancement of weathering and the habitability of Earth. Nature 340:457–460. https://doi.org/10.1038/340457a0

Smerdon B, Klassen J, Gardner WP (2019) AER/AGS Report 98: Hydrogeological Characterization of the Upper Cretaceous–Quaternary Units in the Fox Creek Area, West-Central Alberta. 49

Smerdon BD, Devito KJ, Mendoza CA (2005) Interaction of groundwater and shallow lakes on outwash sediments in the sub-humid Boreal Plains of Canada. Journal of Hydrology 314:246–262. https://doi.org/10.1016/j.jhydrol.2005.04.001

Smerdon BD, Redding T, Beckers J (2009) An overview of the effects of forest management on groundwater hydrology. JEM. https://doi.org/10.22230/jem.2009v10n1a409

Sprenger M, Tetzlaff D, Buttle J, et al (2018) Measuring and Modeling Stable Isotopes of Mobile and Bulk Soil Water. Vadose Zone Journal 17:1–18. https://doi.org/10.2136/vzj2017.08.0149

Stephens DB (1996) Vadose Zone Hydrology, 1st edn. CRC Press

Strack M, Hayne S, Lovitt J, et al (2019) Petroleum exploration increases methane emissions from northern peatlands. Nat Commun 10:2804. https://doi.org/10.1038/s41467-019-10762-4

Strack M, Softa D, Bird M, Xu B (2018) Impact of winter roads on boreal peatland carbon exchange. Glob Change Biol 24:e201–e212. https://doi.org/10.1111/gcb.13844

Strong WL, La Roi GH (1983a) Root-system morphology of common boreal forest trees in Alberta, Canada. Canadian Journal of Forest Research 13 (6):1164–1173

Strong WL, La Roi GH (1983b) Rooting depths and successional development of selected boreal forest communities. Canadian Journal of Forest Research 13:

Sun N, Yan H, Wigmosta MS, et al (2022) Forest Canopy Density Effects on Snowpack Across the Climate Gradients of the Western United States Mountain Ranges. Water Resources Research 58:. https://doi.org/10.1029/2020WR029194

Thornthwaite CW (1948) An Approach toward a Rational Classification of Climate. Geographical Review 38:55–94

Timoney K, Lee P (2001) Environmental management in resource-rich Alberta, Canada: first world jurisdiction, third world analogue? Journal of Environmental Management 63:387–405

Turetsky MR, Crow SE, Evans RJ, et al (2008) Trade-offs in resource allocation among moss species control decomposition in boreal peatlands. Journal of Ecology 96:1297–1305. https://doi.org/10.1111/j.1365-2745.2008.01438.x

van Rensen CK, Nielsen SE, White B, et al (2015) Natural regeneration of forest vegetation on legacy seismic lines in boreal habitats in Alberta's oil sands region. Biological Conservation 184:127–135. https://doi.org/10.1016/j.biocon.2015.01.020

Vitt DH, Achuff P, Andrus RE (1975) The vegetation and chemical properties of patterned fens in the Swan Hills, north central Alberta. Can J Bot 53:2776–2795. https://doi.org/10.1139/b75-306

Vitt DH, Chee W-L (1990) The relationships of vegetation to surface water chemistry and peat chemistry in fens of Alberta, Canada. Vegetatio 89:87–106. https://doi.org/10.1007/BF00032163

Vitt DH, Halsey LA, Bauer IE, Campbell C (2000) Spatial and temporal trends in carbon storage of peatlands of continental western Canada through the Holocene. 37:

Vrugt JA, Robinson BA (2007) Improved evolutionary optimization from genetically adaptive multimethod search. Proc Natl Acad Sci USA 104:708–711. https://doi.org/10.1073/pnas.0610471104

Waddington JM, Roulet NT (2000) Carbon balance of a boreal patterned peatland: CARBON BALANCE OF A BOREAL PATTERNED PEATLAND. Global Change Biology 6:87–97. https://doi.org/10.1046/j.1365-2486.2000.00283.x

Walker TN, Garnett MH, Ward SE, et al (2016) Vascular plants promote ancient peatland carbon loss with climate warming. Glob Change Biol 22:1880–1889. https://doi.org/10.1111/gcb.13213

Wang T, Hamann A, Spittlehouse D, Carroll C (2016) Locally downscaled and spatially customizable climate data for historical and future periods for North America. PLoS ONE 11:

Watmough SA, Dillon PJ (2003) Base Cation and Nitrogen Budgets for a Mixed Hardwood Catchment in South-central Ontario. Ecosystems 6:675–693. https://doi.org/10.1007/s10021-002-0164-y

Wei X, Giles-Hansen K, Spencer SA, et al (2022) Forest harvesting and hydrology in boreal Forests: Under an increased and cumulative disturbance context. Forest Ecology and Management 522:120468. https://doi.org/10.1016/j.foreco.2022.120468

Weihermüller L, Kasteel R, Vereecken H (2006) Soil Heterogeneity Effects on Solute Breakthrough Sampled with Suction Cups: Numerical Simulations. Vadose Zone Journal 5:886–893. https://doi.org/10.2136/vzj2005.0105

Wenner DB, Ketcham' PD, Dowd JF (1991) Stable isotopic composition of waters in a small Piedmont watershed. Stable Isotope Geochemistry: A Tribute to Samuel Epstein

White AF (2014) 5.05 Natural Weathering Rates of Silicate Minerals

Woo I, Zedler JB (2002) Can nutrients alone shift a sedge meadow towards dominance by the invasive Typha × glauca. Wetlands 22:509–521. https://doi.org/10.1672/0277-5212(2002)022[0509:CNASAS]2.0.CO;2

Yin Z, Ouyang H, Xu X, et al (2010a) Estimation of Evapotranspiration from Faber Fir Forest Ecosystem in the Eastern Tibetan Plateau of China Using SHAW Model. JWARP 02:143–153. https://doi.org/10.4236/jwarp.2010.22017

Yin ZF, Ouyang H, Chen H (2010b) Simulating Soil Freezing and Thawing of Temperate Desert Ecosystem on the Qinghai-Tibet Plateau. Procedia Environmental Sciences 2:476–485. https://doi.org/10.1016/j.proenv.2010.10.052

Zha T, Barr AG, Van Der Kamp G, et al (2010) Interannual variation of evapotranspiration from forest and grassland ecosystems in western canada in relation to drought. Agricultural and Forest Meteorology 150:1476–1484. https://doi.org/10.1016/j.agrformet.2010.08.003

Zhao P, Tang X, Zhao P, et al (2013) Identifying the water source for subsurface flow with deuterium and oxygen-18 isotopes of soil water collected from tension lysimeters and cores. Journal of Hydrology 503:1–10. https://doi.org/10.1016/j.jhydrol.2013.08.033

Zimmermann U, Ehhalt DH, Munnich KO (1967) Soil water movement and evapotranspiration: Changes in the isotopic composition of water. International Atomic Energy Agency Isotopes in Hydrology:567–584

Appendix

Appendix A Equipment Installed at all Study Sites

Table A.1: Monitoring equipment installed at all study sites.

Study Site	Equipment Installed					
	30 cm Lysimeter	60 cm Lysimeter	120 cm Lysimeter	Rain Collector	Soil Moisture and Temperature Sensors (15, 30, and 60 cm)	Weather Station
U1	x	✓	✓	✓	✓	✓
U2	✓	✓	✓	✓	✓	x
U3	x	✓	✓	✓	✓	x
L8	✓	✓	✓	✓	✓	✓
L12	✓	✓	✓	✓	✓	x

Appendix B XRD Machine Specifications

Instrument: Rigaku Ultima IV

Radiation Source: Cobalt tube at 38 kV and 38 mA

Anode	Wavelength (Å)		
	$K\alpha_1$ (100)	$K\alpha_2$ (50)	$K\beta_1$
Co	1.78900	1.79283	1.62083

Focusing Geometry: Bragg Brentano Mode

Detector: D/Tex Ultra with Fe Filter (K-beta filter)

Slit sizes used are:

Divergence Slit - 2/3deg

Divergence Height Limiting Slit - 10mm

Scattering slit - open

Receiving Slit - open

Scan Information:

Range: 5 to 90°

Scan Axis: 2Θ/Θ

Scan Mode: Continuous

Sampling Width (Step Size): 0.0200°

Scan Speed: 2.00 deg/min

Spin: none

Appendix C Soil Water Anion Measurement Methods

Table B.1: Measured anions in soil-water and the methods used for each anion.

Dissolved Ion	Method
NH_4-N	Salicylate-hypochlorite method (Bower and Holm-Hansen 1980)
Cl^-	Ferrithiocyante method *(EPA Method 325.2)*
PO_4-P	Molybdenum Blue Method *(EPA Method 365.1)*
NO_3+NO_2-N (TON) and NO_3 by calculation	Hydrazine Reduction Method *(EPA Method 353.1)*
NO_3+NO_2-N (TON-V)	Vanadium Chloride Reduction Method (Jokinen *et al*., 2013)
SO_4-S	Barium Chloride Turbidimetric Method *(EPA method 375.4)*

Appendix D Soil Moisture and Temperature Plots for Upland Sites U1 and U3

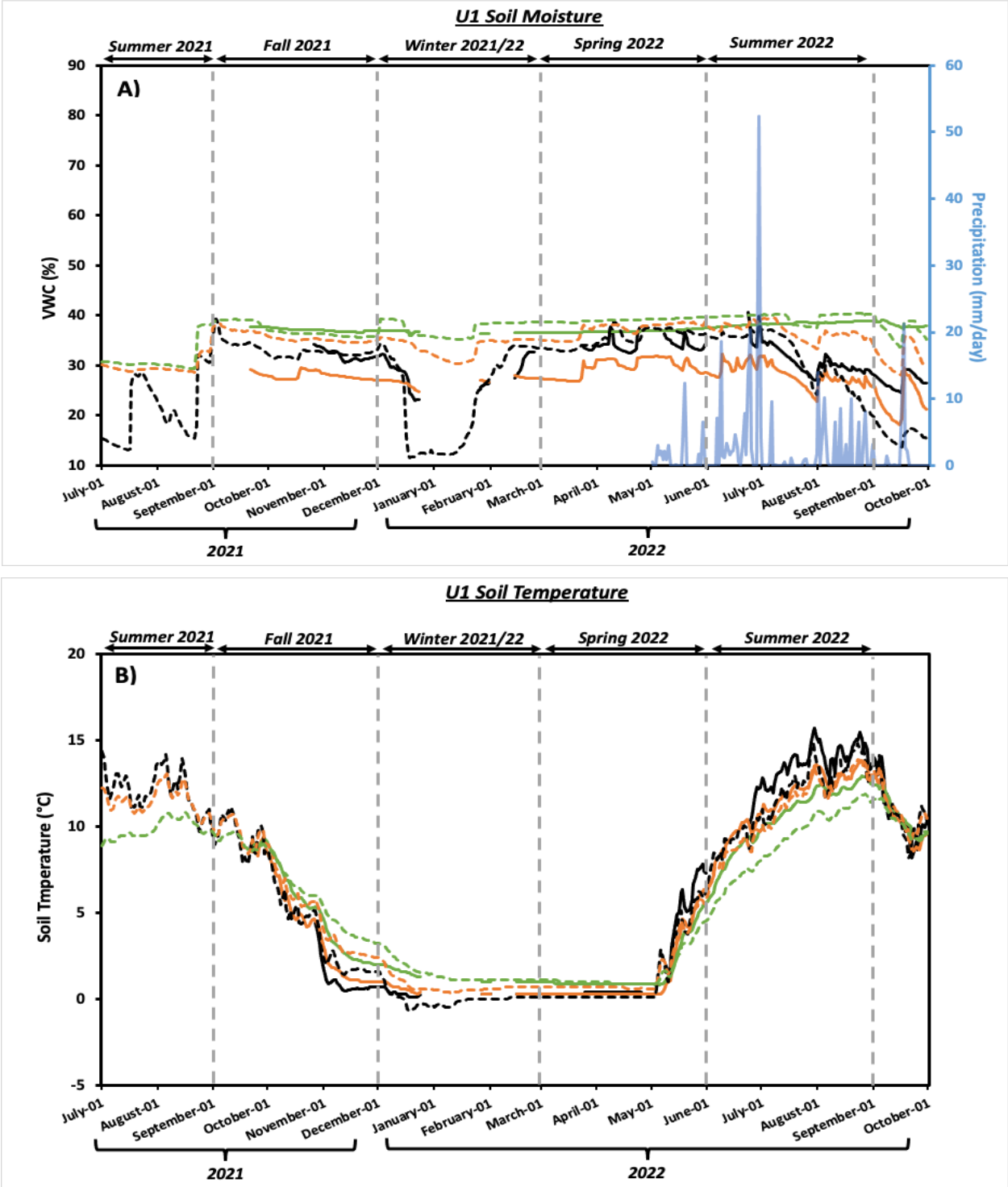

Figure D.1: Plots of A) soil-moisture response to precipitation and B) soil-temperature from July 2021 to October 2022 for Upland Site 1 (U1).

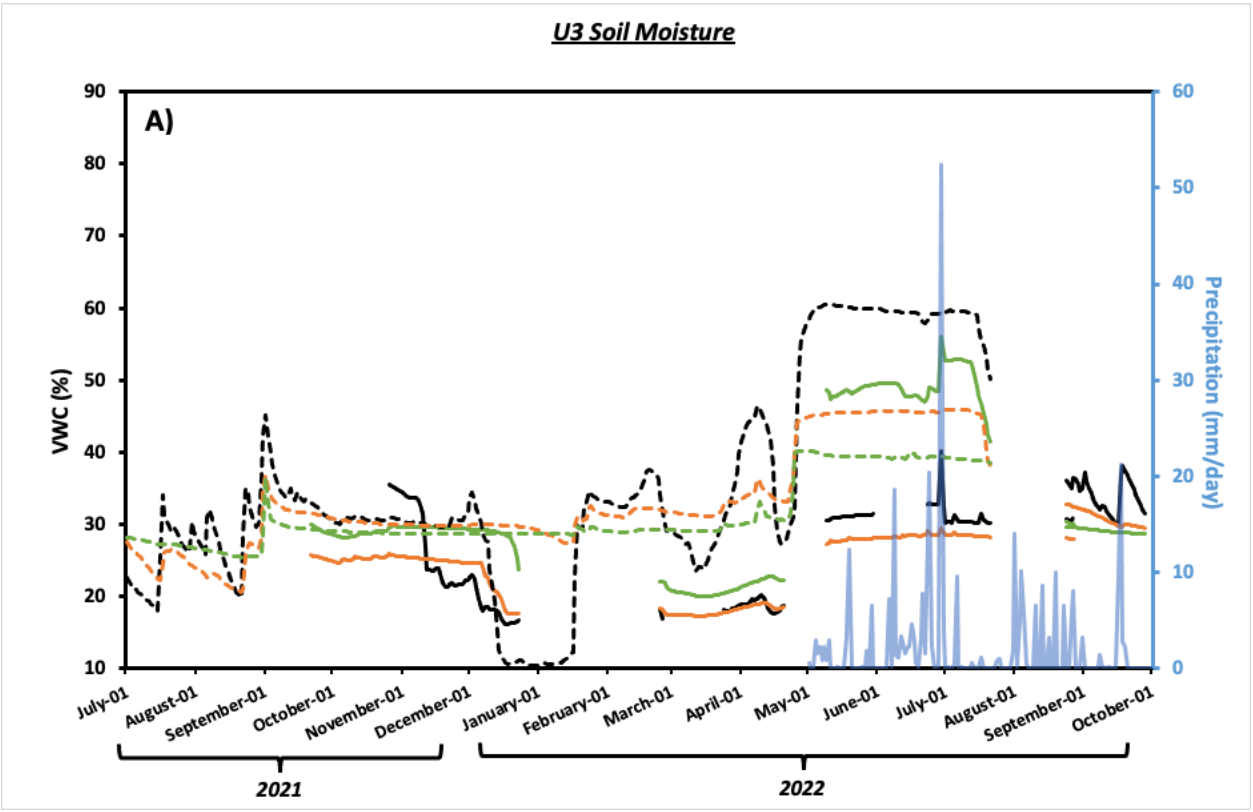

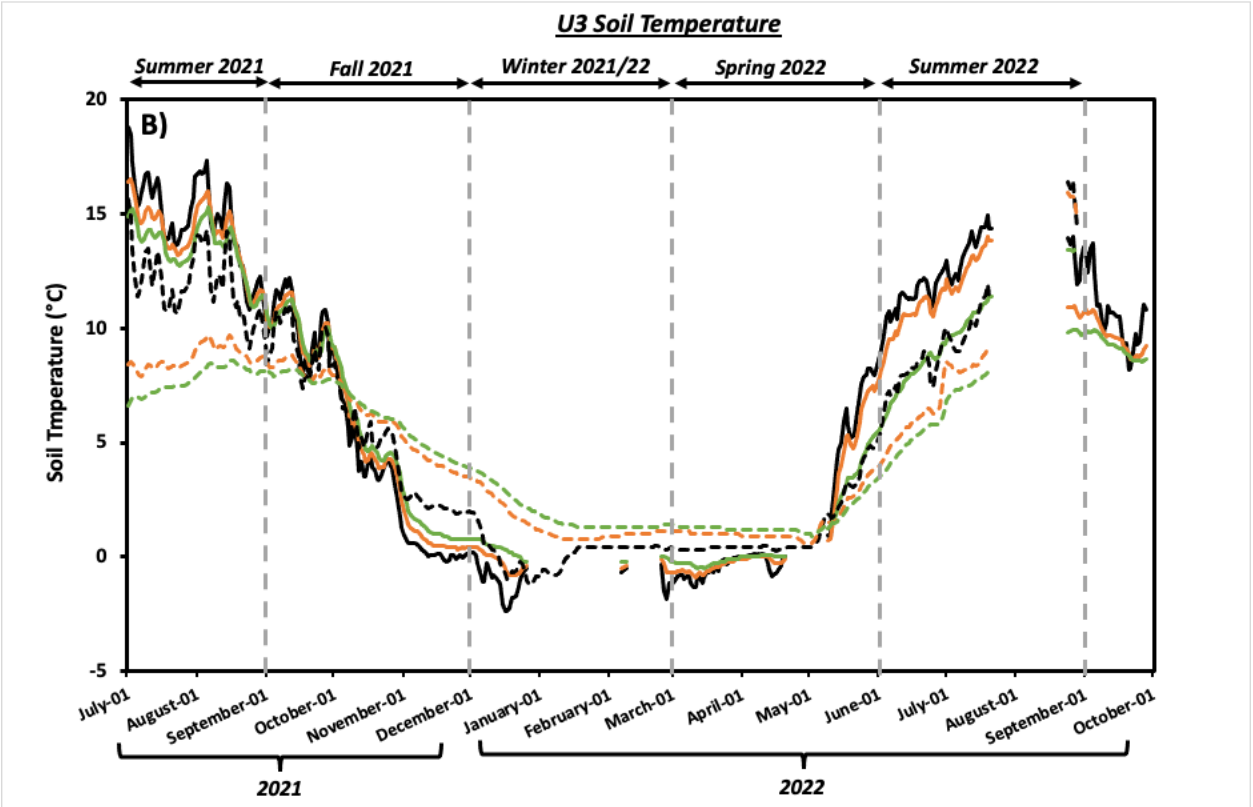

Figure D.2: Plots of A) soil-moisture response to precipitation and B) soil-temperature from July 2021 to October 2022 for Upland Site 3 (U3).

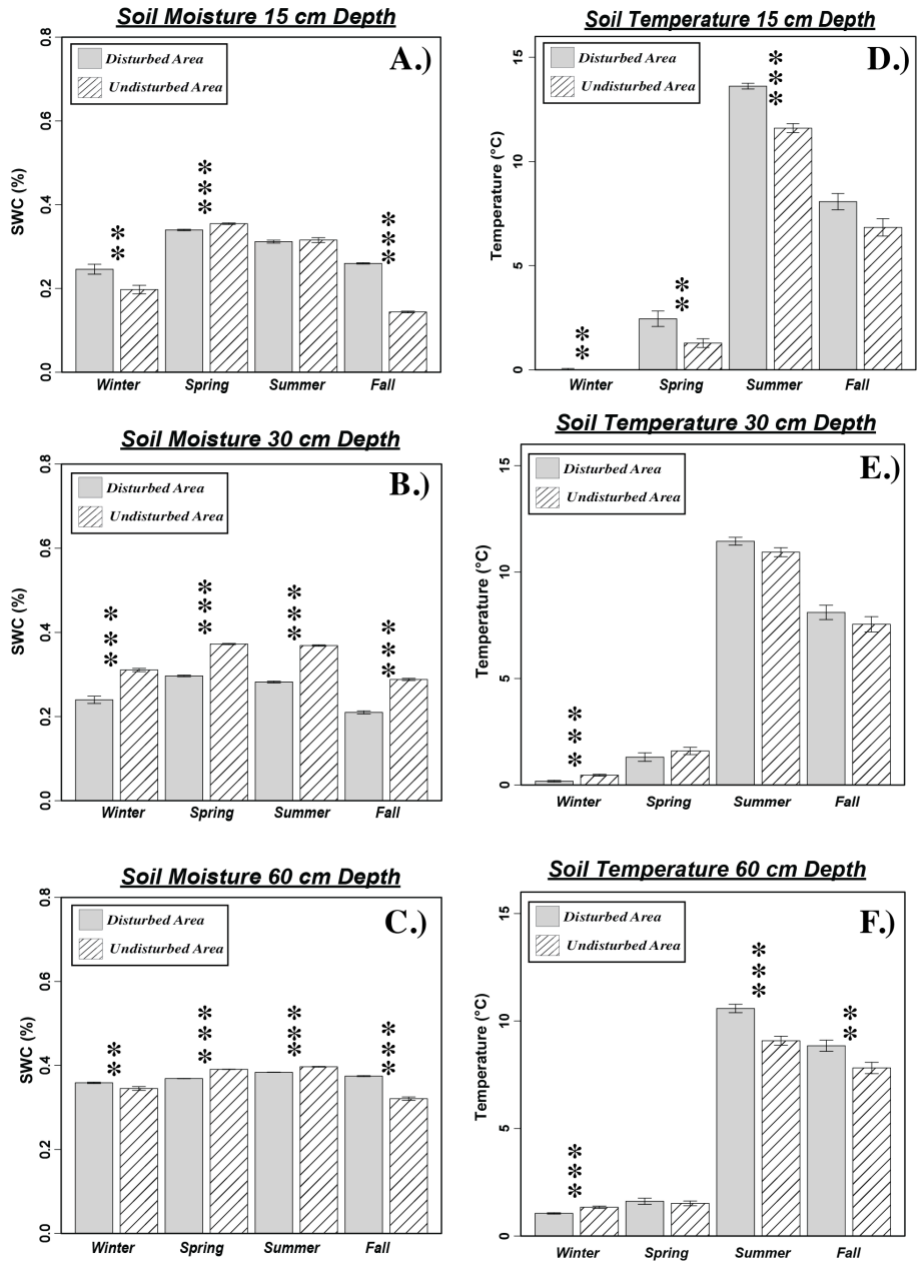

Figure D.3: Upland site 1 (U1) bar charts of soil moisture at A) 15 cm, B) 30 cm, and C) 60 cm and soil temperature at D) 15 cm, E) 30 cm, and F) 60 cm depths in the soil-profile. Error bars represent 95% confidence intervals. A two-sample t-test was applied for differences between the seismic line and adjacent undisturbed area at each depth for each season. Levels of significance: *, **, *** correspond to $p < 0.05$, $p < 0.01$, and $p < 0.001$ respectively.

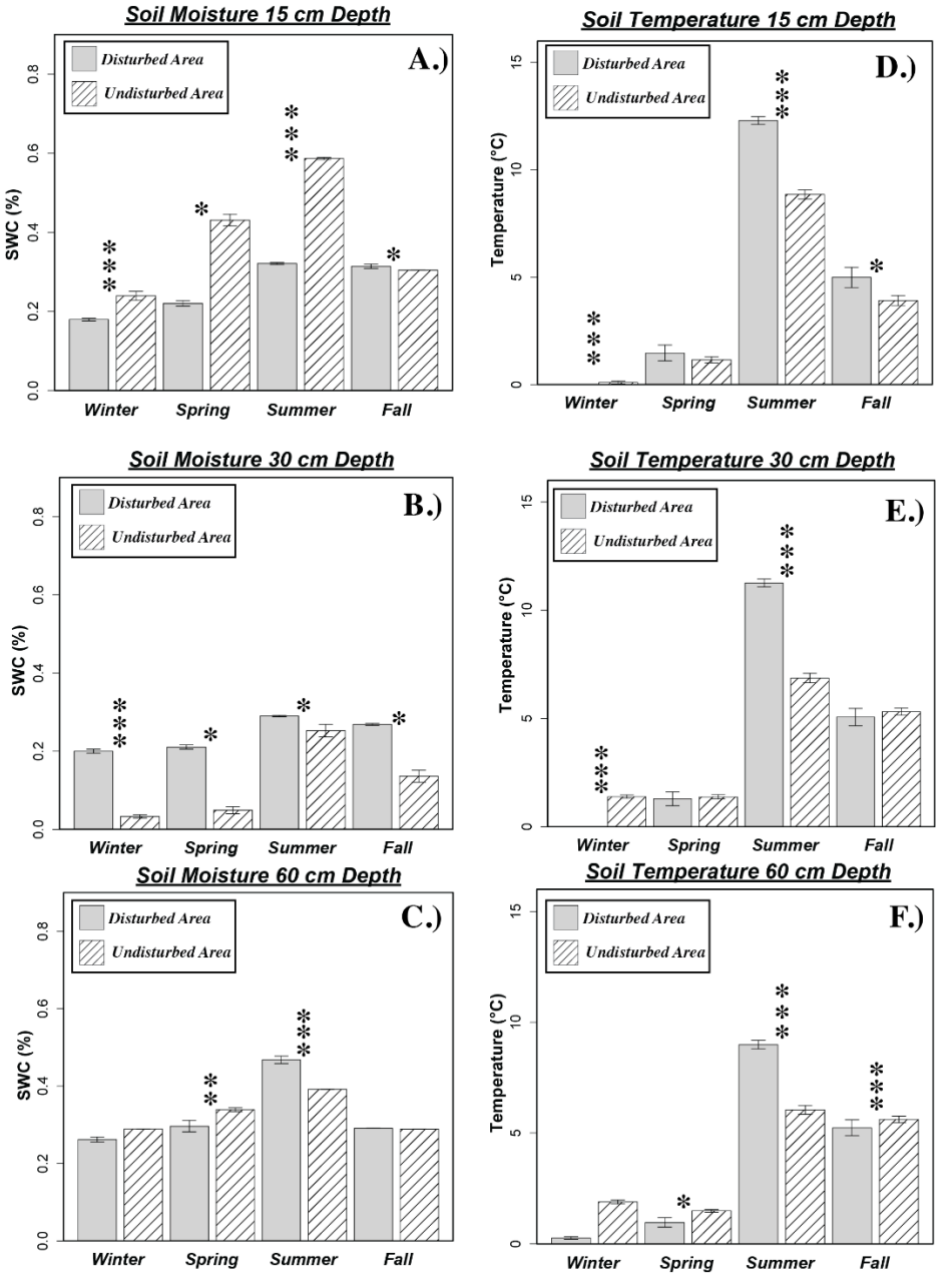

Figure D.4: Upland site 3 (U3) bar charts of soil moisture at A) 15 cm, B) 30 cm, and C) 60 cm and soil temperature at D) 15 cm, E) 30 cm, and F) 60 cm depths in the soil-profile. Error bars represent 95% confidence intervals. A two-sample t-test was applied for differences between the seismic line and adjacent undisturbed area at each depth for each season. Levels of significance: *, **, *** correspond to $p < 0.05$, $p < 0.01$, and $p < 0.001$ respectively.

Appendix E Soil Solids Chemistry for Upland Sites U1 and U3

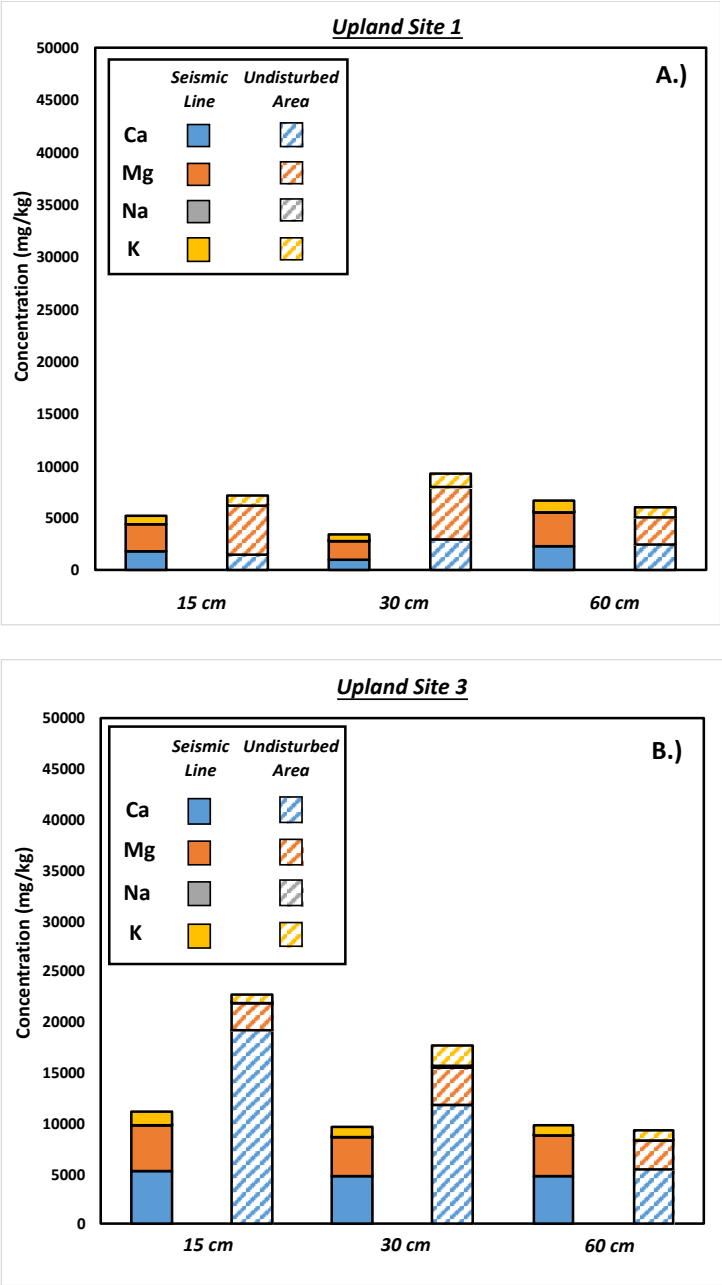

Figure E.1: Major water-soluble ion concentrations for the soil solids obtained on a seismic line and the adjacent undisturbed area over various depths for A) Upland Site 2 and B) Upland Site 3.

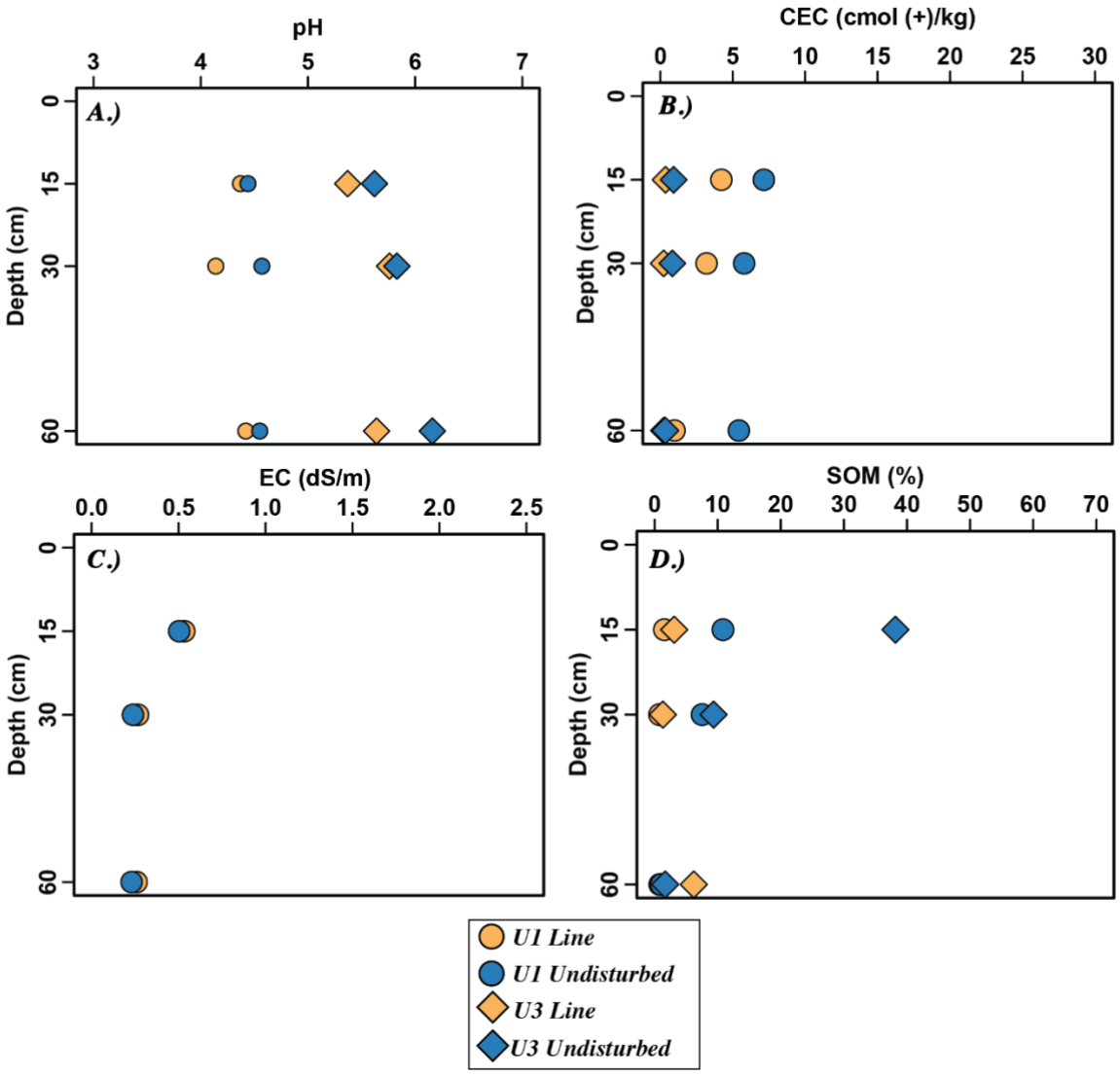

Figure E.2: Plots of A) pH, B) Cation exchange capacity (CEC), C) Electrical Conductivity (EC) and D) Soil organic matter (SOM) obtained from solids in the soil-profile for Upland sites 1 and 3.

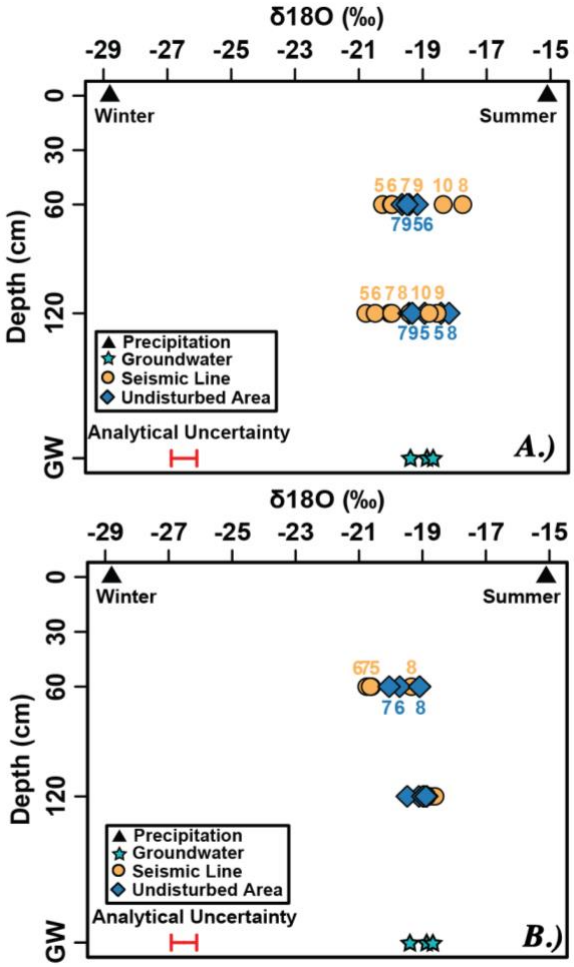

Figure E.3: Seasonal variations in $\delta^{18}O$ values at A) U1 and B) U3 separated by depth in the Fox Creek watershed (numbers above points indicate month of the year). Shown for reference are shallow Paskapoo groundwater $\delta^{18}O$ values (+/- standard deviation) along with average winter and summer precipitation $\delta^{18}O$ values. GW denotes groundwater.

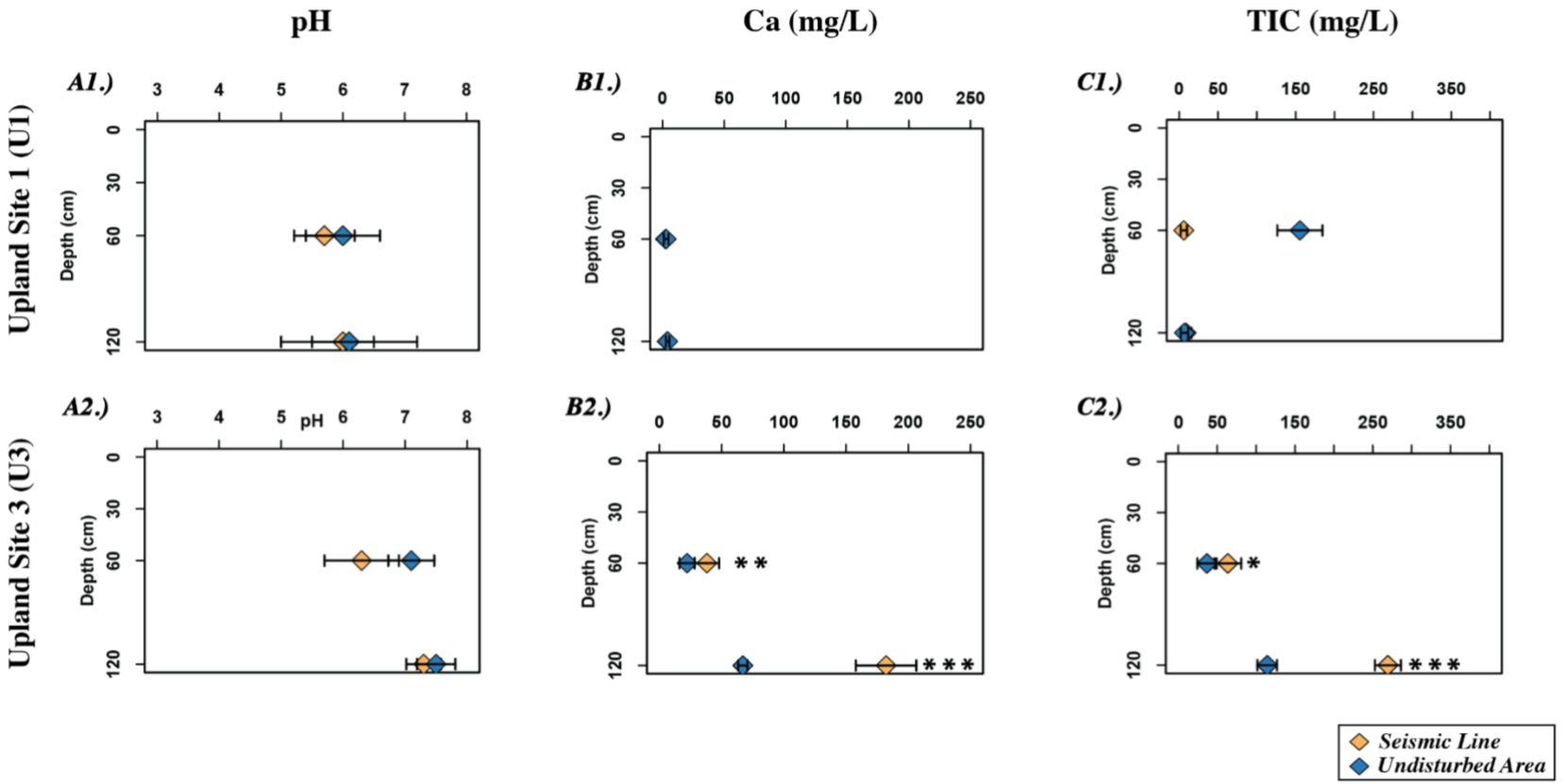

Figure E.4: Mean values (+/- standard deviation) of soil-water pH and concentrations of Ca and Total-inorganic carbon (TIC) for the soil-profiles at sites U2, L8, and L12 (the yellow and blue symbols correspond to the seismic line and undisturbed area samples respectively). The Mann-Whitney U test was applied for differences between the seismic line and undisturbed area at each depth with levels of significance: *, **, *** corresponding to $p < 0.05$, $p < 0.01$, and $p < 0.001$ respectively.

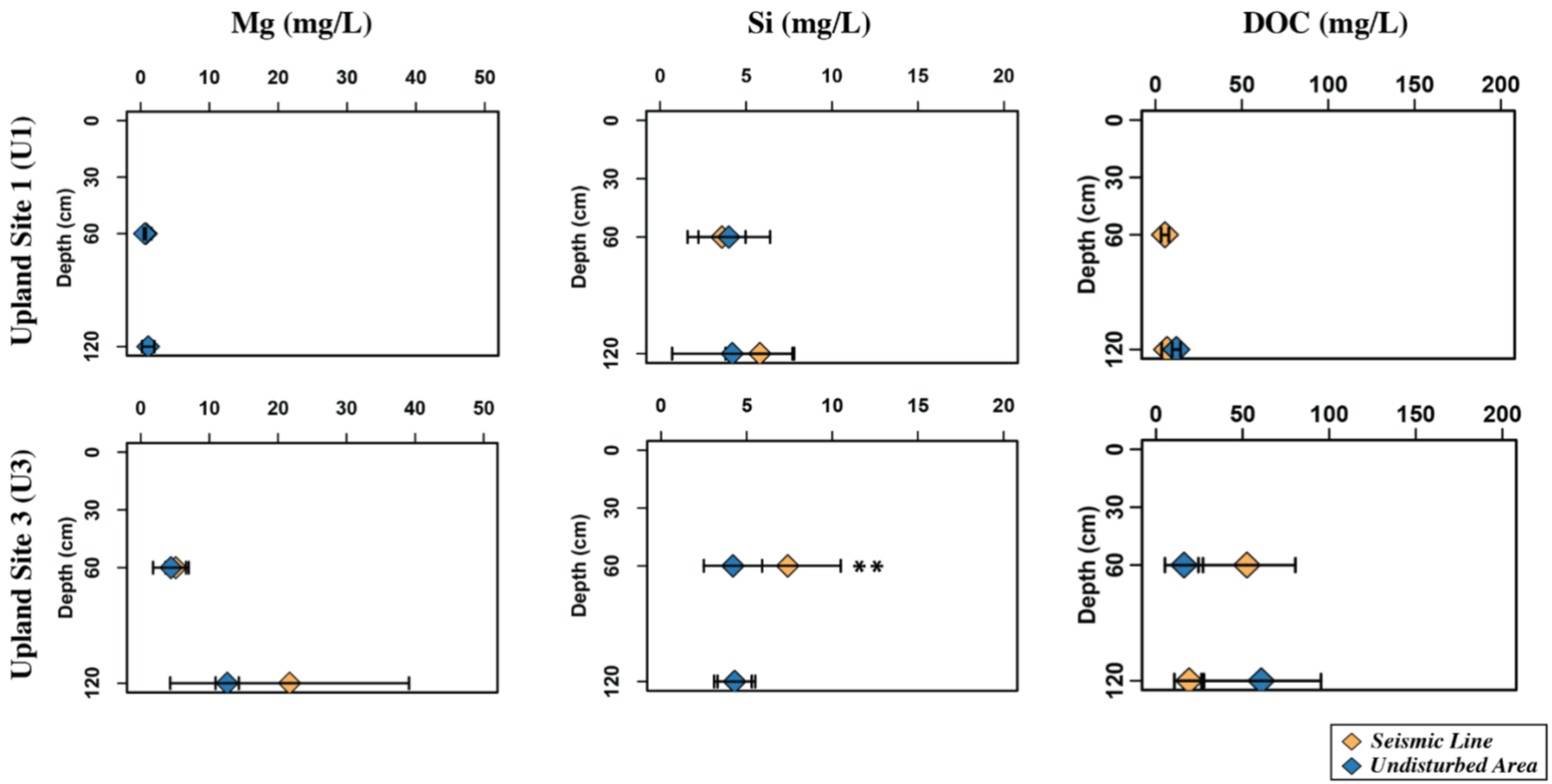

Figure E.5: Mean values (+/- standard deviation) of soil-water Mg, Si, and DOC concentrations for the soil-profiles at sites U2, L8, and L12 (the yellow and blue symbols correspond to the seismic line and undisturbed area samples respectively). The Mann-Whitney U test was applied for differences between the seismic line and undisturbed area at each depth with levels of significance: *, **, *** corresponding to $p < 0.05$, $p < 0.01$, and $p < 0.001$ respectively.

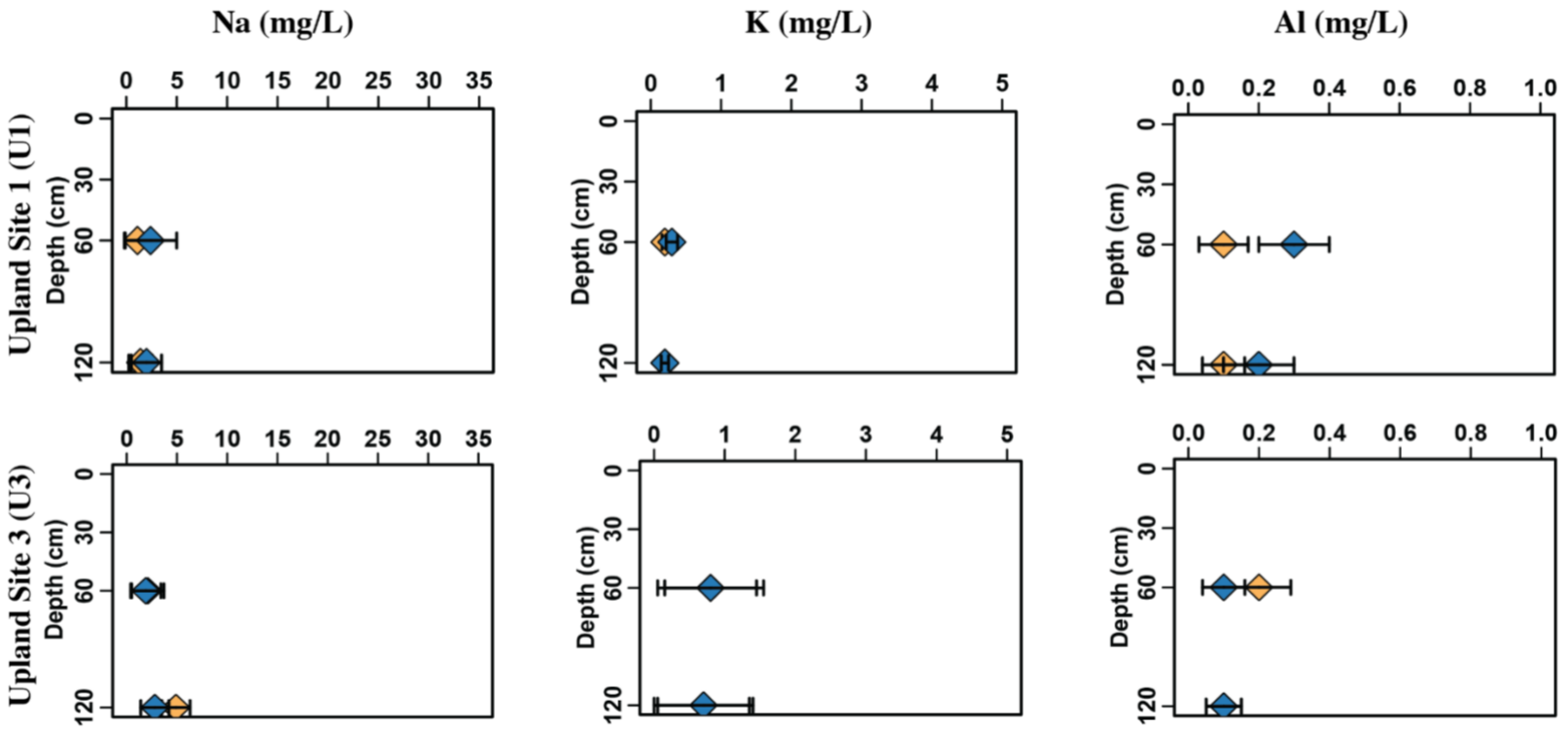

Figure E.6: Mean values (+/- standard deviation) of soil-water Na, K, and Al concentrations for the soil-profiles at sites U2, L8, and L12 (the yellow and blue symbols correspond to the seismic line and undisturbed area samples respectively). The Mann-Whitney U test was applied for differences between the seismic line and undisturbed area at each depth with levels of significance: *, **, *** corresponding to $p < 0.05$, $p < 0.01$, and $p < 0.001$ respectively.